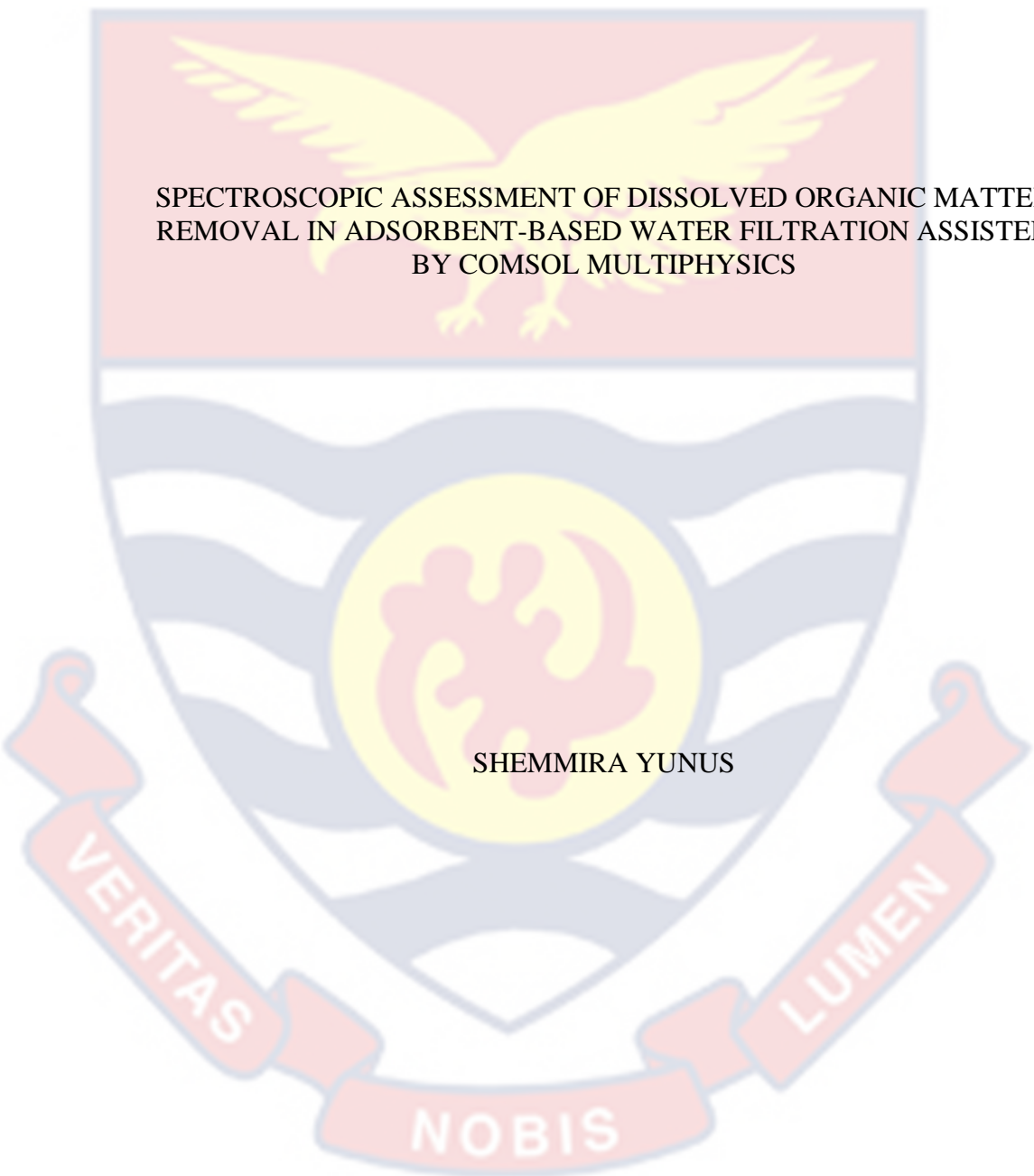


UNIVERSITY OF CAPE COAST



SPECTROSCOPIC ASSESSMENT OF DISSOLVED ORGANIC MATTER  
REMOVAL IN ADSORBENT-BASED WATER FILTRATION ASSISTED  
BY COMSOL MULTIPHYSICS

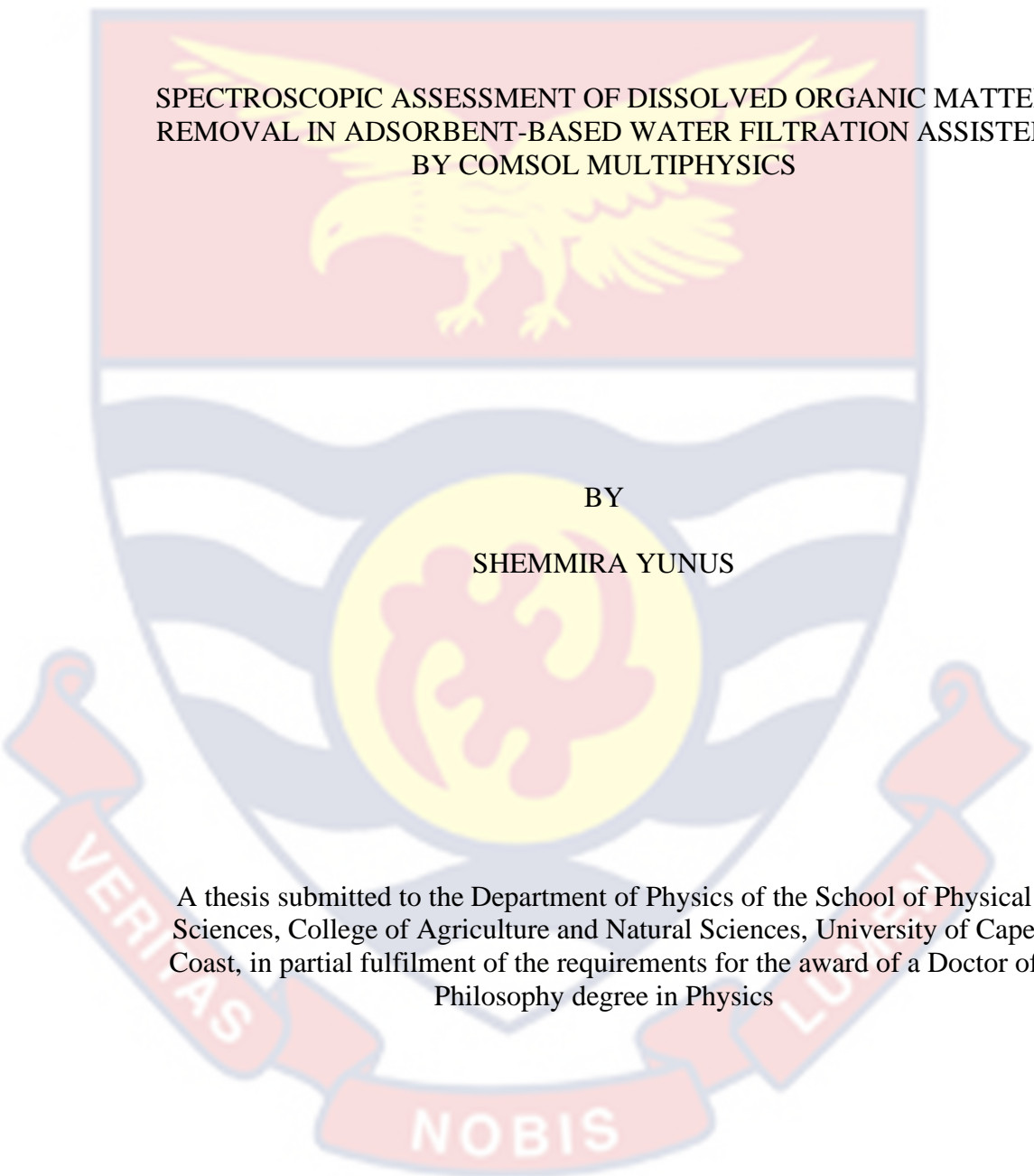
SHEMMIRA YUNUS

2023



© Shemmira Yunus  
University of Cape Coast

UNIVERSITY OF CAPE COAST



SPECTROSCOPIC ASSESSMENT OF DISSOLVED ORGANIC MATTER  
REMOVAL IN ADSORBENT-BASED WATER FILTRATION ASSISTED  
BY COMSOL MULTIPHYSICS

BY  
SHEMMIRA YUNUS

A thesis submitted to the Department of Physics of the School of Physical Sciences, College of Agriculture and Natural Sciences, University of Cape Coast, in partial fulfilment of the requirements for the award of a Doctor of Philosophy degree in Physics

MAY 2023

DECLARATION

**Candidate's Declaration**

I hereby declare that this thesis is the result of my own original research and that no part of it has been presented for another degree in this university or elsewhere.

Candidate Signature: ..... Date: .....

Name: Shemmira Yunus

**Supervisors' Declaration**

We hereby declare that the preparation and presentation of the thesis were supervised in accordance with the guidelines on supervision of thesis laid down by the University of Cape Coast.

Principal Supervisor's Signature ..... Date .....

Name: Dr. Baah Sefa-Ntiri

Co-Supervisor's Signature ..... Date .....

Name: Prof. Benjamin Anderson

## ABSTRACT

This study sought to characterise and evaluate the Dissolved Organic Matter adsorption capacity of granular activated carbon, using X-ray diffraction, Fourier transform infrared spectroscopy, absorbance, transmittance, fluorescence, and polarized light microscopy. The impact of the activating agents, adsorbent mass, and retention times on the adsorbent's performance was assessed. Twelve adsorbents were prepared, six  $\text{CaCl}_2$  activated and six  $\text{NaCl}$  activated. The adsorbents were derived from a furnace or conventional carbonisation of coconut shells, cassia siamea tree, and shea nut tree branches. The adsorbents were tested using a surface water sample at different retention times (5 minutes, 10 minutes, and 15 minutes) and adsorbent masses (10 g, 20 g, and 30 g). Analysis of the X-ray diffraction spectra revealed the presence of three phases of silicon dioxide ( $\text{SiO}_2$ ). This indicates the amorphous nature of the adsorbents and confirms the presence of carbon and graphite, which are essential for effective adsorption. The Fourier transform infrared spectra exhibited C–O and Si–O stretching, attributed to the presence of silicon-containing minerals. Absorbance, transmission, and fluorescence results demonstrated a high efficiency in DOM removal, particularly for the  $\text{CaCl}_2$ -activated adsorbents (75%). These findings were further validated through multivariate analysis. The polarized light imaging technique proved effective in distinguishing between the efficiency of the adsorbent at a polarization angle of  $90^\circ$ . Each technique provided valuable insights into the adsorbents' performance in DOM removal from surface water. The study was assisted by COMSOL Multiphysics simulation, which mimicked the behaviour of the adsorbents under specific filtration conditions.

KEY WORDS

Dissolved organic matter

Disinfection by-products

Granular activated charcoal

Laser-induced fluorescence

Multivariate analysis

Polarized light microscopy





## ACKNOWLEDGEMENTS

I would first of all, like to acknowledge the tremendous assistance of my supervisors, Dr. Baah Sefa-Ntiri and Prof. Benjamin Anderson, for they have been my main source of encouragement throughout this research. Their diligent dedication and patience in the supervision of this work have led to this great achievement.

I also wish to express my deepest gratitude to Dr. Samuel Sonko Sackey, the former coordinator of the Laser and Fibre Optics Centre (LAFOC) for his motivation and support. My sincere thanks also go to the head of the department, Prof. George Amoako and all lecturers of the Department of Physics for their various contributions to the successful completion of this work.

I, sincerely thank the International Science Programme (ISP) of Uppsala University, Sweden, and the School of Graduate Studies (SGS), University of Cape Coast for their financial support. I am undoubtedly grateful to the Laser and Fibre Optics Centre (LAFOC) of the Department of Physics, University of Cape Coast, and the current coordinator and all members of the African Spectral Imaging Network (AFSIN) for their warmth, support, and encouragement.

Lastly, I would like to acknowledge and appreciate the love and support shown by my family and friends throughout the period of this research.

DEDICATION

In memory of my father, Mr. Yunus Daud, and to my husband, Mr. Abdul-  
Mumin Al-Hassan.





## TABLE OF CONTENTS

	Page
DECLARATION	ii
ABSTRACT	iii
KEY WORDS	iv
ACKNOWLEDGMENTS	v
DEDICATION	vi
LIST OF TABLES	xi
LIST OF FIGURES	xii
LIST OF ABBREVIATIONS	xxiii
<b>CHAPTER ONE: INTRODUCTION</b>	
Background to the Study	1
Statement of the Problem	7
Purpose of the Study	7
Research Objectives	8
Significance of the Study	9
Delimitations	9
Limitations	10
Definition of Terms	10
Organisation of the Study	11
<b>CHAPTER TWO: LITERATURE REVIEW</b>	
Introduction	12
Water Treatment Techniques	12
DOM Characterisation and Removal Techniques	13
Spectroscopy	18

X-ray diffraction spectroscopy	19
Fourier transform infra-red spectroscopy	23
Ultraviolet-visible absorption and transmission spectroscopy	25
Fluorescence spectroscopy	28
Polarized light microscopy	31
COMSOL Multiphysics Simulation	32
COMSOL Multiphysics interface and features	34
Fluid flow	36
Free and porous media flow	39
Chapter Summary	40
<b>CHAPTER THREE: MATERIALS AND METHODS</b>	
Introduction	41
Preparation of Adsorbents	41
Adsorbent Characterisation	44
X-ray diffraction spectroscopy	45
Fourier transform infrared spectroscopy	45
Surface Water Sampling	46
Adsorbent Testing	46
Physicochemical water quality assessment	49
UV-visible absorbance spectroscopy	49
UV-LED induced transmission	51
Laser-induced fluorescence	52
Polarized light microscopy	53
Data Analysis (Principal Component and Cluster Analysis)	55
COMSOL Multiphysics Simulation of a Filter	55

Chapter Summary	57
CHAPTER FOUR: RESULTS AND DISCUSSION	
Introduction	58
Adsorbent Characterisation	58
X-ray diffraction spectroscopy	58
Fourier transform infrared spectroscopy	63
Physicochemical Results	65
Absorbance and Transmittance Spectrophotometer	66
Absorbance with VWR 6300PC Spectrophotometer	66
Absorbance with USB4000 Spectrometer	74
Ultraviolet Light Emitting Diode Transmittance	82
Laser-Induced Fluorescence	90
Polarized Light Microscopy	111
Average Adsorption Capacity of Prepared GAC Adsorbents	112
COMSOL Multiphysics Simulation	114
Chapter Summary	118
CHAPTER FIVE: SUMMARY, CONCLUSIONS, AND RECOMMENDATIONS	
Overview	119
Summary	119
Conclusions	120
Recommendations	123
REFERENCES	124
APPENDICES	137
APPENDIX A: GAC ADSORBENT PREPARATION PROTOCOL	137

APPENDIX B: PHYSICOCHEMICAL PARAMETERS	138
APPENDIX C : POLARIZED LIGHT IMAGES	139
PUBLICATIONS	141



## LIST OF TABLES

	Page
1 Adsorbent label description	44
2 Filtered sample labels for F_CS_CA	48
3 Filtered sample labels for all adsorbents	48
4 Crystallite sizes of the prepared adsorbents	62
5 Fingerprint Wavelengths for DOM Absorbance	67



## LIST OF FIGURES

	Page
1	The electromagnetic spectrum (Chemistry LibreTexts, 2019) 19
2	X-ray diffraction at a crystal surface (Liao, 2013) 20
3	Principle of Fourier transform infrared spectroscopy 24
4	Polarization of unpolarized light with a linear polarizer (Ferris et al., 2010) 31
5	Samples of organic agricultural by-products for adsorbent preparation (A) Coconut shells, (B) Cassia siamea tree branches, and (C) Shea nut tree branches 41
6	Conventional carbonization of raw adsorbent material (A) Initial burning process and (B) Carbonisation process 42
7	Nabertherm industrial furnace (Nabertherm, Germany) 43
8	The source of the unfiltered surface water sample (A) River Brimsu, and (B) River Brimsu flowing into the Dam. P is the point of fetching 46
9	(A) Filtration of adsorbent water mixture through Whatman filter paper (150 mm Ø) (B) Filtered water samples stored in bottles 47
10	The double-beam spectrophotometer (VWR 6300PC, USA) 49
11	Schematic Diagram of Absorbance Setup. DLS is the deuterium light source, S is the sample holder, OF is the optical fibre, SP is the spectrometer (USB 4000, Ocean Optics, USA), C is the cable, and CP is the computer. 50
12	Schematic diagram of LED-IT setup. LS is the UV light emitting diode source, S is the sample, OF is the optical fiber, SP is the



- spectrometer (USB 4000, Ocean Optics, USA), C is the cable,  
and CP is the computer. 51
- 13 Schematic Diagram of LIF Setup. LS is the laser source, S is the  
sample, OF is the optical fibre, SP is the spectrometer (USB 4000,  
LPF is the long pass filter, FPM is the fibre port-micro positioner,  
C is the cable, and CP is the computer. 52
- 14 Schematic diagram of transmission-based LEGO polarization  
imaging setup. LS is the light source (NIR-LED), P is the polarizer,  
L is the lens, T is the transmitted ray, CU is the cuvette, A, B, and  
C are the motors for controlling the light source, sample stage, and  
polarizer, PC is the Pi camera, HDO is the HDMI outlet, UC is the  
USB outlet, MI is the mouse inlet, and KI is the keyboard inlet 54
- 15 A picture of the transmission-based LEGO Polarization Imaging  
Set-up. LS is the light source (NIR-LED), LC is the light source  
power circuit, P is the polarizer, L is the lens, CU is the cuvette, A,  
B, and C are the motors for controlling the light source, sample stage,  
and polarizer respectively, PC is the Pi camera, and RB is  
the Raspberry Pi 54
- 16 (A) 3-dimensional visualisation of a designed filter model in  
COMSOL 5.6 (B) Extrusion of treatment chamber containing  
the adsorbent 56
- 17 (A) Filter model geometry and (B) meshed geometry used to  
simulate the velocity profile and transport of water contaminants  
in the designed filter 57

- 18 X-ray diffraction spectra for furnace and conventionally carbonized coconut shell (CS) activated carbon samples. 59
- 19 X-ray diffraction spectra for furnace and conventionally carbonized cassia siamea tree (CT) branch-activated adsorbents. 60
- 20 X-ray diffraction spectra for furnace and conventionally carbonized shea nut tree (ST) activated carbon samples. 61
- 21 Fourier transform infrared (FTIR) spectra from the coconut shell activated carbon adsorbents 63
- 22 Fourier transform infrared (FTIR) spectra for cassia siamea tree branch-activated carbon adsorbents 64
- 23 Fourier transform infrared (FTIR) spectra for shea nut tree branch-activated carbon adsorbents 64
- 24 Absorbance spectra for samples filtered with 10 g of furnace carbonized coconut shell-activated carbon 67
- 25 Absorbance at 254 nm for water samples filtered with 10 g of the furnace and conventionally carbonized (A) coconut shell, (B) cassia siamea tree branch, and (C) shea nut tree branch activated carbon adsorbents at 5(B1), 10(B2), and 15(B3) minutes retention times 69
- 26 Absorbance removal efficiency for samples filtered with 10 g of the furnace and conventionally carbonized coconut shell (CS), cassia siamea tree (CT) branch, and shea nut tree (ST) branch activated carbon adsorbents at 5(B1), 10(B2), and 15(B3) minutes retention times 70
- 27 Absorbance at 254 nm for water samples filtered with 20 g of the furnace and conventionally carbonized (A) coconut shell, (B)

- cassia siamea tree branch, and (C) shea nut tree branch activated carbon adsorbents at 5(D1), 10(D2), and 15(D3) minutes retention times 71
- 28 Absorbance removal efficiency for samples filtered with 20 g of the furnace and conventionally carbonized coconut shell (CS), cassia siamea tree (CT) branch, and shea nut tree (ST) branch activated carbon adsorbents at 5(D1), 10(D2), and 15(D3) minutes retention times 72
- 29 Absorbance at 254 nm for water samples filtered with 30 g of the furnace and conventionally carbonized (A) coconut shell, (B) cassia siamea tree branch, and (C) shea nut tree branch activated carbon adsorbents at 5(F1), 10(F2), and 15(F3) minutes retention times 73
- 30 Absorbance removal efficiency for samples filtered with 30 g of the furnace and conventionally carbonized coconut shell (CS), cassia siamea tree (CT) branch, and shea nut tree (ST) branch activated carbon adsorbents at 5(F1), 10(F2), and 15(F3) minutes retention times 74
- 31 Absorbance spectra for samples filtered with 10 g of the (A) furnace carbonized coconut shell, (B) conventionally carbonized coconut shell, (C) furnace carbonized cassia siamea tree branch, (D) conventionally carbonized cassia siamea tree branch, (E) furnace carbonized shea nut tree branch, and (F) conventionally carbonized shea nut tree branch activated carbon adsorbents 75

- 32 Absorbance peaks at 245 nm for samples filtered with 10 g of the furnace and conventionally carbonized (A) coconut shell, (B) cassia siamea tree branch, and (C) shea nut tree branch activated carbon adsorbents at 5(B1), 10(B2), and 15(B3) minutes retention times 76
- 33 Absorbance spectra for samples filtered with 20 g of the (A) furnace carbonized coconut shell, (B) conventionally carbonized coconut shell, (C) furnace carbonized cassia siamea tree branch, (D) conventionally carbonized cassia siamea tree branch, (E) furnace carbonized shea nut tree branch, and (F) conventionally carbonized shea nut tree branch activated carbon adsorbents 78
- 34 Absorbance peaks at 245 nm for samples filtered with 20 g of the furnace and conventionally carbonized (A) coconut shell, (B) cassia siamea tree branch, and (C) shea nut tree branch activated carbon adsorbents at 5(D1), 10(D2), and 15(D3) minutes retention times 79
- 35 Absorbance spectra for samples filtered with 30 g of the (A) furnace carbonized coconut shell, (B) conventionally carbonized coconut shell, (C) furnace carbonized cassia siamea tree branch, (D) conventionally carbonized cassia siamea tree branch, (E) furnace carbonized shea nut tree branch, and (F) conventionally carbonized shea nut tree branch activated carbon adsorbents 80
- 36 Absorbance peaks at 245 nm for samples filtered with 30 g of the furnace and conventionally carbonized (A) coconut shell, (B) cassia siamea tree branch, and (C) shea nut tree branch



- activated carbon adsorbents at 5(F1), 10(F2), and 15(F3) minutes retention times 81
- 37 UV LED induced transmittance for samples filtered with 10 g of the (A) furnace carbonized coconut shell, (B) conventionally carbonized coconut shell, (C) furnace carbonized cassia siamea tree branch, (D) conventionally carbonized cassia siamea tree branch, (E) furnace carbonized shea nut tree branch, and (F) conventionally carbonized shea nut tree branch activated carbon adsorbents. 83
- 38 UV LED induced transmittance for samples filtered with 10 g of the furnace and conventionally carbonized (A) coconut shell, (B) cassia siamea tree branch, and (C) shea nut tree branch activated carbon adsorbents at 5(B1), 10(B2), and 15(B3) minutes retention times 84
- 39 UV LED induced transmittance for samples filtered with 20 g of the (A) furnace carbonized coconut shell, (B) conventionally carbonized coconut shell, (C) furnace carbonized cassia siamea tree branch, (D) conventionally carbonized cassia siamea tree branch, (E) furnace carbonized shea nut tree branch, and (F) conventionally carbonized shea nut tree branch activated carbon adsorbents 86
- 40 UV LED induced transmittance for samples filtered with 20 g of the furnace and conventionally carbonized (A) coconut shell, (B) cassia siamea tree branch, and (C) shea nut tree branch activated carbon adsorbents at 5(D1), 10(D2), and 15(D3) minutes retention times 87

- 41 UV LED induced transmittance for samples filtered with 30 g of the (A) furnace carbonized coconut shell, (B) conventionally carbonized coconut shell, (C) furnace carbonized cassia siamea tree branch, (D) conventionally carbonized cassia siamea tree branch, (E) furnace carbonized shea nut tree branch, and (F) conventionally carbonized shea nut tree branch activated carbon adsorbents 88
- 42 UV LED induced transmittance for samples filtered with 30 g of the furnace and conventionally carbonized (A) coconut shell, (B) cassia siamea tree branch, and (C) shea nut tree branch activated carbon adsorbents at 5(F1), 10(F2), and 15(F3) minutes retention times 89
- 43 LIF spectra of all samples filtered with 10 g of the (A) furnace carbonized coconut shell, (B) conventionally carbonized coconut shell, (C) furnace carbonized cassia siamea tree branch, (D) conventionally carbonized cassia siamea tree branch, (E) furnace carbonized shea nut tree, and (F) conventionally carbonized shea nut tree branch activated carbon adsorbents 92
- 44 LIF peak intensities at 520 nm for samples filtered with 10 g of the furnace and conventionally carbonized (A) coconut shell, (B) cassia siamea tree branch, and (C) shea nut tree branch activated carbon adsorbents at 5(B1), 10(B2), and 15(B3) minutes retention times 93
- 45 LIF spectra of all samples filtered with 20 g of the (A) furnace carbonized coconut shell, (B) conventionally carbonized coconut



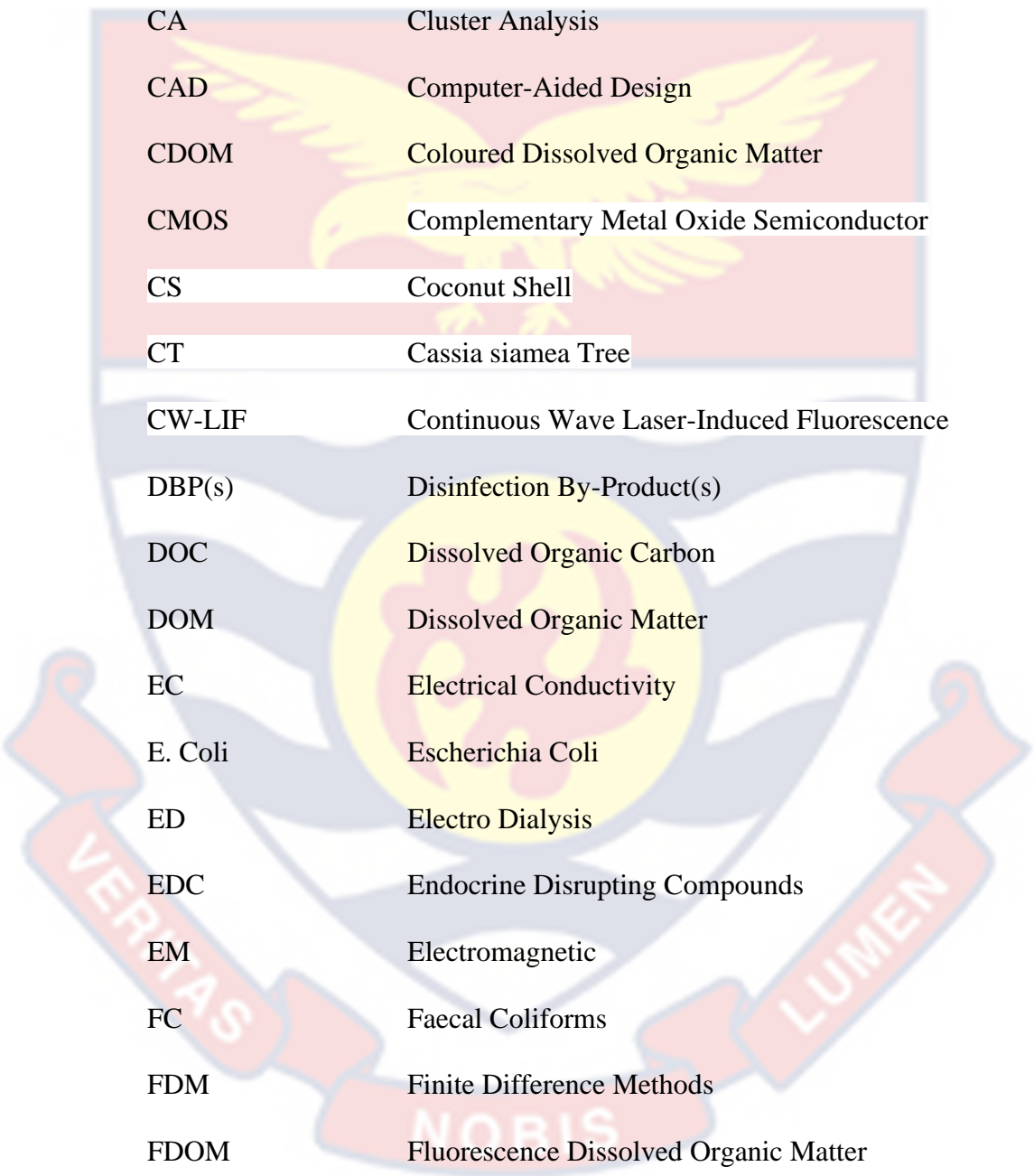
- shell, (C) furnace carbonized cassia siamea tree branch, (D) conventionally carbonized cassia siamea tree branch, (E) furnace carbonized shea nut tree branch, and (F) conventionally carbonized shea nut tree branch activated carbon adsorbents 94
- 46 LIF peak intensities at 520 nm for samples filtered with 20 g of the furnace and conventionally carbonized (A) coconut shell, (B) cassia siamea tree branch, and (C) shea nut tree branch activated carbon adsorbents at 5(D1), 10(D2), and 15(D3) minutes retention times 95
- 47 LIF spectra of all samples filtered with 30 g of the (A) furnace carbonized coconut shell, (B) conventionally carbonized coconut shell, (C) furnace carbonized cassia siamea tree branch, (D) conventionally carbonized cassia siamea tree branch, (E) furnace carbonized shea nut tree branch, and (F) conventionally carbonized shea nut tree branch activated carbon adsorbents 97
- 48 LIF peak intensities at 520 nm for samples filtered with 30 g of the furnace and conventionally carbonized (A) coconut shell, (B) cassia siamea tree branch, and (C) shea nut tree branch activated carbon adsorbents at 5(F1), 10(F2), and 15(F3) minutes retention times 98
- 49 Cluster analysis based on ward method of normalized data for samples filtered with 10 g of the (A) furnace carbonized coconut shell, (B) conventionally carbonized coconut shell, (C) furnace carbonized cassia siamea tree branch, (D) conventionally carbonized cassia siamea tree branch, (E) furnace carbonized shea nut tree branch,

- and (F) conventionally carbonized shea nut tree branch activated carbon adsorbents 100
- 50 Cluster analysis based on ward method of normalized data for samples filtered with 20 g of the (A) furnace carbonized coconut shell, (B) conventionally carbonized coconut shell, (C) furnace carbonized cassia siamea tree branch, (D) conventionally carbonized cassia siamea tree branch, (E) furnace carbonized shea nut tree branch, and (F) conventionally carbonized shea nut tree branch activated carbon adsorbents 101
- 51 Cluster analysis based on ward method of normalized data for samples filtered with 30 g of the (A) furnace carbonized coconut shell, (B) conventionally carbonized coconut shell, (C) furnace carbonized cassia siamea tree branch, (D) conventionally carbonized cassia siamea tree branch, (E) furnace carbonized shea nut tree branch, and (F) conventionally carbonized shea nut tree branch activated carbon adsorbents 102
- 52 Scree plot of the eigenvalues of the principal components for the LIF spectra 103
- 53 Score plots for samples filtered with 10 g of the (A) furnace carbonized coconut shell, (B) conventionally carbonized coconut shell, (C) furnace carbonized cassia siamea tree branch, (D) conventionally carbonized cassia siamea tree branch, (E) furnace carbonized shea nut tree branch, and (F) conventionally carbonized shea nut tree branch activated carbon adsorbents 104

- 54 Score plots for samples filtered with 20 g of the (A) furnace carbonized coconut shell, (B) conventionally carbonized coconut shell, (C) furnace carbonized cassia siamea tree branch, (D) conventionally carbonized cassia siamea tree branch, (E) furnace carbonized shea nut tree branch, and (F) conventionally carbonized shea nut tree branch activated carbon adsorbents 105
- 55 Score plots for samples filtered with 30 g of the (A) furnace carbonized coconut shell, (B) conventionally carbonized coconut shell, (C) furnace carbonized cassia siamea tree branch, (D) conventionally carbonized cassia siamea tree branch, (E) furnace carbonized shea nut tree branch, and (F) conventionally carbonized shea nut tree branch activated carbon adsorbents 106
- 56 Euclidean distances from the standard water sample to all samples filtered with 10 g of the (A) furnace carbonized coconut shell, (B) conventionally carbonized coconut shell, (C) furnace carbonized cassia siamea tree branch, (D) conventionally carbonized cassia siamea tree branch, (E) furnace carbonized shea nut tree branch, and (F) conventionally carbonized shea nut tree branch activated carbon adsorbents 108
- 57 Euclidean distances from the standard water sample to all samples filtered with 20 g of the (A) furnace carbonized coconut shell, (B) conventionally carbonized coconut shell, (C) furnace carbonized cassia siamea tree branch, (D) conventionally carbonized cassia siamea tree branch, (E) furnace carbonized shea nut tree branch,

	and (F) conventionally carbonized shea nut tree activated carbon adsorbents	109
58	Euclidean distances from the standard water sample to all samples filtered with 30 g of the (A) furnace carbonized coconut shell, (B) conventionally carbonized coconut shell, (C) furnace carbonized cassia siamea tree branch, (D) conventionally carbonized cassia siamea tree branch, (E) furnace carbonized shea nut tree branch, and (F) conventionally carbonized shea nut tree branch activated carbon adsorbents	110
59	Polarized light intensity plot of all samples filtered with 30 g of the CaCl <sub>2</sub> -activated adsorbents	111
60	DOM removal efficiency for samples filtered with CaCl <sub>2</sub> - and NaCl-activated carbon adsorbents	112
61	DOM removal efficiency for the different activating chemicals	113
62	(A) Surface plot and (B) Contour plot of the velocity profile of water flow through the designed filter	114
63	Line plot of the velocity profile of water flow through the filter	115
64	Contour plot of the pressure profile of water flow through the filter	116
65	Change in species concentration with adsorbent thickness for 30 hours	117
66	Change in concentration with adsorbent thickness for 120 hours	118

## LIST OF ABBREVIATIONS

The background of the page features a large, semi-transparent watermark of the University of Cape Coast crest. The crest is a shield-shaped emblem with a yellow eagle with outstretched wings in the center. The shield is divided into four quadrants by a white cross. The top-left quadrant is red, the top-right is white, the bottom-left is blue, and the bottom-right is white. A red banner curves across the bottom of the shield with the Latin motto 'VERITAS NOBIS LUMEN' in white capital letters.

A <sub>254</sub>	Absorbance at 254 nm
AC	Activated Carbon
BEM	Boundary Element Method
CA	Cluster Analysis
CAD	Computer-Aided Design
CDOM	Coloured Dissolved Organic Matter
CMOS	Complementary Metal Oxide Semiconductor
CS	Coconut Shell
CT	Cassia siamea Tree
CW-LIF	Continuous Wave Laser-Induced Fluorescence
DBP(s)	Disinfection By-Product(s)
DOC	Dissolved Organic Carbon
DOM	Dissolved Organic Matter
EC	Electrical Conductivity
E. Coli	Escherichia Coli
ED	Electro Dialysis
EDC	Endocrine Disrupting Compounds
EM	Electromagnetic
FC	Faecal Coliforms
FDM	Finite Difference Methods
FDOM	Fluorescence Dissolved Organic Matter
FEA	Finite Element Analysis
FEM	Finite Element Method
FTIR	Fourier Transform Infrared



The background of the page features a large, semi-transparent watermark of the University of Cape Coast crest. The crest is a shield-shaped emblem with a yellow eagle with outstretched wings in the center. The shield is divided into three horizontal sections: a top red section, a middle white section with blue wavy lines, and a bottom yellow section. A red ribbon scrolls across the bottom of the shield with the Latin motto 'VERITAS NOBIS LUMEN'.

FVM	Finite Volume Method
FWHM	Full Width Half Maximum
GAC	Granular Activated Carbon
GACF	Granular Activated Carbon Filtration
GLAAS	Global Analysis and Assessment of Sanitation and Drinking Water
GWCL	Ghana Water Company Limited
HAA	Halo-Acetic Acid
LED	Light Emitting Diode
LED-IT	Light Emitting Diode Induced Transmission
LIF	Laser-Induced Fluorescence
MF	Micro-Filtration
MW	Molecular Weight
NF	Nano-Filtration
NIR	Near Infrared
NOM	Natural Organic Matter
NS	Navier Stokes
PAC	Powdered Activated Carbon
PCA	Principal Component Analysis
PDEs	Partial Differential Equations
PM	Perturbation Methods
PUF	Polyurethane Foam
Re	Reynolds number
RO	Reverse Osmosis
RSF	Rapid Sand Filtration



SDGs	Sustainable Development Goals
SSF	Slow Sand Filtration
ST	Shea nut Tree
TDS	Total Dissolved Solids
TOC	Total Organic Carbon
TR-LIF	Time Resolved Laser-induced Fluorescence
TSS	Total Suspended Solids
THM	Tri-Halo Methane
UCC	University of Cape Coast
UF	Ultra-Filtration
USA	United States of America
UV	Ultra Violet
WHO	World Health Organization
XRD	X-Ray Diffraction



## CHAPTER ONE

### INTRODUCTION

Access to safe and affordable drinking water is the primary driver of enhanced public health and economic growth. Dissolved Organic Matter (DOM) in water, especially surface water sources, poses a significant challenge to most conventional water treatment techniques and human health due to the formation of disinfection by-products after disinfection. Due to DOM's heterogeneous and complex nature, the inadequacies of most conventional water treatment techniques necessitate the exploration of cost-effective technologies for efficient DOM removal. In this chapter, the background to the study, statement of the problem, purpose of the study, research objectives, significance of the study, delimitations and limitations of the study, and the definition of some terms used in the study, have been presented.

#### **Background to the Study**

Safe water scarcity has gained significant recognition over the years due to its impact on global development. The availability of safe and affordable water is the main catalyst for improved public health and thus economic growth. To this end, the Sustainable Development Goal (SDG) 6.1, calls for globally unbiased access to safe and affordable drinking water (World Health Organisation, 2019). Current reports by the World Health Organisation (WHO), however, suggest that 783 million people still lack access to safe water, with over 500 million people relying on unprotected and untreated ground and surface water resources. A global population of 2 billion people also depends on water sources with high levels of faecal and other physicochemical contaminants (World Health Organisation, 2019).

The critical lack of safe and affordable water, especially amid the current COVID-19 emergency, not only affect human health but also the quality of life of the general population, especially women and children (García, 2011; World Health Organisation, 2017). This challenge of safe water scarcity may be attributed to the gradual growth in population, the high levels of water pollution contaminants in freshwater sources; as well as the lack of improved and innovative technology to easily assess and control water pollution (World Health Organisation, 2020). The steady rise in safe water scarcity, especially due to water pollution and higher water demand, therefore necessitates the development of efficient and cost-effective water remediation techniques, especially in developing countries where the quality of natural water resources is easily compromised.

Ghana is not an exception in the global safe water crisis, despite her riches in terms of natural water resources. The quality of water in the country is under constant pressure with the continual usage of manual water quality assessment techniques, such as water quality sampling, transportation, and preservation, which are cumbersome and subjective (Okache et al., 2015). In addition, the WHO global water, sanitation, and hygiene report, with recent data from Ghana and the Global Analysis and Assessment of Sanitation and Drinking Water (GLAAS) 2018/2019, highlighted the urgent need for improved drinking water quality in Ghana. Curbing the challenge of safe water scarcity will also be a big step towards achieving goal 6.1 of the SDGs (World Health Organisation, 2019) since most rural and some urban dwellers in Ghana still rely on unsafe ground and surface water resources for drinking and other domestic activities (World Health Organisation, 2017; World Health Organisation, 2019).

Research (García, 2011) also suggests that, in an attempt to resolve the challenge of safe water scarcity, developing countries like Ghana, should focus on developing sustainable and easy-to-maintain techniques and/or systems for water purification. This could be achieved through using local agricultural by-products to develop environmentally friendly techniques and systems for effective water remediation, instead of their synthetic and cost-intensive counterparts (García, 2011). There is, therefore, the need to develop innovative, environmentally friendly, and cost-effective point-of-use water quality analysis and treatment techniques that would ensure the continual availability of safe water.

Ensuring continued access to safe water is, however, a very challenging task due to the numerous classes of contaminants present in the ground and surface water resources. Water pollution contaminants are generally categorized into four main classes: Physical, Chemical, Biological, and Radiological contaminants (U.S. Environmental Protection Agency, 2012).

Physical contaminants mainly include dissolved or suspended organic materials in water. They are mainly carbon-based and, thus, easy to bind with human tissue, which makes them extremely toxic even in small concentrations. Physical contaminants also affect the physical appearance of water, and hence, its aesthetic properties, such as taste, colour, and odour. Some physical contaminants include; Dissolved Organic Matter (DOM), Total Dissolved Solids (TDS), and Total Suspended Solids (TSS).

Chemical contaminants, on the other hand, are mostly inorganic and constitute different compounds and elements. Chemical contaminants mostly include but are not limited to drugs, pesticides, and bleach. Others include nitrates and nitrites, fluorides, arsenic, and lead.

Biological contaminants, are however commonly classified under microbiological contaminants or microbes and are mainly made up of living organisms. Examples include parasites, pathogenic and non-pathogenic bacteria, protozoa, and viruses. Some indicators of microbiological contamination in water also include faecal coliform (FC) and *Escherichia coli* (*E. coli*) (Sharma & Bhattacharya, 2017; World Health Organisation, 2017; World Health Organisation, 2020).

Radiological contaminants, which are mostly categorized under chemical contaminants, also find their way into our water sources. Radiological contaminants are chemical elements with unstable atoms, thus, leading to the emission of ionizing radiation. Such radioactive contaminants are generally carcinogenic, with surface water being more susceptible than groundwater resources.

Each of the above-mentioned classes of contaminants may also be broadly categorized as natural or anthropogenic based on origin (Sharma & Bhattacharya, 2017; U.S. Environmental Protection Agency, 2012).

DOM is one of the few physical contaminants with both a natural and anthropogenic origin. It is a constituent of Natural Organic Matter (NOM) which is a carbon-based compound mostly found in higher concentrations in surface and groundwater resources. The presence of DOM in surface water is always most likely attributed to the breakdown of plant material or regarded as the by-product of microbiological activities. This led to the two main categories of DOM; allochthonous and autochthonous DOM. Allochthonous DOM is produced from the breakdown of terrestrial plant material and thus contains more humic-like compounds, whilst autochthonous DOM, is produced within the water source from microbiological activities, and contains less humic-like



compounds. Each category of DOM is further made up of protein-like or humic-like constituents based on the heterogeneous mixture of the compounds present (Hidayah, Chou, & Yeh, 2018; Williams, Conrad, Kothawala, & Baulch, 2019).

As a carbon-based physical contaminant, DOM not only affects the aesthetic quality of drinking water but also causes the formation of disinfection by-products (DBPs) when it reacts with chlorine. The major classes of DBPs formed, when DOM reacts with chlorine are Tri-Halo Methane (THM) and the Halo-Acetic Acid (HAA). The formation level of these chlorine-based DBPs (THM and HAA) is, however, dependent on the category of DOM present and its composition and concentration in the water sample. Allochthonous DOM causes the formation of THM and HAA in high concentrations due to the high levels of the humic-like compounds present. Autochthonous DOM, on the other hand, has lower levels of the humic-like compounds present and thus, has a lower ability to form THM and HAA.

Autochthonous DOM can, however, cause the formation of nitrogen-based DBPs when the water sample is disinfected with chloramine (Hidayah et al., 2018; Williams et al., 2019; Yusuf & Audu, 2017). This notwithstanding, it can generally be stated that allochthonous DOM has a more direct relationship with the formation of DBPs during chlorine-based disinfection of DOM-infested water (Williams et al., 2019).

The general lack of understanding of the link between DOM reactivity and heterogeneity complicates its removal with most conventional water purification systems. This leads to a low DOM removal efficiency and increased cost of water treatment. Hence, with the steady rise in DOM concentrations, especially in our surface water systems, most conventional water treatment techniques are becoming limited and, are in dire need of optimisation. The



optimization of these conventional techniques would help in the effective removal of DOM and hence reduce the formation of DBPs, whilst also tackling other contaminants. It is, therefore, necessary to develop new and improved techniques for the efficient and cost-effective removal of DOM from our natural water resources.

However, due to the link between the humic-like constituents of DOM and DBP formation rate, the characterization of DOM has become a necessary step towards the development of effective techniques for its removal. The most commonly used DOM characterization technique in recent times is resin fractionation, which makes use of the hydrophobic nature of DOM to separate it into various fractions. The major limitation of this characterization technique has to do with its applicability, timeliness, water sample modification methods, and the exactness in the determination of DOM concentration in a particular water sample. The inability to curb these limitations led researchers into the use of total organic carbon (TOC) and chemometric techniques as surrogates for DOM characterization and quantification (Chiu, Huang, Chen, & Yeh, 2019; Wang & Chen, 2018; Yunus, 2020).

Fluorescence spectroscopy has however, recently gained much recognition among other spectroscopic techniques, as a more preferred method due to its sensitivity and selectivity, that is, its ability to detect very low contaminant concentrations and distinguish between different fluorophores (Chiu et al., 2019; Wang, Zheng, Jiang, Chen, & Wang, 2020). Moreover, with the recent advancements in technology, and hence the emergence of several multivariate techniques, such as Parallel Factor Analysis (PARAFAC), Principal Component analysis (PCA), Cluster analysis (CA), etcetera, the use

of spectroscopy coupled with some multivariate techniques, paves the way for much-detailed sample characterisation.

This study is, therefore, geared towards the characterisation, quantification, and subsequent removal of DOM from surface water samples using several spectroscopic (X-ray diffraction, Fourier transform infrared spectroscopy, absorbance, fluorescence, and polarized light microscopy) and multivariate (PCA and CA) techniques. An unsupervised pattern recognition method was employed in the present study for efficient discrimination between the several data sets obtained from the spectroscopic techniques. This study would also evaluate the flow velocity and flow rates of water through a modeled activated-carbon embedded polyurethane foam (PUF) composite membrane filter using COMSOL Multiphysics simulations.

### **Statement of the Problem**

The presence of DOM in drinking water poses grave threats to human health and increases the cost of water purification. The structural complexity of DOM, and the dependence of DBP formation rates on some specific components, create a lot of challenges in DOM removal. This, therefore, necessitates the use of some effective spectroscopic techniques and novel adsorbent filtrated methods, for the characterisation and subsequent removal of DOM from water samples.

### **Purpose of the Study**

The purpose of this study was to effectively characterise and subsequently remove DOM in surface water samples using some spectroscopic techniques and locally prepared Granular Activated Carbon (GAC) from different agricultural by-products. The methods used in this study were aimed

at obtaining an efficient and environmentally friendly GAC adsorbent for effective DOM removal from surface water through composite membrane filtration.

This study also sought to, address the challenge of effective DOM characterization, which would aid in the effective removal of DOM using spectroscopic and novel adsorbent filtration techniques, assisted by COMSOL Multiphysics simulations. The results of this study, along with the COMSOL Multiphysics simulation results, would help in assessing the efficiency of the prepared adsorbents and the modeled composite membrane filter in terms of effective DOM removal, especially from surface water.

### **Research Objectives**

The main objective is to effectively characterize DOM in surface water using spectroscopic techniques and remove DOM using locally prepared GAC from different agricultural by-products.

The specific objectives of the study are to:

1. prepare and characterise GAC adsorbents using different agricultural by-products for effective DOM removal
2. filter raw surface water samples using the prepared GAC adsorbents
3. characterise DOM in filtered and unfiltered surface water samples using spectroscopic techniques and assess the DOM removal performance of GAC
4. assess the effect of chemical activation agents on the performance of the GAC adsorbents
5. model and simulate the velocity profile of fluid flow, as well as the transport and adsorption of water contaminants in a designed GAC-

embedded composite membrane filter using the fluid flow model in COMSOL Multiphysics for large-scale water treatment

### **Significance of the Study**

The results of this study would help establish the performance of some spectroscopic techniques in DOM characterization and quantification, thus, increasing DOM removal efficiency from natural water sources with locally prepared GAC adsorbents. The results of the study would generally reduce water purification costs, and subsequently curb the safe water scarcity crises that plague the rural communities of most developing countries. The COMSOL simulation results would also present the perfect model requirements and blueprint for packing the best GAC adsorbent filter with a PUF substrate to achieve significant levels of DOM removal efficiencies and a longer filter life span. The total outcome of the study will serve as a stepping stone towards achieving SDG 6.1 which aims at achieving universal and equitable access to safe and affordable drinking water by 2030 in Ghana and other developing countries.

### **Delimitations**

This study focused on using specific agricultural by-products from the Upper West and Central regions of Ghana, and the findings may need to be generalisable to the same agricultural by-products from other regions or countries. The assessment may be limited to the specific set of prepared adsorbents and other types not considered in this study. Moreover, the study only investigated some physicochemical contaminants and the removal of dissolved organic matter (DOM) and did not extensively address the removal of other water contaminants. The water samples used in this study were fetched

from river Brimsu (Central region); hence, the findings may not apply to water from diverse sources or seasons. The filtration technique used to test the adsorbent performance was done at a laboratory scale, and the findings may only partially represent the complexities and disparities in real-life situations. The discrepancies between the laboratory scale and real-life situations were mitigated using COMSOL Multiphysics simulation.

### **Limitations**

This study was conducted in a controlled laboratory environment, and real-life applications may introduce additional parameters not accounted for. The adsorbent performance was also assessed for a limited time without considering seasonal variations and their effect on DOM concentration in surface water. Rapid advancements in adsorbent technologies or water remediation techniques may have occurred after this study. As such, the findings may not reflect any of the latest innovations in the field.

### **Definition of Terms**

Dissolved Organic Matter is dissolved organic compounds in water or soil that consist of various natural and anthropogenic substances such as humic and fulvic acids.

Adsorbent-based water filtration is a water treatment technique that involves using solid materials (adsorbents) to attract and retain dissolved organic matter from water through adsorption.

Adsorption is the process by which dissolved organic matter adheres to the surface of an adsorbent material, forming a layer or film on its surface.



## Organisation of the Study

The organisation of the rest of this thesis is as follows: Chapter one gives a brief overview of safe water scarcity, its causes, and how it affects developing countries such as Ghana. Under this same chapter, the main contaminant of focus, DOM, was elaborated on, showing its effects on human health and how it could be characterised and removed from drinking water using locally prepared GAC adsorbents. The scope of this study, objectives, and significance, as well as the organisation of the rest of the thesis also included in chapter one.

Chapter two concentrates on some recent and not-so-recent studies in line with this thesis, which makes up the literature review section. The section will focus on COMSOL Multiphysics and some spectroscopic techniques, with much emphasis on X-ray diffraction (XRD) spectroscopy, Fourier Transform Infrared (FTIR) spectroscopy, UV-visible absorption and transmission, Laser-Induced Fluorescence (LIF), and polarized light microscopy.

Chapter three, is however, divided into six (6) sections; COMSOL Multiphysics simulation, preparation of adsorbents, characterisation of adsorbents, surface water sampling, and adsorbents testing. Chapter four reports the research findings from each section discussed in chapter three and gives discussions of these findings.

The last chapter, chapter five, gives the summary of the whole study, the conclusions made, and applicable recommendations for future research.

## CHAPTER TWO

### LITERATURE REVIEW

#### Introduction

This chapter reviews the literature on water treatment techniques, and spectroscopy, with emphasis on X-ray diffraction (XRD) spectroscopy, Fourier Transform Infrared (FTIR) spectroscopy, UV-visible absorption and transmission, Laser-Induced Fluorescence (LIF), polarized light microscopy. The research outcomes from several studies on the use of GAC for water treatment are also discussed. A brief review of the literature on COMSOL Multiphysics is also given.

#### Water Treatment Techniques

The presence of water pollution contaminants in most water sources has become a common global concern. Despite their difference in origin, higher levels of water pollution contaminants may lead to acute and possibly fatal health problems when such water is consumed. This has led to the establishment of certain quality standards by the World Health Organisation (WHO), towards evaluating the suitability of water, for domestic usage, especially for drinking purposes (Sharma & Bhattacharya, 2017).

Some waterborne diseases such as cholera, typhoid fever, and hepatitis A or E, are caused by pathogenic microorganisms that can easily spread through drinking contaminated water. But aside from these life-threatening microbiological contaminants, some equally dangerous contaminants should be well-thought-out in the holistic treatment of water for drinking. One such contaminant is organic matter, which is especially difficult to remove in the dissolved form, known as DOM (Sharma & Bhattacharya, 2017).

## DOM Characterisation and Removal Techniques

As the levels of DOM rise in surface water, most centralized water purification and distribution systems, including point-of-use drinking water treatment plants, face grave challenges in optimizing available techniques for the effective removal of DOM. This has led to the failure to curb the potential formation of DBPs amidst the general struggle of removing other contaminants from drinking water (Williams et al., 2019). Hence, with the main dependence of DBP formation on the reactivity of DOM with chlorine, the most important step towards controlling the formation of DBPs is the effective removal of DOM from water sources (Hidayah et al., 2018). Several treatment techniques have been developed and studied over the years for effective DOM removal, but the most commonly used are coagulation and filtration.

The success of coagulation is highly dependent on the type of DOM present in the sample, the coagulant type and dose, as well as other physicochemical parameters such as pH. The humic component of DOM, which is the main contributing factor to the formation of DBPs, is mostly removed through coagulation. This, however, majorly depends on the nature of the coagulant and the characteristics of the DOM in question. Coagulation is also limited in the area of tackling only the humic compounds, since the non-humic or hydrophilic compounds also contribute to the formation of DBPs, especially in water with low humic concentrations (Hansen et al., 2016; Hidayah et al., 2018; Williams et al., 2019). An increased coagulant demand, based on the character of DOM may also lead to the deterioration of the pathogen removal capability, and hence result in suboptimal outcomes in the coagulation process. These limitations may cause damage to water treatment utilities and

subsequently lead to poor performance in DOM removal (Health Canada, 2019).

Filtration is another common and very important technique for water treatment. It targets very small particles, as well as some bacteria, heavy metals, and even some viruses, depending on the type of filtration technique. With the trends of current research in the field of filtration, different types of filtration techniques are now available. These techniques are broadly categorized into, membrane filtration and granular media filtration.

Membrane filtration is essentially a filtration technique that involves a single permeable layer that allows some constituents of a liquid sample to pass through whilst blocking others. Membrane-based filtration techniques therefore rely mainly on the pore size of the permeable layer involved and are thus broken down into micro-filtration (MF), ultra-filtration (UF), nano-filtration (NF), and reverse osmosis (RO). These techniques target both physicochemical and microbiological contaminants with particle sizes ranging from 0.5 to 5, 0.005 to 0.5, 0.0007 to 0.005, and  $<0.0007$  microns ( $\mu\text{m}$ ), respectively. The membranes used in each membrane filtration technique can be made from polymeric, metallic, ceramic, or fibre materials. Some advantages of membrane-based water filtration include a wide range of target contaminants, consistent production of good quality water, limited chemical and energy usage, portability, and flexibility (Hoslett et al., 2018; Shabiimam et al., 2018; Zedda et al., 2015).

However, despite the advantages of these membrane filtration techniques, dissolved contaminants with very minute particle sizes, smaller than the pore sizes in each filtration technique, can escape into the permeate. Even



with the very small pore sizes in reverse osmosis and its ability to remove all impurities smaller than a water molecule, this technique also rids water of its natural and essential minerals. An attempt to replenish these nutrients further leads to an increase in the pH of the treated water sample.

RO membrane filtration is also energy intensive and requires sample pre-treatment with micro or ultrafiltration to curb membrane fouling problems, especially with the presence of DOM. The occurrence of membrane fouling decreases membrane selectivity with time, thus leading to integrity failure and a shorter lifetime. Moreover, recent advances in NF or RO techniques towards reducing membrane fouling, have increased its energy requirements and the need for technical expertise. Thus, making these techniques unsustainable options for developing countries (Hoslett et al., 2018; Yunus, 2020).

Granular media filtration techniques, on the other hand, include rapid sand filtration (RSF), slow sand filtration (SSF), and granular activated carbon filtration (GACF).

SSF is a relatively simple technique that has been used for over eighteen centuries. It uses a sand bed that targets the contaminants, followed by a course layer that prevents the sand from clogging the outlet. SSF is a very good technique for removing suspended solids, some microbiological contaminants, and heavy metals. Its ability to remove microbiological contaminants from water relies on the formation of a biofilm containing bacteria that prey on other incoming microbes (Shabiimam et al., 2018).

However, with time, due to the continuous deposition of contaminants on the filter media, the pores get clogged, thus resulting in reduced filter performance. Some downsides of SSF include low flow rates, long maturation



periods, and large area requirements. Thus, mostly desirable for centralised water purification and distribution systems (Hoslett et al., 2018; Shabiimam et al., 2018; Yunus, 2020).

RSF, on the other hand, was developed in the 80s to help curb the problem of large area requirements of the SSF. This technique constitutes the use of two specific types of filters, that is, the rapid gravity filter and the rapid pressure filter. The main components of each of these filter types include the filter chamber, fine sand, and gravel for support. RSF is not effective as a stand-alone technique and thus requires some pre-treatment steps such as coagulation, sedimentation, and flocculation, as well as post-treatment techniques such as disinfection, mostly with chlorine. When combined with these pre- and post-treatment techniques, RSF can be a highly efficient technique in removing turbidity and other chemical contaminants (such as arsenic, salts, etcetera).

The lifetime of an RSF system is however dependent on maintaining a 30-minute backwashing process every 24 hours. This process removes most of the particulate matter stuck on the filter bed or in between the pores (Shabiimam et al., 2018). Hence, for a typical water treatment plant design using RSFs, there must be several rapid sand filters available to give way for the backwashing of a used filter. However, as one RSF is being cleaned, the flow on the others becomes higher, thus causing a flow surge, which can lead to low treatment efficiency.

Additionally, as a RSF is being used, the sand media deteriorates rapidly with time, due to the accumulation of contaminants on the sand media. These accumulated contaminants include some inorganic compounds which can only be removed through heterogeneous, homogenous, and biological oxidation (Hoslett et al., 2018; Shabiimam et al., 2018).

AC is a globally preferred adsorbent that is predominantly used for contaminant removal from water and wastewater. AC exists as a microporous carbon with a high contaminant adsorption capacity due to its well-developed pores and high internal surface area (Jjagwe, Olupot, Menya, & Kalibbala, 2021; Lu et al., 2020).

Current research suggests that many AC adsorbents are made from a variety of agricultural waste materials. Some of these can be categorized under shells, wood, petroleum, and coal (Bakti & Gareso, 2018; Bergna, Hu, Prokkola, Romar, & Lassi, 2020; Hoslett et al., 2018). The prepared activated carbon from these raw materials varies in particle size and several other intrinsic properties based on the activation methods used. With regards to particle size, AC adsorbents can be broadly categorized into powdered activated carbon (PAC) and granular activated carbon (GAC).

GAC has generally larger particle sizes compared to PAC, with GAC particle sizes ranging from 0.2 mm to 5 mm, and that of PAC equal to or less than 0.188 mm. GAC is almost always used in water filtration systems for the removal of organic contaminants through the process of adsorption. The efficiency and lifetime of such filtration systems largely depend on the pore characteristics of the adsorbent, which is very dependent on the preparation method, as well as the contaminant type and concentration (Galvão, da Silva Moretti, Fernandes, & Kuroda, 2021; Hoslett et al., 2018).

The application of GAC in water filtration systems replaces RSF or is mostly used alongside, thus reducing the need for the addition of other treatment steps. GAC can remove some components of DOM by adsorbing the dissolved matter onto its well-developed surface. However, as this adsorption process continues, a biofilm is subsequently created, hence reducing the DOM removal

efficiency of the GAC adsorbent. This defect was addressed by combining the adsorption process with a biodegradation step (Hoslett et al., 2018).

Several other researchers (Bedru et al., 2019; Galvão et al., 2021; Jjagwe et al., 2021; Shabiimam et al., 2018) highlighted the versatile nature of GAC as a filtration material capable of removing various forms of pollution. These generalizations are however based on the availability and sustainability of effective modification techniques used in the preparation of highly efficient GAC. Hence, whilst the complex and cost-intensive AC adsorbents in the developed world are effective in the removal of most organic contaminants, the cost-effective brands in the developing world are mostly used in combination with other treatment techniques to achieve safe drinking water standards (Hoslett et al., 2018; Shabiimam et al., 2018).

Moreover, commercially available AC adsorbents are mostly made from unrenewable materials such as coal, peat, lignite, etcetera. This, therefore, necessitates the production of efficient, cost-effective, and environmentally safe AC from agricultural by-products, which are readily available in the developing world. The use of these agricultural by-products may also provide a much more sustainable waste management option for the developing world, whilst helping provide safe drinking water to rural communities (Jjagwe et al., 2021).

### **Spectroscopy**

Spectroscopy involves the study of the properties of matter as it interacts with electromagnetic radiation. The different types of electromagnetic radiation, are arranged in an order of increasing or decreasing wavelength on the electromagnetic spectrum (Figure 1) with the following categories: gamma rays, x-rays, ultraviolet (UV) radiation, visible radiation, infrared radiation,

microwave radiation, and radio waves. Based on the category of electromagnetic radiation in use, there are different types of spectroscopic techniques, which rely on the measurement of radiation intensity (Hussain, 2019; Pavia, Lampman, & Kriz, 2001). The interaction of matter with X-rays, infrared radiations, ultraviolet (UV), and visible radiation, gives rise to different spectroscopic techniques (Amuah, 2020; Pavia et al., 2001).

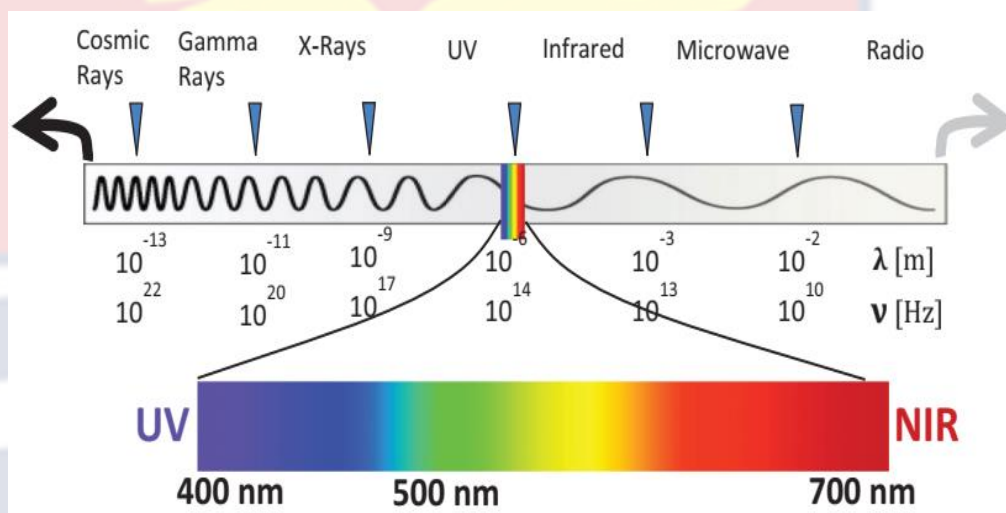


Figure 1: The electromagnetic spectrum (Chemistry LibreTexts, 2019)

This study is however, focused on the use of X-ray diffraction (XRD) spectroscopy, Fourier Transform Infrared (FTIR) Spectroscopy, UV-visible absorption and transmission spectroscopy, Laser-Induced Fluorescence (LIF) spectroscopy, and polarized light microscopy techniques, for the characterization and testing of some prepared GAC adsorbents for DOM removal in surface water samples.

### X-ray diffraction spectroscopy

X-ray diffraction (XRD) spectroscopy is a rapid, non-destructive analytical technique that is primarily used for the phase identification of a powdered sample. This technique works by irradiating a sample with X-rays (0.154 nm), thus causing elastic scattering since the same wavelength of



radiation is re-emitted after interacting with the sample. The interaction of the X-rays with the sample causes the production of a regular array of spherical waves which are scattered in all directions. The scattered waves mostly interfere destructively, with only a few constructive interferences, which only occur when the system conditions satisfy Bragg's law (Dutrow, 2022).

Bragg's law generally relates the wavelength of any electromagnetic radiation to the diffraction angle as well as the lattice or d-spacing in a crystalline sample. For diffraction to occur, Bragg's law requires the angle of incidence to be equal to the angle of scattering. It also requires the path difference to be equal to an integer number of wavelengths. To establish Bragg's law, consider two parallel lattice planes of a crystal that are a distance  $d$  apart (Figure 2).

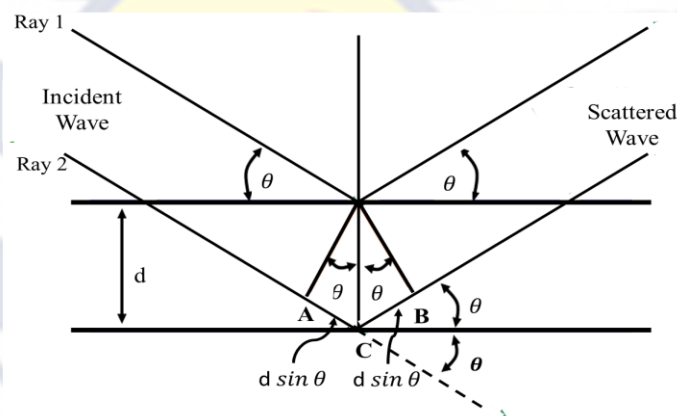


Figure 2: X-ray diffraction at a crystal surface (Liao, 2013)

When two rays from an incident X-ray, rays 1 and 2, reach the first and second planes of the crystal respectively, they are reflected according to the first law of reflection, with a path difference of  $2d\sin\theta$ , where  $\theta$  is the angle of refraction. The distance that will be travelled by ray 2 upon reaching the second plane, from point A to O, then O to B is  $AO + OB$ . The distance made by ray 2 is, however, longer than the path taken by ray 1 after interacting with the first



plane. Hence, if the distance traversed by ray 2 is an integral multiple of the wavelength of the incident X-ray, constructive interference occurs, and the distance is given by equation (1).

$$AO + OB = n\lambda \quad (1)$$

From Figure 2, the distance, AO is expressed as shown in equation (2). Substituting equation (2) into equation (1) gives the required diffraction condition known as Bragg's law as shown in equation (3). Where  $\lambda$  is the wavelength of the X-rays,  $d$  is the distance between the planes,  $\theta$  is the Bragg angle, and  $n$  is an integer.

$$AO = OB = d \sin \theta \quad (2)$$

$$n\lambda = 2d \sin \theta \quad (3)$$

The diffraction peaks of an XRD spectra are normally converted to the  $d$ -spacings which helps in the identification of the minerals present in the sample. This is possible because each mineral has a set of unique  $d$ -spacings, and is achieved by comparing the  $d$ -spacings with a standard reference pattern (Dutrow, 2022).

X-ray diffraction can also be employed in determining the mean crystallite size of a powdered sample using the Scherrer equation as given in equation (4), where  $\beta$  is the full width at half maximum (FWHM) of the diffraction peaks measured in radians,  $k$  is a constant given to be 0.9,  $\lambda$  is the wavelength of the incident X-rays which is 0.154 nanometre (nm), and  $\theta$  is the Bragg angle ( $2\theta/2$ ) which also represents the peak positions (Mensah, Abbas, Azis, Khamis, & Mamoun, 2019).

$$D = \frac{k\lambda}{\beta \cos \theta} \quad (4)$$

This estimated crystallite size is however an approximation since the FWHM can be affected by several factors (crystal lattice imperfections or inhomogeneous strains), especially in granular samples ( $> 0.2 \mu\text{m}$ ). The estimated crystallite size is also different from the average particle size of the prepared adsorbents since crystallites combine to form grains, which also combine to form particles. Moreover, the inverse correlation between particle size and the surface area is also well established as shown in equation (5), where  $D_p$  is the particle size,  $\rho$  is the bulk density of the powdered sample, and SSA is the specific surface area (Mensah, Abbas, Azis, Khamis, & Mamoun, 2019).

$$D_p = \frac{6}{\rho \times \text{SSA}} \quad (5)$$

In a recent study, Lee, Lee, and Roh (2021), examined changes in the structural parameters of  $\text{CO}_2$ -activated carbon black using XRD spectroscopy. The results showed a significant effect of the activation process on the structure of the carbon black sample, by showcasing the development of micropores, large internal pores, and a maximum burn-off of 83.2%. A clear difference was observed between the micro-crystallites of the carbon black sample and that of graphite.

Farma, Wahyuni, and Awitdrus (2019), on the other hand, evaluated the microstructure of some AC samples using the XRD technique. The Scherrer equation was also employed by Mensah et al. (2019) in estimating the average crystalline sizes of recycled hematite ( $\alpha\text{-Fe}_2\text{O}_3$ ) nanoparticles. An inverse correlation between the average crystallite sizes of the recycled  $\alpha\text{-Fe}_2\text{O}_3$  nanoparticles and the milling time was observed. That is, the longer the milling time, the smaller the crystallite sizes of the sample. These researchers and several others, emphasized the efficient use of the XRD spectroscopy in the

structural characterization of different samples, thus showcasing its unique applicability in adsorbent characterization (Ahamed, Chandrasekaran, & Kumar, 2013; Bakti & Gareso, 2018; Dewi, Agusnar, & Alfian, 2018; Farma et al., 2019; Lee et al., 2021; Mensah et al., 2019; Nwosu, Ajala, Owoyemi, & Raheem, 2018).

### **Fourier transform infrared spectroscopy**

Infrared (IR) spectroscopy involves the interaction of IR radiation with matter and serves as a complementary technique to XRD (Pavia et al., 2001). This technique is precise, non-destructive, and essential in determining the structure of molecules present in a sample. Recent developments in IR spectroscopy involve the imaging of tissues using IR microscopy. This technique has also been applied in the fields of cellular components mapping, in attempts to differentiate between normal and abnormal cells, protein analysis, and in photosynthesis research (Berthomieu & Hienerwadel, 2009).

IR spectroscopy relies on the principle that, a particular type of bond can only be found in a certain small portion of the infrared region which is a vibrational state. In IR spectroscopy, an incident IR radiation (2.5 to 14 microns) passes through a sample, with some of the radiation being absorbed by the sample and some transmitted. The transmitted radiation is then recorded as an IR spectrum, which is a plot of measured radiation intensity against the wavenumber. Different molecules produce different spectra, which makes each spectrum unique, and hence helps in distinguishing between molecules in a sample (Amuah, 2019; Pavia et al., 2001; Pavia, Lampman, Kriz, & Vyvyan, 2004).

IR spectroscopy is primarily based on the fundamental design of a Michelson interferometer (Figure 3), where an incident IR radiation is sent through a 50-50 beam splitter, with half of the intensity going to a fixed mirror and the other half to a mirror moving with a constant velocity. These two beams are then reflected and recombined (now with a path difference between the beams) to construct an interference pattern. However, to obtain a full spectrum as a function of wavenumber, Fourier transform is performed on the interference pattern, thus giving it the name, Fourier transform Infrared spectroscopy (Berthomieu & Hienerwadel, 2009; Birkner & Wang, 2023; Pavia et al., 2004).

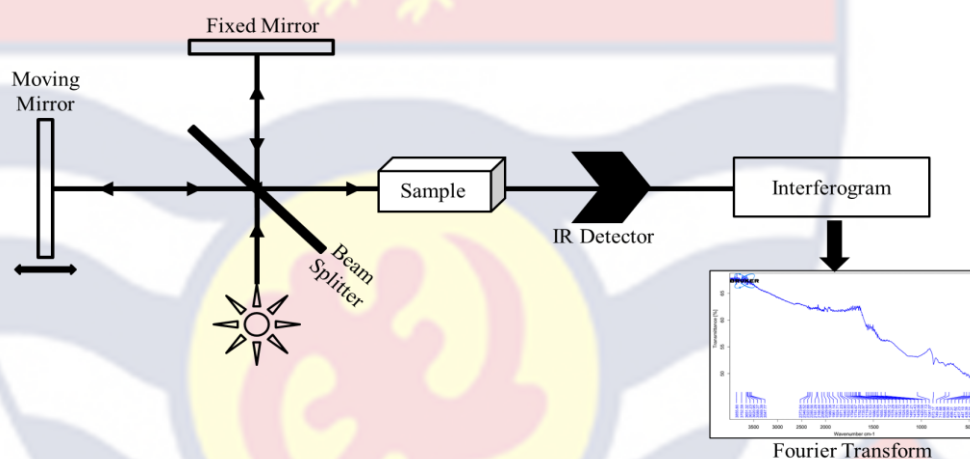


Figure 3: Principle of Fourier transform infrared spectroscopy

In the field of water purification, FTIR is mostly employed in the characterization of filter media and other adsorbents. Bakti and Gareso (2018), employed this technique in the characterization of  $\text{ZnCl}_2$  and  $\text{Na}_2\text{CO}_3$  activated carbon, and the results indicated a successful discrimination between the AC adsorbents considered in the study. (Shepel et al., 2015), also took advantage of the unique properties of FTIR to study how the intensity of the least overlapping IR bands of some AC adsorbents is affected by adsorbent preparation methods and FTIR spectrum recording conditions (Bakti & Gareso, 2018; Shepel et al., 2015).



The work of Nwosu et al. (2018), however, coupled FTIR with the XRD technique, in characterizing modified bentonite and different kaolin clay samples, to assess the adsorbent efficiency in contaminant removal from water. The FTIR spectra for each clay sample exhibited the presence of different functional groups, thus revealing the effect of the modification process on the clay samples. Several other studies emphasized the importance and precision of FTIR spectroscopy in adsorbent characterization, especially in the field of water purification (Das, Samal, & Meikap, 2015; Joshi, 2018; Zheng, Song, Meng, & Fang, 2016).

### **Ultraviolet-visible absorption and transmission spectroscopy**

Ultraviolet (UV)-visible absorption spectroscopy is one of the oldest spectroscopic techniques that deal with the evaluation of micro and semi-micro parameters of the different analytes in a sample. This technique measures the aftermath of the interaction between electromagnetic radiation in the UV and/or visible regions and the absorbing species in a sample. UV-visible absorption spectroscopy is also based on the principle that the higher the population of absorbing species and the efficiency with which they absorb radiation, the greater the extent of absorption.

This basic principle of absorption gave birth to the Beer-Lambert law, which is a combination of Beer's and Lambert's hypotheses on absorption. The Beer-Lambert law is based on the observation that, when electromagnetic radiation is incident on a liquid sample containing some absorbing species, the absorbance is directly related to the concentration of absorbing species, also known as the chromophores, and inversely related to the transmitted intensity, also known as transmittance.



According to Lambert's law, the rate of decrease in intensity,  $-\frac{dI}{dx}$  of an incident electromagnetic radiation of a single wavelength as it passes through a homogeneous sample of small thickness,  $dx$  is as shown in equation (6) (Gryczynski & Gryczynski, 2020)

$$-\frac{dI}{dx} \propto I \quad (6)$$

Rewriting equation (6) by introducing a constant of proportionality,  $\sigma$  gives equation (7), where  $\sigma$  is the adsorption cross section.

$$-\frac{dI}{dx} = \sigma I \quad (7)$$

Integrating equation (7) and introducing an integration constant,  $C$  gives equation (8).

$$-\ln I = \sigma x + C \quad (8)$$

But, at  $x = 0$ ,  $I = I_0$  (incident monochromatic light), hence  $C = -\ln I_0$ . Substituting the expression for  $C$  into equation (8) gives equation (9), which can be rewritten as in equation (10) (Gryczynski & Gryczynski, 2020).

$$\ln \frac{I}{I_0} = \sigma x \quad (9)$$

$$I = I_0 e^{-\sigma x} \quad (10)$$

A study by Sefa-Ntiri et al. (2014), employed Lambert's technique in measuring the optical turbidity of ground and surface water samples. In this study, Lambert's law, as in equation (10), was used to determine the optical turbidity of some ground water samples, represented by  $\sigma$  in equation (10). The results indicated a general increase in optical turbidity with increasing dissolved and suspended solids concentration in the water samples.

Beer on the other hand, asserted that the absorbance of a sample is not only dependent on the concentration of absorbing species but also on the

interaction period ( $t$ ) between the radiation and the sample; that is, the shorter the period of interaction the higher the transmittance and hence, the lower the absorbance. However, with the speed of light ( $c$ ) being constant, the period of absorption is also proportional to the distance travelled within the sample, which is the sample cell path length,  $l$ .

Consequently, a combination of Beer and Lamberts' law is expressed in equation (11) for a given wavelength of electromagnetic radiation, where  $A$  is the absorbance,  $C$  is the molar concentration of the solute in Molarity,  $l$  is the path length of the sample cell in centimetres and  $\epsilon$  is the molar absorptivity.

$$A = \epsilon Cl \quad (11)$$

The Beer-Lambert's law, as expressed in equation (11), is however, only helpful in measuring the concentration of a particular sample, if the wavelength at which the chromophores absorb radiation, as well as the molar absorptivity, is known (Hardesty & Attili, 2010; Hussain, 2019). This expounds the wavelength dependence of the molar absorptivity, which is a spectroscopic characteristic property of the chromophores in the sample (Gryczynski & Gryczynski, 2020; Yunus, 2020).

Coloured Dissolved Organic Matter (CDOM), is the part of DOM that absorbs in the UV and visible regions of the EM spectrum. CDOM is a significant constituent (10 – 90%) of DOM in surface or groundwater, thus a good measure of the total DOM concentration in a surface water sample. The absorption of light by CDOM decreases exponentially with increasing wavelength as illustrated by Beer-Lambert's law in equation (11).

However, aromatic groups are the major constituents of CDOM, which associates it more with the humic component of DOM. This makes UV visible absorbance an approximate measure of the total DOM concentration in a

particular sample. Some of the UV-visible absorption parameters used in the effective characterization of DOM include; absorbance at 254 nm, spectral slope and spectral ratio, and specific UV absorbance (SUVA); that is, the absorbance at 254 nm normalized to DOC concentration (Moona, 2021).

Research also showed that absorbance at 254 nm or wavelengths between 280 – 350 nm correlate well with DBP formation rates. Other recent studies (e.g., Moona (2021)) also observed that the absorbance at 272 nm serves as the best indicator of total organic halogen (TOX) concentration in water (Bolton, 2003; Carstea et al., 2020; Moona, 2021).

### **Fluorescence spectroscopy**

Fluorescence is one of the leading spectroscopic techniques in the different disciplines of science. It is a form of luminescence that occurs when light is emitted from a substance due to electronically excited energy levels. Fluorescence generally occurs in singlet excited states, where the electron in the higher energy state is paired, by opposite spin with another electron in the lower (ground) energy orbital. This leads to the return of the electron to the lower energy state, thus causing the rapid emission of a photon. The absorbing species in a sample that fluoresces are known as fluorophores. With laser-induced fluorescence (LIF), the fluorophores of a sample are excited to a higher energy level with a laser light source. Depending on the type of laser and detector used in fluorescence, LIF can be referred to as emission or excitation LIF. In the case of the excitation LIF, a tuneable laser source is used, thus allowing the excitation wavelengths to vary. Whereas, in the emission LIF case, a fixed pump laser is used to give an emission spectrum of the sample, which is then separated into the different detected wavelengths using a monochromator.

LIF spectroscopy can also be classified as continuous wave LIF (CW-LIF); which uses a continuous laser for excitation, or time-resolved LIF (TR-LIF); where a pulsed laser source is used to induce fluorescence. The CW-LIF is employed when only the spectral information of a sample is needed. The TR-LIF, however, provides very useful information such as the lifetimes of the chemical species present (Gryczynski & Gryczynski, 2020).

These classes of LIF can further be broken into point measurement techniques or imaging geometry techniques. The point measurement technique involves only a small area of the sample, where the spectroscopic information is collected using an optical fibre. The imaging geometry, on the other hand, uses a camera to take images of the sample under investigation (Edinburgh Instruments, 2022; Lakowicz, 2006; Murphy, Graeber, Stedmon, & Bro, 2013; Gryczynski & Gryczynski, 2020).

The part of DOM that can fluoresce, when excited with either UV or visible light is known as fluorescent dissolved organic matter (FDOM). The concentration of FDOM in a water sample is easily determined using the specific optical properties of the fluorophores present in the sample since the molecular structure of these fluorophores controls the wavelengths at which fluorescence occurs. The humic-like and protein-like components of FDOM, as well as their corresponding concentrations, can be determined from the fluorescence emission spectra using the wavelength and intensity of the prominent peak (s). Research shows that the humic-like component occurs at much longer emission wavelengths (>350 nm) compared to the protein-like component which occurs at much shorter emission wavelengths (<350 nm). In effect, the rapid and compositional characterization of DOM with high efficiency, sensitivity, and minimal sample preparation can be achieved using



fluorescence spectroscopy. This technique provides very valuable information on the nature and composition of DOM and has been employed by several researchers in DOM characterization and filter performance assessment using different water treatment techniques (Barker, Dubnick, Lyons, & Chin, 2013; Sweetman et al., 2018; Watson, Farré, Leusch, & Knight, 2018).

Some earlier studies employed fluorescence spectroscopy in exploring the differences in DOM concentration in surface and groundwater, although not very focused on assessing the efficiency of different adsorbents (Chiu et al., 2019). Aziz et al. (2018), including several other researchers (Carstea et al., 2020; Yamada et al., 2019) employed fluorescence spectroscopy, mostly with excitations in the blue region (430 - 500 nm) as rapid methods in evaluating the quality of different water samples. The results of these studies, indicated a good correlation between the fluorescence spectra and DOM concentration, thus making fluorescence spectroscopy a good proxy for DOM or dissolved organic carbon (DOC) concentration in water.

A study by Sefa-Ntiri et al. (2020), also used the LIF technique in assessing DOM contamination levels of different well water samples on a seasonal basis. The study revealed the contribution of the humic component of DOM to the FDOM concentration of the water samples. Thus, indicating a direct relation between FDOM concentration and fluorescence intensity.

Moona (2021) further emphasized the fact that fluorescence spectroscopy is an effective method for tracking DOM changes through biological filtration, due to its high analytical precision and sensitivity. Several other studies, also demonstrated the applicability of fluorescence spectroscopy, in tracking water quality changes in terms of FDOM concentration (Heibati et



al., 2017; Korak, Rosario-Ortiz, & Scott Summers, 2015; Moona, 2021; Wasswa, 2018; Yang et al., 2019).

Kim et al. (2018), on the other hand, also looked at detecting organic compounds in water using a UV LED (280 nm) based spectroscopic system coupled with a photodetector. The results indicated a very good correlation ( $R^2 = 0.998$ ) between the LED-based spectroscopic system and the photodetector absorbance results (Kim, Ji, & Eom, 2018).

### **Polarized light microscopy**

Polarized light microscopy is a spectroscopic technique used in the characterization and identification of a variety of materials, especially biological materials. It also provides information on the colour, structure, as well as absorption, and compositional characteristics of different materials. The process of polarized light microscopy involves the illumination of the sample with polarized light using the reflection or transmission mode.

Natural or artificial light sources usually produce naturally unpolarized light, which comprises over a zillion light rays vibrating in all possible directions or planes (Figure 4). These unpolarized light rays become linearly polarized after passing through a polarizer, which only allows the passage of light rays vibrating in one direction or plane as illustrated in Figure 4.

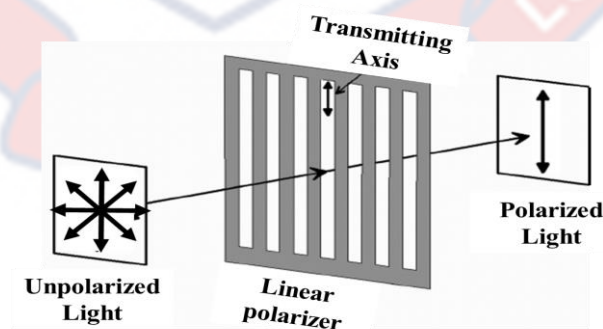


*Figure 4:* Polarization of unpolarized light with a linear polarizer (Ferris et al., 2010)

Unpolarized light could also be circularly or elliptically polarized depending on the type of polarizer used (Bagnell, 2012; Rančić, 2019). Ferris et al. (2010), successfully illustrated the potential use of polarized light in colposcopy examinations, and observed its importance in enhancing the evaluation and detection of cervical neoplasia (Ferris et al., 2010).

### **COMSOL Multiphysics Simulation**

Computer simulation, in recent times, has become an essential and powerful tool used in mimicking and predicting the physical behaviour of a physical model. Researchers in this field are open to various simulation techniques ranging from basic computer programming languages to advanced packages. These simulation techniques are, however, mostly questioned on accuracy and reliability due to the assumptions made in realising an idea or design. Moreover, since computer simulations are generally aimed at simply mimicking a real-life idea or law in a virtual world, the amount of simplification that takes place in realising the idea determines the accuracy of the virtual model. Hence, in the quest to attain accurate virtual models, researchers tend to look for simulation environments with extraordinary features that allow the addition of all possible physical effects. One simulation software that meets this requirement by far, is COMSOL Multiphysics (Griesmer, 2013; Vajdi, Moghanlou, Sharifanajazi, Asi, & Shokouhimehr, 2020).

COMSOL Multiphysics provides a user-friendly environment with the capability of investigating a wide range of physical laws or ideas. This is made possible with its Multiphysics feature, which allows the simulation of different physical ideas simultaneously. A typical and all-important step in this Multiphysics based simulation technique is the creation of a discrete

mathematical model and solving it numerically. These mathematical models are basically, a set of coupled equations which are categorized into; Governing equations, auxiliary equations, and boundary conditions. The governing equations are, however, the most essential in properly describing the major physical idea or law to be implemented.

Multiphysics-based simulation techniques are generally implemented numerically, using discretization methods like the Finite Element Method (FEM), Boundary Element Method (BEM), Perturbation Method (PM), Finite Volume Method (FVM), or Finite Difference Method (FDM). The governing equations, which are purely partial differential equations (PDEs) in the case of COMSOL Multiphysics, are designed to be solved with the FEM (Vajdi et al., 2020).

Most time and space-dependent problems in physics are generally described using partial differential equations (PDEs). The PDEs for some problems with certain geometries, cannot be solved accurately using analytical methods. This flaw, calls into play, the use of different discretization techniques to approximate the PDEs with numerical equations which can be solved using numerical methods. The solutions to these numerical equations are, therefore, approximations to the solutions of the actual PDEs. This process of numerically solving PDEs with the help of different discretization techniques is often carried out using the finite element method (FEM) (COMSOL Multiphysics, 2017).

The practical application of FEM in computer simulation software is referred to as Finite Element Analysis (FEA). In using FEA software, there are some major things to consider, such as; a computer-aided design (CAD), and a vast knowledge of the relevant physics and specific material properties, including system constraints. Providing these details helps improve accuracy in

mimicking real-life designs and behaviours. One other thing that can influence the accuracy and reliability of a FEA model, is the finite element mesh size, which is used to subdivide the model into elements for easy computation. The relationship is that; as the mesh size becomes smaller, the numerically computed solution gets closer to the true solution. Hence, most researchers go through a series of mesh refinement techniques (reducing the element size, increasing the element order, etcetera) in their quest to achieve accurate and reliable simulation results.

COMSOL Multiphysics is one of the best software that encompasses this numerical procedure of the FEA. This modelling simulation software is also generally accepted as a reliable and scientifically trusted simulation software in physics and engineering disciplines (Munir & Spirka, 2013; Khan et al., 2020).

### **COMSOL Multiphysics interface and features**

One of the best features of COMSOL Multiphysics is the ability of the user to interface different types of physics in one simulation. COMSOL Multiphysics also allows users to integrate its interface with other peripheral simulation and engineering software interfaces with ease for a unified workflow. Some of these other peripheral simulation and engineering software interfaces include Matlab, AutoCAD, etcetera. With its vast material library and multi-plot features, along with the computer-aided design (CAD) environment, COMSOL also allows users to design models, specify model material, and simulate real-life ideas with high precision. The general steps in a typical COMSOL model include; geometrical modelling, meshing, and postprocessing.

Geometrical modelling is the first step in creating a COMSOL model. The COMSOL Multiphysics interface provides several geometry tools and



functionalities, thus enhancing the speed and accuracy of the model. The general steps in creating a geometry include; building geometry primitives, using Boolean, partition, and transformation operations to manipulate existing geometries, and specifying actions to deal with overlapping objects using “Form Union or Form Assembly” (Halliday, 2017).

Meshing, on the other hand, is an essential step in obtaining accurate and timely results. There are nine built-in size parameter sets for meshing in COMSOL Multiphysics, which range from extremely fine to extremely coarse. The default mesh size is the physics-controlled mesh with normal element size. Several adjustments can however be made, using the five mesh modification parameters; maximum or minimum element size, maximum element growth, curvature factor, and resolution of narrow regions (Griesmer, 2014).

The post-processing capabilities of COMSOL Multiphysics include very flexible techniques that help in understanding and validating a model. These post-processing techniques also aid the performance of operations on data sets, the creation of deformations that showcase realistic displacements, the definition of specific expressions, and the interpretation of results (Griesmer, 2014).

The most desired of all these features of COMSOL is the ability to simulate or mimic real-life ideas with such high accuracy that, the effect of each decision can be ascertained. This is made possible with the available tools in COMSOL that are used to replicate most physics phenomena such as; AC/DC, acoustics, chemical species transport, electrochemistry, fluid flow, heat transfer, optics, plasma, radio frequency, semiconductor, structural mechanics, and mathematics. With all these features available in COMSOL, the era of



expensive prototype testing is over, since each phenomenon, idea, or design can be mimicked in a digital environment with the ability to make changes at no extra cost (Multiphysics, 2022).

### **Fluid flow**

Fluid, according to Rodgers (2013), is a liquid or a gas that can deform continuously when it is under the action of an applied shear stress. A fluid will continue in its deformed state for some time even when the shear stress is removed. Fluids generally comprise liquids and gasses, as well as some forms of plasma. When a fluid is subject to different unbalanced forces, it moves, and this motion is termed fluid flow under fluid dynamics. Fluids also flow when there is a pressure difference between two points, and the flow occurs from regions of higher pressure to lower pressure.

The two major types of fluid flow are the laminar and turbulent flow. However, fluid flow can also be described as; steady or unsteady; uniform or non-uniform; compressible or incompressible; rotational or irrotational, and can be in either one-, two- or three-dimensions. For fluid flow in a pipe, the laminar flow regime is characterized by a highly ordered fluid motion with smooth streamlines. Turbulent flow in pipes, is, however, characterized by a highly disordered motion of the fluid with fluid velocity fluctuations. The flow regime experienced in everyday practice is completely turbulent, with laminar flow occurring for viscous fluids in narrow pipes.

A fluid flow can transition from laminar to turbulent by fluctuating between the two regimes for a period of time and over some region of space, before fully turning to one regime. This transition depends on the nature of the pipe (material, surface roughness, and geometry) as well as the surface

temperature and fluid type. Osborne Reynolds, in 1883, discovered a relationship between the two flow regimes and observed that each regime depends on a dimensionless ratio which he later called the Reynolds number (Re) (Cengel & Cimbala, 2006; Kudela, 2022).

This ratio is as expressed in equation (12) for circular pipes of uniform diameter, where  $D$  is the diameter of the pipe,  $V_{\text{avg}}$  is the average flow velocity, and  $\nu = \mu/\rho$  is the kinematic viscosity, with  $\mu$  being the dynamic viscosity and  $\rho$  the volume density of the fluid.

$$\text{Re} = \frac{\text{inertial forces}}{\text{viscous forces}} = \frac{V_{\text{avg}}D}{\nu} = \frac{\rho V_{\text{avg}}D}{\mu} \quad (12)$$

Fluid flow is said to be laminar at low Re ( $\text{Re} < 2100$ ); that is when the viscous forces are larger compared to the inertial forces, and are thus able to prevent the rapid random movement of the fluid. But when the viscous forces are much less compared to the inertial forces and are unable to prevent the rapid random movement of the fluid, Re becomes high ( $\text{Re} > 4000$ ) and the flow becomes turbulent (Cengel & Cimbala, 2006; Kudela, 2022).

Flow compressibility is another important way of describing fluid flow, which depends on the Mach number (M) as shown in equation (13), where  $V$  is the fluid velocity and  $c_s$  is the speed of sound in the fluid.

$$M = \frac{\text{fluid velocity}}{\text{speed of sound}} = \frac{V}{c_s} \quad (13)$$

A fluid is incompressible for values of  $M < 0.3$ , and compressible when  $M > 0.3$ . Whilst compressible fluids have changing volume, incompressible fluids have a constant volume, and hence a constant density, such as water.

Fluid flow is generally governed by a form of Newton's second law for fluids, known as the Navier-Stokes (NS) equation. This equation can be

expressed for compressible or incompressible Newtonian fluids. In the first case, the NS equation is expressed as shown in equation (14).

$$\rho \left( \frac{\partial \mathbf{u}}{\partial t} + \mathbf{u} \odot \nabla \mathbf{u} \right) = -\nabla p + \nabla \left( \mu (\nabla \mathbf{u} + (\nabla \mathbf{u})^T) - \frac{2}{3} \mu (\nabla \odot \mathbf{u}) \mathbf{I} \right) + \mathbf{F} \quad (14)$$

Comparing equation (14) to Newton's second law ( $m\mathbf{a} = \mathbf{F}$ ), the density of the fluid,  $\rho$  is proportional to the mass ( $\rho \propto m$ ), where  $\frac{\partial \mathbf{u}}{\partial t} + \mathbf{u} \odot \nabla \mathbf{u}$  represents the acceleration, with  $\mathbf{u}$  representing the velocity of the fluid flow.  $p$  and  $\mu$  are the fluid pressure and dynamic viscosity respectively. The right side of equation (14) represents the total forces acting on the fluid; with the first  $-\nabla p$ , second  $\nabla \left( \mu (\nabla \mathbf{u} + (\nabla \mathbf{u})^T) - \frac{2}{3} \mu (\nabla \odot \mathbf{u}) \mathbf{I} \right)$ , and third  $\mathbf{F}$  terms representing the pressure forces, the viscous forces, and the external forces on the fluid respectively.

Whilst the NS equation shows the conservation of momentum, the continuity equation, which is solved alongside the NS equation, illustrates the conservation of mass, as shown in equation (15).

$$\frac{\partial \rho}{\partial t} + \nabla \odot (\rho \mathbf{u}) = 0 \quad (15)$$

However, for incompressible fluid flow, equation (15) becomes equation (16) since the fluid density  $\rho$  is constant. Applying equation (16) to (14) gives the NS equation for incompressible flow as shown in equation (17).

$$\rho (\nabla \odot \mathbf{u}) = 0 \quad \therefore \nabla \odot \mathbf{u} = 0 \quad (16)$$

$$\rho \left( \frac{\partial \mathbf{u}}{\partial t} + \mathbf{u} \odot \nabla \mathbf{u} \right) = -\nabla p + \nabla \left( \mu (\nabla \mathbf{u} + (\nabla \mathbf{u})^T) \right) + \mathbf{F} \quad (17)$$

Equation (17) transforms to equation (18) under the laminar flow regime, with very low  $Re$  ( $Re \ll 1$ ) and hence negligible inertial forces on the left side of equation (14), and assumably no external forces (Negligible gravity) (Bazzi, 2020; Dobek, 2012).

$$0 = -\nabla p + \nabla(\mu(\nabla u + (\nabla u)^T)) \quad (18)$$

The several physics interfaces under fluid flow in COMSOL are employed in the simulation of the flow and pressure fields of both liquids and gases. The physics interfaces under fluid flow include; single-phase flow, thin film flow, multiphase flow, porous media and subsurface flow, non-isothermal flow, high Mach number flow, rarefied flow, particle tracing, and fluid structure interaction. This study will however, concentrate on the free and porous media flow under the porous media and sub-surface flow physics interface.

### **Free and porous media flow**

Water filtration through a porous adsorbent and/or substrate is easily described by the free and porous media flow physics interface in COMSOL. Free and porous media flow is governed by the Brinkman equation, which appears to be a combination of the NS equation and Darcy's law. Darcy's aspect of the Brinkman equation, governs the slow flow in porous media, whilst the fast flow in the free channel is described by the NS equation. The free and porous media flow interface is mostly used to compute fluid velocity and pressure fields of single-phase flow where the free flow is connected to a porous media domain (COMSOL Multiphysics, 2020).

Henry Darcy formulated his law in 1856 based on his experiments on dead-end water filtration through sand beds. This law only applies when the gradient in hydraulic potential becomes the driving force for the movement of fluids in the porous medium. Darcy's law is also valid only for slow, viscous flow with  $Re < 1$ , and is expressed as in equation (19), where  $Q$  is the volumetric flow rate in  $m^3/s$ ;  $k$  is the permeability of porous medium in  $m^2$ ;  $\mu$  is the fluid viscosity in Pa.s;  $A$  is the cross-sectional area of the porous media in  $m^2$ ;  $p_b$ –

$p_a$  is the pressure drop across the medium in Pa; and  $L$  is the length of the sample in metres (Gonite, 2015).

$$Q = \frac{-kA(p_b - p_a)}{\mu L} \quad (19)$$

Coupling Darcy's law with the NS equation gives the Brinkman equation as shown in equation (20) (Gonite, 2015), where  $\rho$ ,  $u$ ,  $\eta$ ,  $k$ ,  $p$ , and  $F$  represent the density, velocity vector, viscosity, permeability, pressure, and the force term respectively (Yan, Liu, & Jing, 2018).

$$\rho \frac{\partial u}{\partial t} - \nabla \cdot \eta (\nabla u + (\nabla u)^T) - \left( \frac{\eta}{k} u + \nabla p - F \right) = 0 \quad (20)$$

The above-mentioned studies, to the best of my knowledge, only made use of the optical properties of DOM, without much emphasis on evaluating the efficacy of different GAC adsorbents prepared from different agricultural by-products. The present study will ultimately help optimize the cost and efficiency of locally prepared adsorbents for point-of-use water purification. This study will also focus on developing a unique GAC preparation method, which will be tested and confirmed using different spectroscopic techniques.

### Chapter Summary

This chapter reviewed some literature on spectroscopy, giving prominence to X-ray diffraction spectroscopy, Fourier transform infrared spectroscopy, UV-visible absorption, and transmission, as well as laser-induced fluorescence. The application of these techniques in water treatment using GAC with emphasis on DOM removal has been discussed. The working principle and previous studies on some adsorbent characterisation techniques were also deliberated on. A brief introduction to COMSOL Multiphysics was also given.



## CHAPTER THREE

### MATERIALS AND METHODS

#### Introduction

This chapter focuses on outlining the methods and techniques adapted for this study. The first part elaborates more on the preparation and characterisation processes of the AC adsorbents using XRD and FTIR, emphasising the raw materials used and the activation chemicals. The second part describes the four spectroscopic techniques: UV-visible absorption, LED-Induced Transmission (LED-IT), Laser-Induced Fluorescence (LIF), and polarized light microscopy, used in testing the prepared adsorbents. The third part describes how COMSOL Multiphysics was used in modelling and simulating the AC adsorbent-based filtration system.

#### Preparation of Adsorbents

Organic agricultural by-products like coconut shells and samples of shea nut tree and cassia siamea tree branches (Figure 5) were used as raw materials to prepare the GAC adsorbents using the protocol summarised in Appendix A.

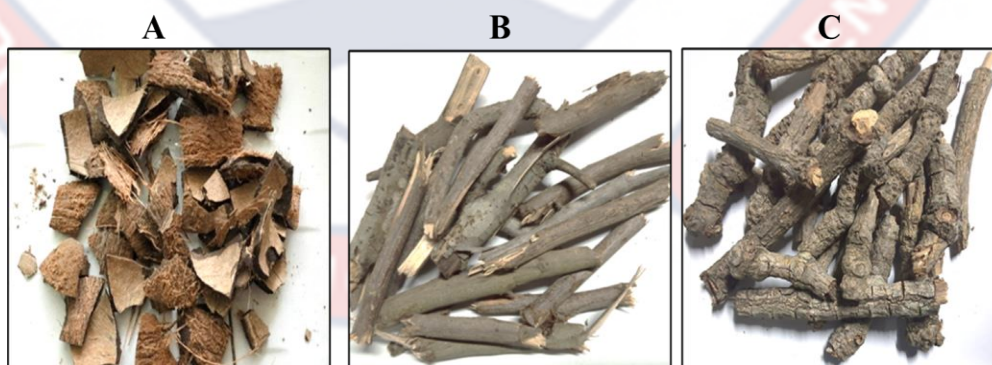


*Figure 5:* Samples of organic agricultural by-products for adsorbent preparation (A) Coconut shells, (B) Cassia siamea tree branches, and (C) Shea nut tree branches

The coconut shells were collected from local coconut oil vendors in Cape Coast, and the tree samples were collected from nearby farmlands in Wa, the upper west region of Ghana, where they are in abundance. Each raw sample was crushed into smaller pieces, sun-dried, and divided into two groups. Conventional and furnace carbonisation methods were used on each group of crushed raw materials. The conventional carbonisation was carried out by placing the raw sample in a shallow dry hole (40 cm radius and 50 cm in depth) and allowing it to burn. After a few minutes of burning, the hole was covered with leaves and topped up with zinc sheets, and sand, leaving out a small section as a smoke outlet (Figure 6). The carbonised char was then dug up after 24 hours, rinsed with distilled water and sun-dried.



*Figure 6:* Conventional carbonisation of raw adsorbent material (A) Initial burning process and (B) Carbonisation process

In the case of the furnace carbonisation technique, each sample was placed in a ceramic cup, sealed with aluminium foil, and then placed inside a marble furnace with a temperature range of 30 to 3000 °C (Nabertherm, Germany). The marble furnace used is as shown in Figure 7. The temperature was set to 500 °C and the samples were carbonised for 2 hours. The carbonised pieces in each group were left to cool, after which each sample was crushed into powdered form and sieved using a mesh size of 0.5 mm.



Figure 7: Nabertherm industrial furnace (Nabertherm, Germany)

Each grouped sample (conventionally and furnace carbonised group) was divided into two subgroups. One of the two subgroups was chemically activated using  $\text{CaCl}_2$  and the other with  $\text{NaCl}$ . These activations were done by soaking each subgroup of char samples in 3.6 M  $\text{CaCl}_2$  or  $\text{NaCl}$  for 24 hours. The concentration of the  $\text{CaCl}_2$  and the  $\text{NaCl}$  was calculated using equation (21), where  $C$  is the molar concentration of the solute in a solution,  $m$  is the mass of the solute in grams,  $V$  is the volume of solvent in liters, and  $M_w$  is the molecular weight in g/mol, obtained from the molecular formula (PhysiologyWeb, 2017).

$$C = \frac{m}{VM_w} \quad (21)$$

Hence, different masses of the  $\text{CaCl}_2$  and the  $\text{NaCl}$  were used to achieve the same molar concentration for each solution. But generally, the activation process in his study involves a solute-to-solvent (water-to- $\text{CaCl}_2$  or  $\text{NaCl}$ )-to-char ratio of 1.0:2.5:1.25. It was envisaged that this ratio would result in high adsorbent efficiency based on the observations and conclusions of previous studies by Bergna et al. (2020), Kumar et al. (2020), Kwasi Opoku et al. (2020), and Xing et al. (2020).

The chemical solutions were separated from the char and each sub-sample was then activated in an oven at 200 °C for 3 hours. The activated



samples were later rinsed several times until a neutral pH was achieved and then oven-dried at 100 °C for 24 hours. This oven-based activation process opened up the pores, thus increasing the porosity of the prepared adsorbents and hence, the surface area for contaminant adsorption (Mohammad Razi, Al-Gheethi, Al-Qaini, & Yousef, 2018; Osman et al., 2019). Twelve (12) GAC adsorbents were prepared, stored in clean, dry containers with tight lids, and labelled as shown in Table 1.

**Table 1: Adsorbent label description**

Adsorbent Label	Label Description
F_CS_CA	Furnace carbonized, and CaCl <sub>2</sub> -activated coconut shells
F_CT_CA	Furnace carbonized, and CaCl <sub>2</sub> -activated Cassia Siamea
F_ST_CA	Furnace carbonized, and CaCl <sub>2</sub> -activated Shea nut tree
F_CS_NA	Furnace carbonized, and NaCl-activated coconut shells
F_CT_NA	Furnace carbonized, and NaCl-activated Cassia Siamea
F_ST_NA	Furnace carbonized, and NaCl-activated Shea nut tree
C_CS_CA	Conventionally carbonized, and CaCl <sub>2</sub> -activated coconut
C_CT_CA	Conventionally carbonized, and CaCl <sub>2</sub> -activated Cassia
C_ST_CA	Conventionally carbonized, and CaCl <sub>2</sub> -activated Shea nut
C_CS_NA	Conventionally carbonized, and NaCl-activated coconut
C_CT_NA	Conventionally carbonized, and NaCl-activated Cassia
C_ST_NA	Conventionally carbonised, and NaCl-activated Shea nut

Source: This study

### Adsorbent Characterisation

The prepared adsorbents were characterized using XRD and FTIR spectroscopic techniques. This characterisation was done to estimate the degree of crystallinity of the different adsorbents and to ascertain their exact absorbance peaks and molecular compositions.

### **X-ray diffraction spectroscopy**

The XRD analysis was carried out using a diffractometer with Cu K-Alpha 1 radiation (1.5406 Å), K-Alpha 2 radiation (1.5444 Å), K-Beta radiation (1.3922 Å), and a K-A2/K-A1 ratio of 0.5. An accelerating current of 40 mA and a 45 kV were used. The GAC adsorbents were each moulded into tablets and placed on the reflection-transmission spinner sample stage to be scanned. The scanning was done with a scan step of 2.4 s and a step size of 0.05 °. The goniometer had a radius of 240 mm with no monochromator placed in front of the incident beam.

The peak patterns were matched with the powder diffraction pattern database to ascertain the composition of each adsorbent sample. The mean crystallite size of each prepared adsorbent sample was then calculated using the Scherrer equation as given in equation (4). The extracted XRD data for the prepared GAC adsorbents were re-plotted in Matlab 2020a and discussed in chapter 4.

### **Fourier transform infrared spectroscopy**

An infrared (IR) spectrum of each GAC adsorbent was taken using a Perkin Elmer FTIR spectrometer (Spectrum Two, USA). The spectrometer is a compact and robust instrument with a lithium tantalate (LiTaO<sub>3</sub>) MIR detector (at room temperature). It has a signal-to-noise ratio (SNR) of 9,300:1. This spectrometer also has a standard optical system with KBr windows for accessible data collection over a spectral range of 8,300 to 350 cm<sup>-1</sup> at an optimum resolution of 0.5 cm<sup>-1</sup>. Another feature of this spectrometer is the availability of diffuse reflectance, specular reflectance accessories, and a computer to visualise the sample data. Each recorded IR spectrum was acquired



from an average of several scans. The background spectrum was first scanned, saved, and used as a reference in taking the spectra of each GAC adsorbent.

### Surface Water Sampling

The surface water samples were collected from river Brimsu (Brimsu), which flows into the Brimsu Dam and serves as the primary raw water source for the Cape Coast branch of Ghana Water Company Limited (GWCL). Duplicate samples were collected at the river and stored in 5-litre gallons with screw caps. The samples in the gallons were then stored in an ice chest for further analysis. The Brimsu river and the Brimsu dam are shown in Figure 8.



*Figure 8:* The source of the unfiltered surface water sample (A) River Brimsu, and (B) River Brimsu flowing into the Dam. P is the point of fetching

### Adsorbent Testing

The prepared GAC adsorbents were each tested on the surface water sample, emphasising the effect of adsorbent mass and retention time on the contaminant removal efficiency of the adsorbent. Three different masses, 10 g, 20 g, and 30 g of each adsorbent, and retention times of 5 minutes, 10 minutes, and 15 minutes were used with 200 millilitres (ml) of the unfiltered surface water sample at room temperature. In other words, the specified mass of a

particular adsorbent was mixed with 200 ml of the unfiltered water sample at room temperature and left for the chosen retention times (5, 10, or 15 min). The mixture was then filtered through a Whatman filter paper (150 mm  $\emptyset$ ) to separate the used GAC adsorbent from the permeate (Figure 9A). The filtered sample was then stored in a cleaned 300 ml bottle with a screw top for further analysis (Figure 9B).

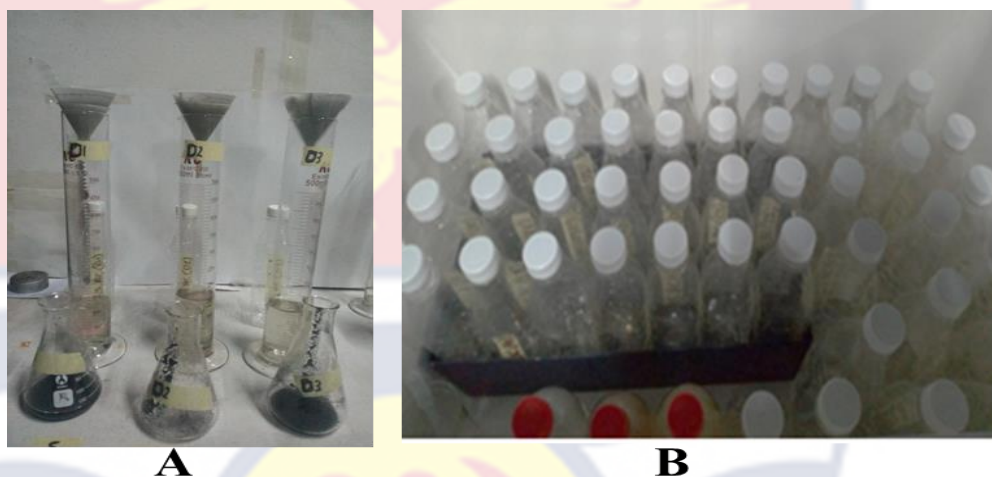


*Figure 9:* (A) Filtration of adsorbent water mixture through Whatman filter paper (150 mm  $\emptyset$ ) (B) Filtered water samples stored in bottles

Some unfiltered Brimsu water samples were filtered through a filter paper (150 mm  $\emptyset$ ) without the GAC adsorbent and labelled as BM\_FP. This sample was used as the reference unfiltered water sample to observe the effect of the adsorbent and not the filter paper on removing DOM. The label description of the adsorbent-filtered samples is shown in Table 2 for F\_CS\_CA adsorbent. This labelling system was employed for all 108 filtered samples that resulted from the beaker test (Table 3). The filtered and unfiltered water samples were each tested for physicochemical and optical water quality parameters using appropriate instruments and techniques; UV-visible absorbance and UV LED-IT spectroscopy, LIF, and polarized light microscopy with a NIR LED.

**Table 2: Filtered sample labels for F\_CS\_CA**

Sample Label	Description
F_CS_CA_B1	Filtered with 10 g of F_CS_CA with a retention of 5 minutes
F_CS_CA_D1	Filtered with 20 g of F_CS_CA with a retention of 5 minutes
F_CS_CA_F1	Filtered with 30 g of F_CS_CA with a retention of 5 minutes
F_CS_CA_B2	Filtered with 10 g of F_CS_CA with a retention of 10 minutes
F_CS_CA_D2	Filtered with 20 g of F_CS_CA with a retention of 10 minutes
F_CS_CA_F2	Filtered with 30 g of F_CS_CA with a retention of 10 minutes
F_CS_CA_B3	Filtered with 10 g of F_CS_CA with a retention of 15 minutes
F_CS_CA_D3	Filtered with 20 g of F_CS_CA with a retention of 15 minutes
F_CS_CA_F3	Filtered with 30 g of F_CS_CA with a retention of 15 minutes

Source: This study

**Table 3: Filtered sample labels for all adsorbents**

Time (min)	Mass (g)		
	10	20	30
5	F_CS_CA(B1)	F_CS_CA(D1)	F_CS_CA(F1)
	C_CS_CA(B1)	C_CS_CA(D1)	C_CS_CA(F1)
10	F_CS_CA(B2)	F_CS_CA(D2)	F_CS_CA(F2)
	C_CS_CA(B2)	C_CS_CA(D2)	C_CS_CA(F2)
15	F_CS_CA(B3)	F_CS_CA(D3)	F_CS_CA(F3)
	C_CS_CA(B3)	C_CS_CA(D3)	C_CS_CA(F3)
5	F_CS_NA(B1)	F_CS_NA(D1)	F_CS_NA(F1)
	C_CS_NA(B1)	C_CS_NA(D1)	C_CS_NA(F1)
10	F_CS_NA(B2)	F_CS_NA(D2)	F_CS_NA(F2)
	C_CS_NA(B2)	C_CS_NA(D2)	C_CS_NA(F2)
15	F_CS_NA(B3)	F_CS_NA(D3)	F_CS_NA(F3)
	C_CS_NA(B3)	C_CS_NA(D3)	C_CS_NA(F3)
5	F_CT_CA(B1)	F_CT_CA(D1)	F_CT_CA(F1)
	C_CT_CA(B1)	C_CT_CA(D1)	C_CT_CA(F1)
10	F_CT_CA(B2)	F_CT_CA(D2)	F_CT_CA(F2)
	C_CT_CA(B2)	C_CT_CA(D2)	C_CT_CA(F2)
15	F_CT_CA(B3)	F_CT_CA(D3)	F_CT_CA(F3)
	C_CT_CA(B3)	C_CT_CA(D3)	C_CT_CA(F3)
5	F_CT_NA(B1)	F_CT_NA(D1)	F_CT_NA(F1)
	C_CT_NA(B1)	C_CT_NA(D1)	C_CT_NA(F1)
10	F_CT_NA(B2)	F_CT_NA(D2)	F_CT_NA(F2)
	C_CT_NA(B2)	C_CT_NA(D2)	C_CT_NA(F2)
15	F_CT_NA(B3)	F_CT_NA(D3)	F_CT_NA(F3)
	C_CT_NA(B3)	C_CT_NA(D3)	C_CT_NA(F3)
5	F_ST_CA(B1)	F_ST_CA(D1)	F_ST_CA(F1)
	C_ST_CA(B1)	C_ST_CA(D1)	C_ST_CA(F1)
10	F_ST_CA(B2)	F_ST_CA(D2)	F_ST_CA(F2)
	C_ST_CA(B2)	C_ST_CA(D2)	C_ST_CA(F2)
15	F_ST_CA(B3)	F_ST_CA(D3)	F_ST_CA(F3)
	C_ST_CA(B3)	C_ST_CA(D3)	C_ST_CA(F3)
5	F_ST_NA(B1)	F_ST_NA(D1)	F_ST_NA(F1)
	C_ST_NA(B1)	C_ST_NA(D1)	C_ST_NA(F1)
10	F_ST_NA(B2)	F_ST_NA(D2)	F_ST_NA(F2)
	C_ST_NA(B2)	C_ST_NA(D2)	C_ST_NA(F2)
15	F_ST_NA(B3)	F_ST_NA(D3)	F_ST_NA(F3)
	C_ST_NA(B3)	C_ST_NA(D3)	C_ST_NA(F3)

Source: This study



### Physicochemical water quality assessment

Some physicochemical water quality parameters, such as pH and salinity, can easily be affected by the salts (NaCl and CaCl<sub>2</sub>) used in the activation process. Hence, the pH and salinity of each filtered and unfiltered water sample were determined using an Eutech benchtop multiparameter analyser (PC 700, USA), and the Trace20 HT100 (USA), respectively. Each parameter was measured thrice and the average was recorded (See Appendix B).

### UV-visible absorbance spectroscopy

The absorbance of each sample in the UV and visible region was determined for each filtered and unfiltered water sample at room temperature (26 °C) using a double beam spectrophotometer (VWR UV 6300PC, USA) as shown in Figure 10. The spectrophotometer uses a tungsten/deuterium lamp with a wavelength range of 190 nm to 1100 nm, a scanning speed of 100 to 3000 nm/min interval, and an absorbance range and accuracy of -0.3 to 3 and  $\pm 0.002$ , respectively.

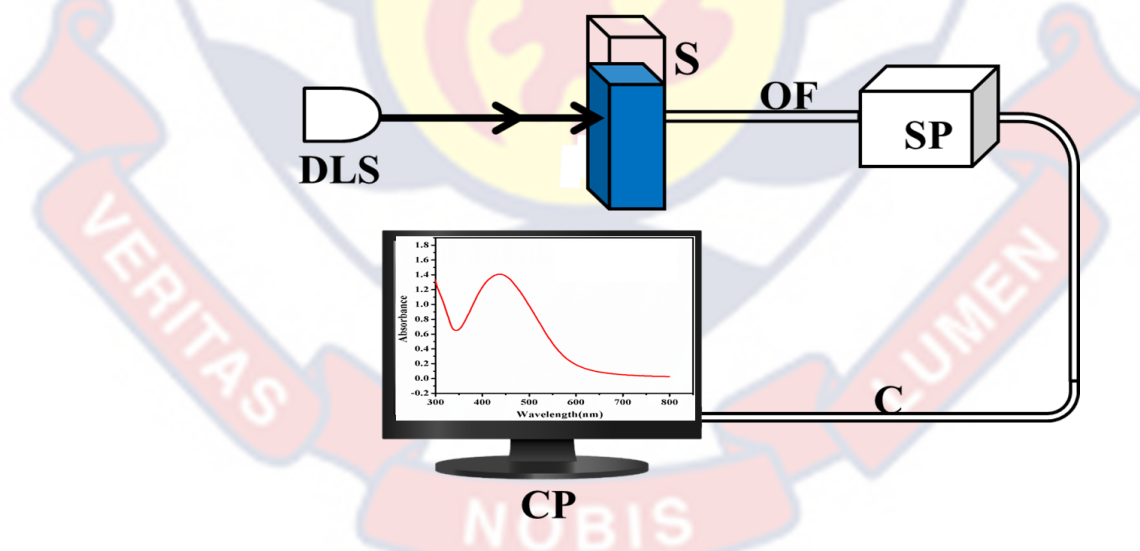


Figure 10: The double-beam spectrophotometer (VWR 6300PC, USA)

Two quartz cuvettes with two transparent and two translucent sides were rinsed with distilled water and air-dried. One cuvette was filled with distilled water and placed in the reference sample holder, whilst the other cuvette was filled with the sample to be analysed and placed in the analyte sample holder. After each analysis, the analyte sample cuvette was filled with the sample that followed, one after the other.

Absorbance scans were performed for each sample in duplicates at a wavelength range of 200 nm to 1000 nm in an interval of 2 nm. The absorbance spectral data for each sample was recorded and later plotted in Matlab2020a. The absorbance at 254 nm ( $A_{254}$ ) was determined for each sample in duplicates, and the averaged values were recorded.

The absorbance spectrum for each sample was again determined using an Oceanview-controlled set-up with a deuterium lamp source, a CUV cuvette holder, and a USB4000 spectrometer detecting system as shown in Figure 11.



*Figure 11:* Schematic Diagram of Absorbance Setup. DLS is the deuterium light source, S is the sample holder, OF is the optical fibre, SP is the spectrometer (USB 4000, Ocean Optics, USA), C is the cable, and CP is the computer.



The electromagnetic radiation from the deuterium lamp source was incident on each sample placed in the sample holder. The spectrometer detected the absorbance spectra for each corresponding sample and the absorbance data stored for each filtered and unfiltered water sample. The stored data were later normalized with the absorbance of distilled water and plotted using Matlab2020a.

### UV-LED induced transmission

The transmittance spectra of the filtered and unfiltered water samples were determined using an LED-induced transmission (LED-IT) setup, as shown in Figure 12. A UV LED source, typically emitting at 255 nm with an optical output power of 0.3 mW (UVTOP250-HL-TO39, Roithner LaserTechnik, Austria), was used as the excitation source in the setup.

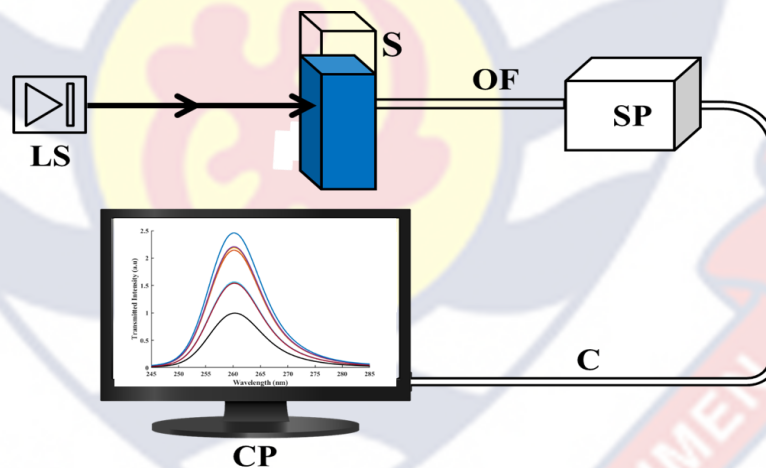


*Figure 12:* Schematic diagram of LED-IT setup. LS is the UV light emitting diode source, S is the sample, OF is the optical fibre, SP is the spectrometer (USB 4000, Ocean Optics, USA), C is the cable, and CP is the computer.

Each sample was poured into a quartz cuvette and placed in a CUV cuvette holder, with a spectrometer (USB4000, Ocean Optics, USA) as the detecting system connected to a desktop computer (Hp, Intel (R) Core (TM) i3

8<sup>th</sup> generation) (Figure 12). The spectrum of the transmitted light was recorded for each filtered and unfiltered water sample.

### Laser-induced fluorescence

The DOM fluorescence spectra of the filtered and unfiltered water samples were determined using the laser-induced fluorescence (LIF) setup as shown in Figure 13.

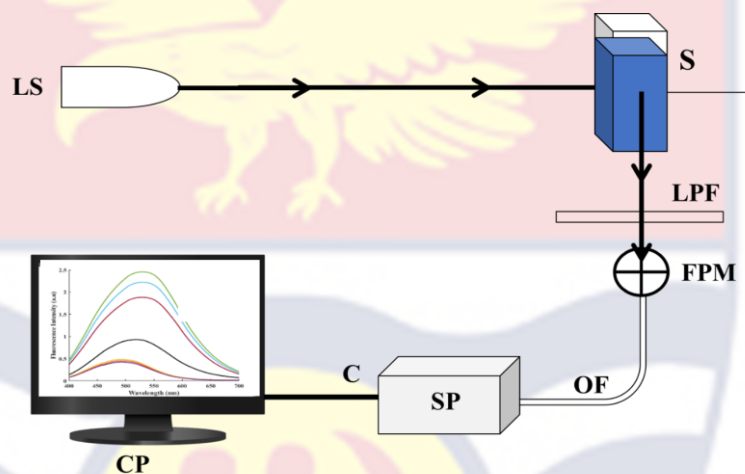


*Figure 13:* Schematic Diagram of LIF Setup. LS is the laser source, S is the sample, OF is the optical fibre, SP is the spectrometer (USB 4000, LPF is the long pass filter, FPM is the fibre port-micro positioner, C is the cable, and CP is the computer.

This LIF setup, just like any fluorescence setup, consists of three major components: the light source, the detecting system, and some other optical elements (Figure 13). A diode laser (Laser module, China) with an excitation wavelength of 405 nm was used in the LIF setup, with two optical fibres (P50-1-UV-VIS, Ocean Optics, USA), a long pass filter with cut-off at 425 nm (425FCS2500, Knight Optical, UK), and a CUV cuvette holder (CUV-ALL-UV, Ocean Optics, USA). A quartz cuvette (104F-QS, Hellma Analytics, Germany) was used as a sample cell, with a spectrometer (USB4000, Ocean

Optics, USA) as the detecting system connected to a desktop computer (Hp, Intel (R) Core (TM) i3 8<sup>th</sup> generation).

Each sample was excited using the 405 nm laser light source and guided onto the sample through the optical fibre with a core diameter of 600  $\mu\text{m}$ . The other optical fibre, positioned 90<sup>0</sup> to the incident beam, was connected from the long-pass filter to the spectrometer. The fluorescence emission spectrum of each sample was collected without the excitation wavelength and displayed on the computer. The Oceanview software was used to control the detecting system and save the fluorescence emission spectra of the samples.

### **Polarized light microscopy**

A transmission-based polarization imaging system was built using LEGO (LEGO TECHNIC 42055, LEGO<sup>®</sup>, USA), with a NIR LED light source of 815 nm. A Raspberry pi embedded with a Complementary Metal Oxide Semiconductor (CMOS) pi camera was programmed to control the motorized setup and take sample images at different polarization angles. The angles used for this study were 0, 15, 30, 45, 60, 75, 90, 105, 120, 135, 150, 165, and 180 degrees. This LEGO-based motorized system (Figure 14) was equipped with three main motors, labelled A, B, and C, which are responsible for controlling the light source (LS), the sample stage, and the polarizer (P), respectively.

However, for this study, only the polarization angles were varied, with the sample stage and light source directly in line with the pi camera (PC) detector. The NIR LED light source was polarized and focused directly onto the sample with a converging lens (L). The polarizer after the sample was then rotated with the help of motor C (Figure 14) at different angles from 0<sup>0</sup> to 180<sup>0</sup>,

inclusive with an interval of  $15^{\circ}$ . An image of the polarized light transmitted through the sample was captured by the PC for each polarization angle.

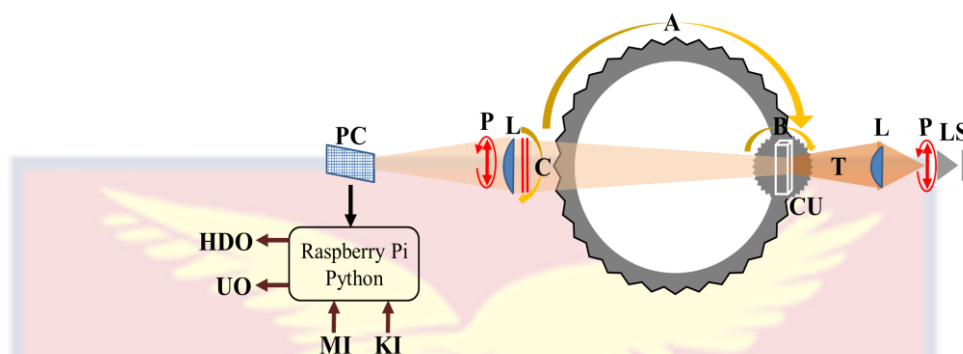


*Figure 14:* Schematic Diagram of transmission-based LEGO polarization imaging setup. LS is the light source (NIR-LED), P is the polarizer, L is the lens, T is the transmitted ray, CU is the cuvette, A, B, and C are the motors for controlling the light source, sample stage, and polarizer, PC is the Pi camera, HDO is the HDMI outlet, UC is the USB outlet, MI is the mouse inlet, and KI is the keyboard inlet

This process was repeated for all filtered and unfiltered water samples, giving a total of 1404 images, with 13 images per sample. A well-labelled plate of the setup is shown in Figure 15.

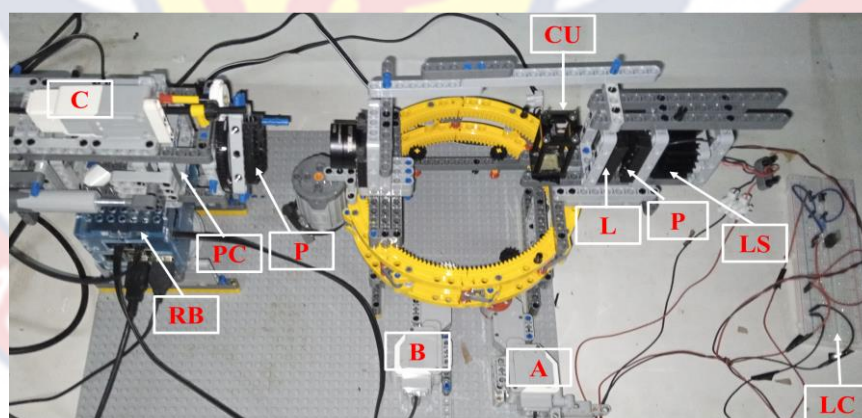


*Figure 15:* A picture of the transmission-based LEGO Polarization Imaging Set-up. LS is the light source (NIR-LED), LC is the light source power circuit, P is the polarizer, L is the lens, CU is the cuvette, A, B, and C are the motors for controlling the light source, sample stage, and polarizer, respectively, PC is the Pi camera, and RB is the Raspberry Pi



This transmission-based polarization imaging system made from LEGOs and a few optical components is at the moment the first of its kind in the field of polarization imaging for water quality analysis.

### **Data Analysis (Principal Component and Cluster Analysis)**

To better determine the most efficient adsorbent from the twelve (12) prepared AC adsorbents, an unsupervised pattern recognition method was used to establish the structure in the various data sets obtained from the spectroscopic techniques. Some unsupervised algorithms used in this study included clustering and dimensional reduction. Due to the dependence of these multivariate techniques on distance, each data set was normalized before applying the algorithms.

Principal Component Analysis (PCA) and Cluster Analysis (CA) were specially employed among the various clustering and dimensional reduction methods for the different spectroscopic data sets. The algorithms for PCA and CA were developed and used in Matlab 2020a to transform the spectral dataset for the various filtered and unfiltered water samples into principal components (PCs) and clusters, respectively, without altering the spectral information. These multivariate techniques also helped detect outliers in the spectral data set, thus giving an accurate discriminatory analysis of the samples (Amuah, 2020; Raja, 2020).

### **COMSOL Multiphysics Simulation of a Filter**

In this study, the free and porous media interface was coupled with the transport of diluted species in the porous media interface of COMSOL 5.6. This coupled study was used to simulate the velocity profile and, the transportation and adsorption of water contaminants in a designed composite membrane filter.



Transport of diluted species in the porous media interface was used to determine the change in the concentration of contaminants as adsorption takes place with time. This information helped ascertain the number of treatments trips a particular adsorbent can use to maintain a decent contaminant removal efficiency. A 3-dimensional geometrical model of the filter design is shown in Figure 16.

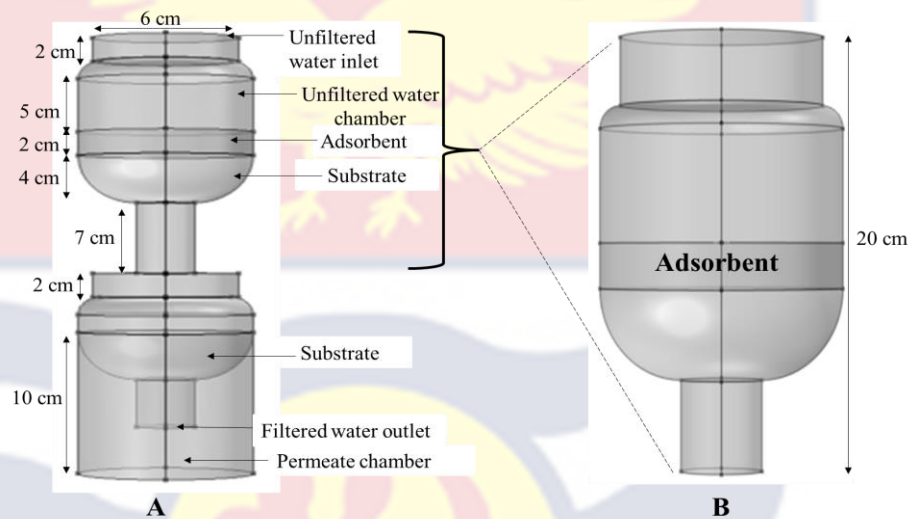
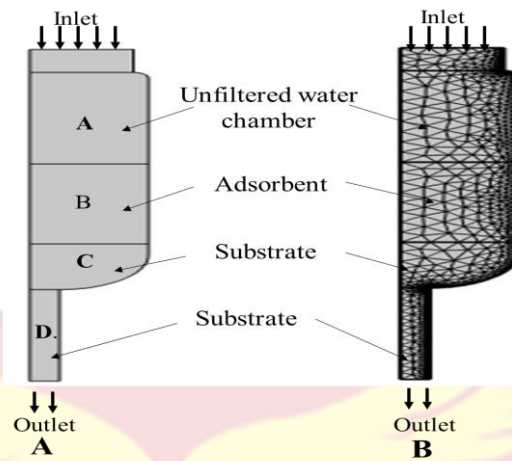


Figure 16: (A) 3-dimensional visualisation of a designed filter model in COMSOL 5.6 (B) Extrusion of treatment chamber containing the adsorbent

A 2D axisymmetric geometry was used for the coupled multiphysics simulation, as shown in Figure 17. This geometry speeds up the computation process and gives post-processing results in 3D. The simulation was carried out under stationary- and time-dependent conditions for the fluid flow and species transport, respectively. A height of 7 cm and an internal diameter of 7 cm were used as the dimensions of the cylindrical treatment chamber. The contaminant concentration of the water was specified as the raw water inlet. This contaminated raw water was simulated to flow through the selected adsorbent column which constitutes the activated carbon and substrate (PUF), with an average inlet velocity of 0.1 m/s.



*Figure 17: (A) Filter model geometry and (B) meshed geometry used to simulate the velocity profile and transport of water contaminants in the designed filter*

The adsorbent density was calculated using adsorbent mass and filter column volume. The 0.5 (1) substrate porosity used in this study was adapted from Yunus et al., (2019). The flow regime was incompressible due to the constant density of the selected liquid material (water) and laminar with no-slip boundary conditions. Atmospheric pressure conditions were assumed at the inlet and outlet, and a user-defined mesh size was selected.

### Chapter Summary

The chapter described the adsorbent preparation and characterisation methods (XRD and FTIR), sample collection site, adsorbent testing, and sample analysis techniques. The chapter also elaborated on other spectroscopic methods, UV-visible absorbance, LED-IT, LIF, and NIR polarized light microscopy, used in characterising the DOM in the filtered and unfiltered samples. This chapter also encompassed the selected multivariate techniques used with the acquired data sets in discriminating between the water samples regarding DOM concentration.

## CHAPTER FOUR

### RESULTS AND DISCUSSION

#### Introduction

This chapter presents the results and discussion of the approaches (Chapter 3) used in the present study. The first part covers the characteristics of the granular activated carbon (GAC) adsorbents obtained from the various characterisation techniques. The second part elucidates the results from the four spectroscopic techniques: UV-visible absorbance, UV LED-induced transmittance, Laser-Induced Fluorescence (LIF), and NIR-LED polarized light microscopy, used in testing the prepared granular activated carbon (GAC) adsorbents are discussed. In the third part, a detailed discussion of the postprocessing results from the COMSOL Multiphysics simulation was given.

#### Adsorbent Characterisation

##### X-ray diffraction spectroscopy

The XRD spectra for the twelve prepared granular activated carbon (GAC) adsorbents are shown in Figures 18, 19, and 20, respectively. In all, two prominent broad diffraction peaks could be identified in the XRD spectra at  $2\theta$  ( $2\theta$ ) ranges of;  $19^\circ \leq 2\theta \leq 35^\circ$  and  $35^\circ \leq 2\theta \leq 55^\circ$  in the current study. These broad peaks are usually observed in the XRD spectra of most activated carbon samples. The two broad peaks indicate the amorphous nature of the GAC adsorbents used. Studies have shown that the two broad peaks indicate the presence of carbon and graphite (Bakti & Gareso, 2018; Mopoung, Moonsri, Palas, & Khumpai, 2015; Shukla et al., 2020; Tahir, Liong, & Bakri, 2016).

The accompanying narrow peaks shown in Figures 18, 19, and 20 exhibit the crystallinity of the GAC adsorbents used in this study. According to

Tahir et al. (2016), this observation is influenced by peak intensity. The observed prominent narrow peaks of the GAC sample were in a range of  $29.3^{\circ} \leq 2\theta \leq 39.5^{\circ}$ , which correspond to silicate minerals, iron ore, and quartz, respectively. The narrow peaks observed in the cassia tree (CT) branch and shea nut tree (ST) branch GAC samples are fascinating. These indicate higher crystallinity and larger pore surface area (Bakti & Gareso, 2018; Mopoung et al., 2015; Tahir et al., 2016).

For the coconut shell (CS) GAC samples (Figure 18), only F\_CS\_CA and C\_CS\_CA showed some crystallinity, yet C\_CS\_CA has pronounced crystallinity shown at  $2\theta \cong 32^{\circ}$ . Furthermore, there seems to be a slight shift to the right of the broad and some narrow diffraction peaks after chemical activation, showing the theoretical changes in the atomic distance of activated carbon, which may be caused by a shift in the interlayer spacing (Farma et al., 2018; Bakti & Gareso, 2018; Tahir et al., 2016).

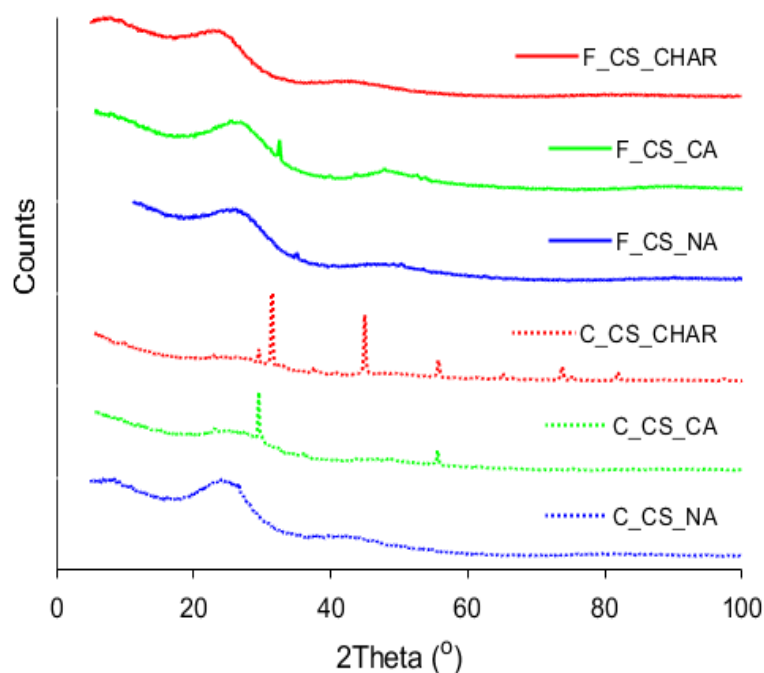


Figure 18: X-ray diffraction spectra for furnace and conventionally carbonized coconut shell (CS) activated carbon samples.



This slight shift of the broad and narrow diffraction peaks was mainly observed in the furnace carbonized GAC adsorbents (Figures 18, 19, and 20, respectively). Other narrow peaks observed at two theta ( $2\theta$ ) values of  $44.5^\circ$  to  $45.0^\circ$ , mostly obtained in the shea nut and cassia siamea tree-activated adsorbents (Figures 19 and 20). They, also correspond to sodalite, analcime and sodium silicate. A narrow peak at  $33^\circ$  was observed for all the NaCl-activated adsorbents, indicating the presence of Na, which is prominent in sample C\_CT\_NA (Figure 19) (Farma et al., 2018; Bakti & Gareso, 2018; Tahir et al., 2016).

All the shea nut tree (ST) branch GAC samples showed more crystallinity due to the presence of several narrow peaks from  $29.3^\circ$  to  $60.81^\circ$  (Dungani et al., 2022), with low intensities in the amorphous signature regions (Figure 20).

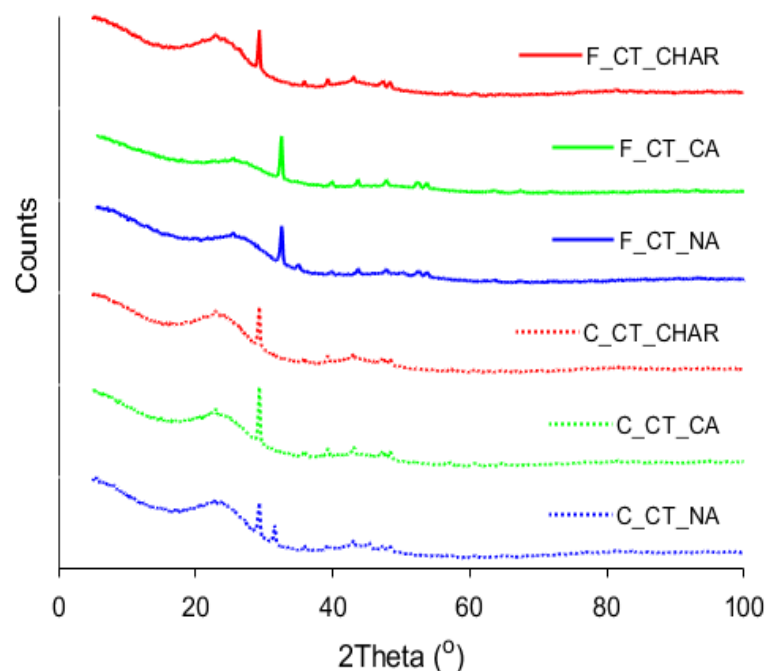
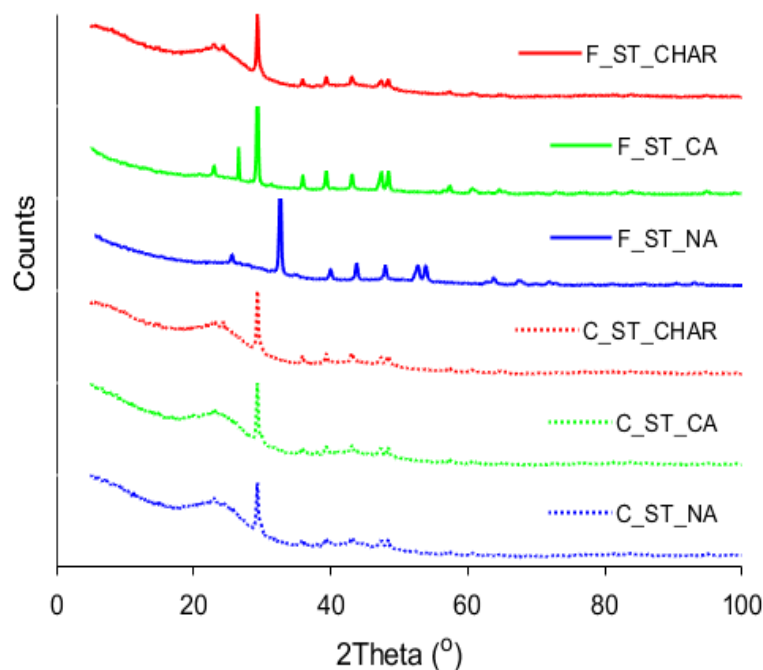


Figure 19: X-ray diffraction spectra for furnace and conventionally carbonized cassia siamea tree (CT) branch-activated adsorbents.

These narrow peaks were generally low in intensity for the conventionally carbonized shea nut tree (ST) adsorbents. They may indicate a much smaller full-width half maximum (FWHM) (From the XRD data obtained) and hence higher crystalline sizes (Bakti & Gareso, 2018).



*Figure 20: X-ray diffraction spectra for furnace and conventionally carbonized shea nut tree (ST) activated carbon samples.*

The crystallite sizes of the prepared GAC adsorbents were estimated using the Debye-Scherrer equation (equation 4) at the two central  $2\theta$  angles,  $39.4^\circ$  and  $48.4^\circ$ , as shown in Table 4. These selected angles are the highest  $2\theta$  angles at which peaks occur for most GAC samples (All except F\_CS). Moreover, as the crystallite size of the sample increases, only peaks at higher  $2\theta$  angles are expected to give better results (Muniz, Santos, Miranda, & Universidade, 2016).

The estimated crystallite sizes of the various prepared GAC adsorbents ranged from 20.85 nm to 27.66 nm, corresponding to C\_CT\_NA, C\_CT\_CA

and F\_ST\_NA, respectively. The adsorbents with the highest crystallite sizes, C\_CT\_CA and F\_ST\_NA, were also observed to have higher peak intensities and, hence, shorter FWHM for the sharp narrow peaks (Figures 19 and 20). This observation is due to the inverse relationship between the crystallite size and FWHM, as in equation (4). The opposite of this observation was seen in C\_CT\_CA, which showcased the smallest crystallite size.

**Table 4: Crystallite sizes of the prepared adsorbents**

Adsorbent Label	$2\theta = 39.4$	$2\theta = 48.4$	Mean Crystallite Size (nm)
F_CS_CA	0.00	0.00	0.00
F_CS_NA	0.00	0.00	0.00
C_CS_CA	0.00	0.00	0.00
C_CS_NA	0.00	0.00	0.00
F_CT_CA	27.22	28.10	27.66
F_CT_NA	27.22	21.07	24.15
C_CT_CA	27.22	28.10	27.66
C_CT_NA	13.61	28.10	20.85
F_ST_CA	27.22	21.24	24.23
F_ST_NA	27.22	28.10	27.66
C_ST_CA	20.58	28.10	24.34
C_ST_NA	27.22	0.31	27.66

Source: This study

The estimated crystallite sizes may also indicate a difference in their DOM removal efficiencies as determined by the selected spectroscopic techniques. However, these estimated crystallite sizes may not reflect an actual dependence on the adsorbent efficiency due to the instrument's contribution to the FWHM values and several other defects (Speakman, 2022). The zero (0) crystallite sizes observed for mostly the coconut shell (CS) based GAC were also due to the absence of peaks at the selected  $2\theta$  angles.

Moreover, the use of the Scherrer equation in determining the crystallite sizes of locally prepared GAC samples (particle size  $\leq 0.5$  mm) in this study is the first of its kind. Applying the Scherrer equation to large crystallite sizes is not yet precise since its derivation is based on the kinematical theory of X-ray diffraction (Muniz et al., 2016).

### Fourier transform infrared spectroscopy

The FTIR spectra, which shows the functional groups present in the prepared GAC adsorbents, are shown in Figures 21 to 23. The mixture of broad and narrow transmission bands shows the rich chemical nature of the prepared adsorbents, especially in terms of carbon. The broadband occurring at 3200 to 3800  $\text{cm}^{-1}$  for some adsorbents is attributed to the O–H stretching of hydroxyl groups and the type of hydrogen bonding present in the adsorbents (Dungani et al., 2022). The broadening at 3200 – 3800  $\text{cm}^{-1}$  may also indicate the presence of some N–H stretching of amines ( $\text{NH}_2$ ) and several carbon bonds.

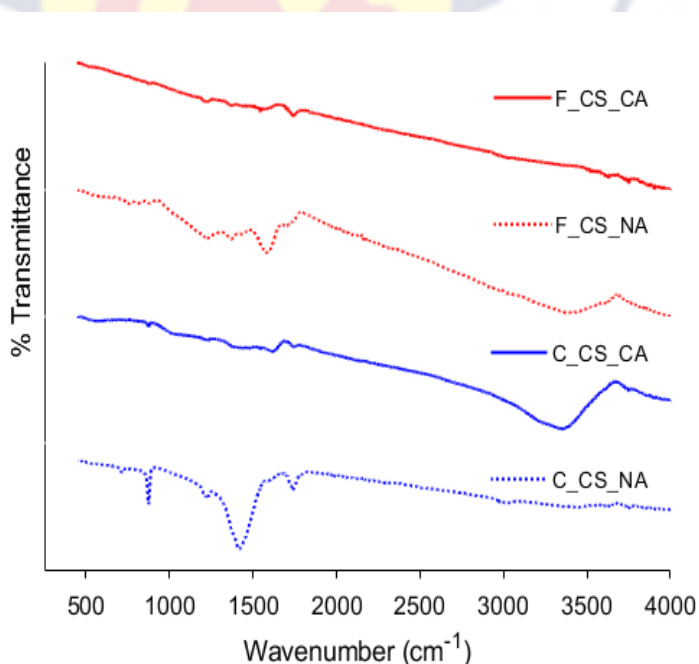


Figure 21: Fourier transform infrared (FTIR) spectra from the coconut shell activated carbon adsorbents



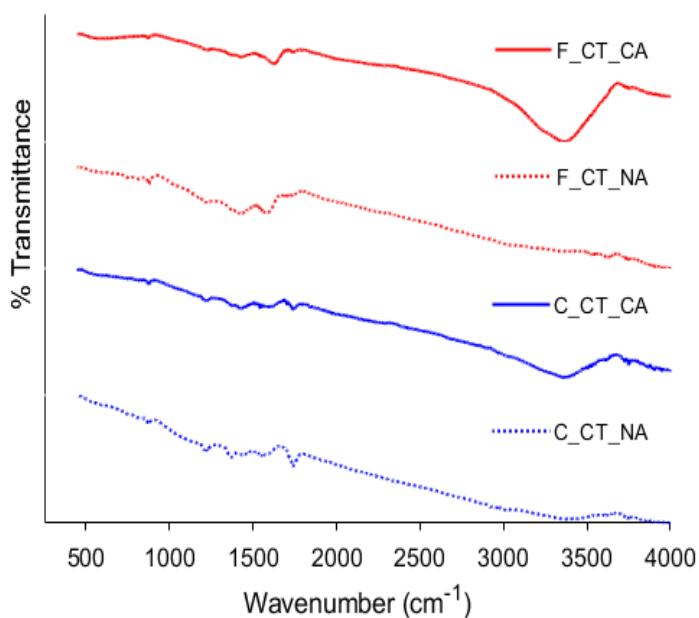


Figure 22: Fourier transform infra-red (FTIR) spectra for cassia siamea tree branch activated carbon adsorbents

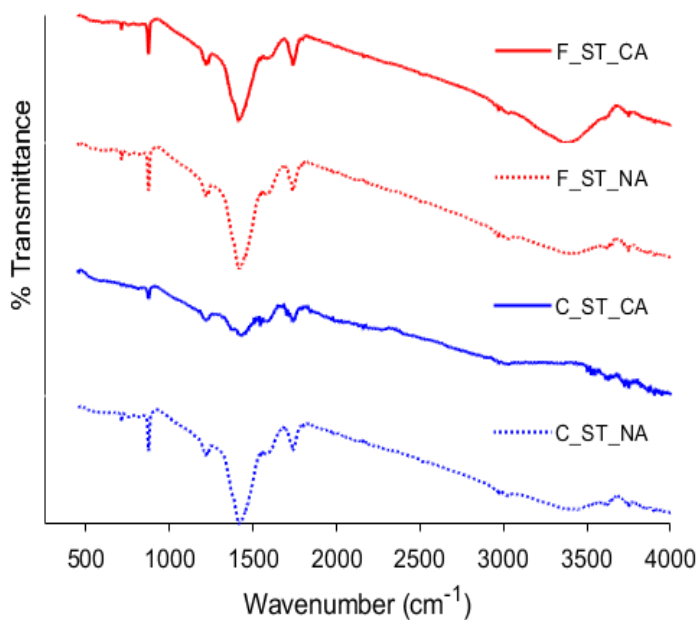


Figure 23: Fourier transform infra-red (FTIR) spectra for shea nut tree branch activated carbon adsorbents

The decrease in the percentage transmittance at this broadband (3200 – 3800  $\text{cm}^{-1}$ ) can be attributed to removing hydrogen and oxygen atoms during the  $\text{CaCl}_2$  activation process (Ali, Aslam, Shawabkeh, Asghar, & Hussein,

2020; Bakti & Gareso, 2018). Moreover, the vibration mode of  $\text{-OH}$  ( $3200 - 3800 \text{ cm}^{-1}$ ) was also observed to be lower for C\_CS\_CA, F\_ST\_CA, and F\_CT\_CA as compared to their NaCl-activated counterparts (Arneli et al., 2017).

This peak is also a well-known feature of most GAC FTIR spectra (Arneli et al., 2017; Dungani et al., 2022) and is very pronounced in the  $\text{CaCl}_2$ -activated adsorbents, especially in F\_CT\_CA (Figure 22). A carbonyl group ( $\text{C=O}$ ) at  $1700 - 1740 \text{ cm}^{-1}$  was also observed in all GAC adsorbents but appeared to be very pronounced in the shea nut tree (ST) GAC adsorbent spectra (Figure 23). This peak is, however, virtually non-existent in the CS and CT adsorbents due to the volatile nature of most carbonyl groups (Bakti & Gareso, 2018).

The pronounced transmission peak around  $1400 \text{ cm}^{-1}$  for C\_CS\_NA and all ST GAC adsorbents (Figure 21 to 23) may be ascribed to some in-plane vibration of carboxylic groups or some oxygen-containing functional groups, such as;  $\text{C-O}$  and  $\text{C=O}$  stretching (Mopoung et al., 2015). The other weak transmission signals at  $1000 - 1300 \text{ cm}^{-1}$ , common in the FTIR spectra of oxidized carbon, show a  $\text{C-O}$  stretching made up of several functional groups; esters, phenols, alcohols, and acids (Ali et al., 2020). The narrow bands around  $800 - 900 \text{ cm}^{-1}$  in the ST GAC adsorbent spectra also confirm the presence of silica-containing minerals due to  $\text{Si-H}$  stretching vibrations, as expected in most AC samples (Amuah, 2020; Mopoung et al., 2015).

### Physicochemical Results

The pH of the unfiltered water sample (Bm\_FP) was 7.00, whilst that of the filtered water samples ranged from 6.71 to 8.84 (Appendix B). The decrease

in the pH of some filtered samples, especially those filtered with the conventionally carbonized and NaCl-activated adsorbents, may be due to using a simple salt in the activation process. However, this decrease in pH is very small since the species formed from the reaction between water and NaCl (OH<sup>-</sup> and H<sup>+</sup>) balance each other (Ahmad, 2013). But generally, these results indicate that the pH of the filtered water samples is within the WHO standard (6.5 – 8.5) (World Health Organization, 2017).

The salinity of all filtered water samples also ranged from 0.04 parts per trillion (ppt) to 2.3 ppt (APPENDIX B). The salinity values recorded for all the filtered samples are far less than the recommended limit of  $5 \times 10^8$  ppt (World Health Organization, 2017). These low salinity levels indicate that the salts (CaCl<sub>2</sub> and NaCl) used in the activation processes were rinsed out properly, thus, leaving no traces of salts in the prepared GAC adsorbents.

### **Absorbance and Transmittance Spectrophotometer**

#### **Absorbance with VWR 6300PC spectrophotometer**

The absorbance spectra acquired for all filtered and unfiltered water samples using the VWR 6300PC spectrophotometer are shown in Figure 24. These spectra are, however, featureless (Figure 24), with very little or no discrimination between the filtered and unfiltered samples. Therefore, this lack of specific features in the UV-visible absorbance spectra for water samples has led to identifying some fingerprint wavelengths with a good representation of the different characteristics of DOM in water samples (Bolton, 2003; Carstea et al., 2020). In Table 5, some of the commonly used fingerprint wavelengths are shown.

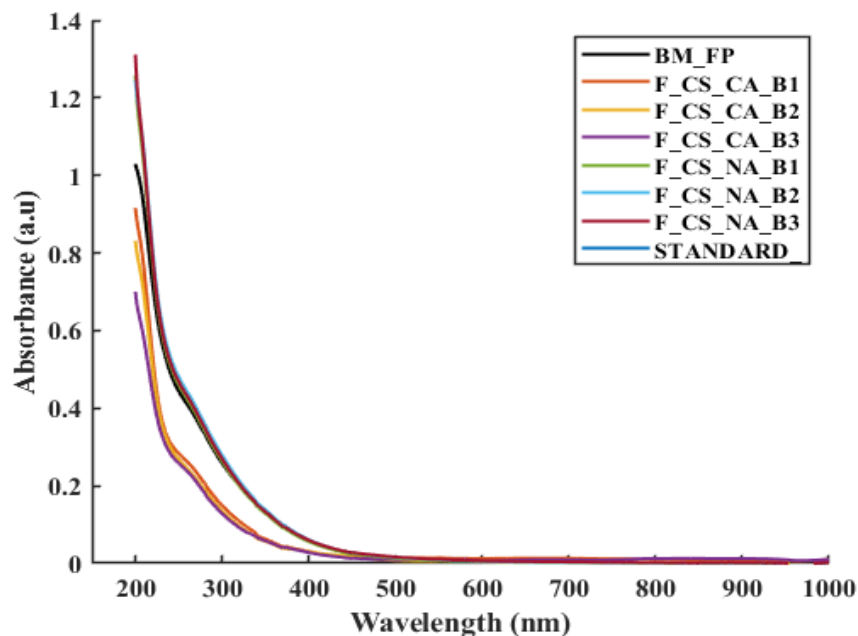


Figure 24: Absorbance spectra for samples filtered with 10 g of furnace carbonized coconut shell-activated carbon

Table 5: Fingerprint Wavelengths for DOM Absorbance

Wavelength (nm)	Properties	Reference
250 nm/365 nm	Aromaticity and molecular	Peuravouri and Pihlaja
203 nm/253 nm	Functionality	Korshin et al. (1997)
254 nm/436 nm		Gjessing et al. (1998);
270 nm/350 nm	Aromaticity (Humification)	Trubetskoj et al. (1999)
465 nm/665 nm		Chen et al. (2002)
272 nm and 280 nm	Aromaticity and molecular weight	Triana et al. (1990); Chin et al. (1994);
254 nm and 272 nm	DBPs Formation	Banks and Wilson (2002); Korshin et al. (2002)
260 nm and 280 nm	Hydrophobic and aromatic	Dilling and Kaiser (2002)
254 nm/400 nm	Aromaticity and humification	Abbt-Braun and Frimmel (1999);
254 nm/365 nm	Molecular weight	Anderson et al. (2000); Anderson and Gjessing

Source: Bolton (2003)

Absorbance at 254 nm ( $A_{254}$ ) was employed in this study due to its significant correlation with DOM concentration in water. A greater portion of DOM is aromatic and constitutes the humic component (Khan et al., 2014;

Moona, 2021; Yunus, 2020). Since the humic feature of DOM is the main contributing factor to the formation of DBPs, its significant removal will result in lower DBPs formation rates.

Moreover, due to the correlation between the humic and aromatic parts of DOM, most researchers almost always use absorbance as an aromaticity monitoring technique. Therefore, a reduction in  $A_{254}$  can be attributed to the adsorption of DOM by the GAC adsorbents, thus, showcasing the adsorption capacity of such adsorbents (Moona, 2021).

The line and bar plots of absorbance at 254 nm ( $A_{254}$ ) for the filtered and unfiltered water samples are shown in Figures 25 to 30. All water samples filtered with the  $\text{CaCl}_2$ -activated GAC adsorbents showed a generally low absorbance at 254 nm ( $A_{254}$ ), thus exhibiting a higher removal efficiency. A few of the water samples filtered with NaCl-activated GAC adsorbents (F\_CS\_NA and C\_CS\_NA) showed an increase in  $A_{254}$  instead (Figure 25 to 30). This anomaly may be attributed to the addition of colour by the GAC adsorbents due to the activating chemical used in the preparation process (Moona, 2021).

For samples filtered with 10 g of each GAC adsorbent (Figures 25 and 26), C\_CS\_CA gave the highest  $A_{254}$  removal efficiency of 76% minimum and 81% maximum. The performance of C\_CS\_CA was followed closely by F\_ST\_CA with a removal efficiency of 74% minimum and 77% maximum, then C\_CT\_CA with 71% minimum and 74% maximum, C\_ST\_CA with 71% minimum and 73% maximum, F\_CT\_CA with 69% minimum and 71% maximum, and lastly F\_CS\_CA with 45% minimum and 50% maximum.



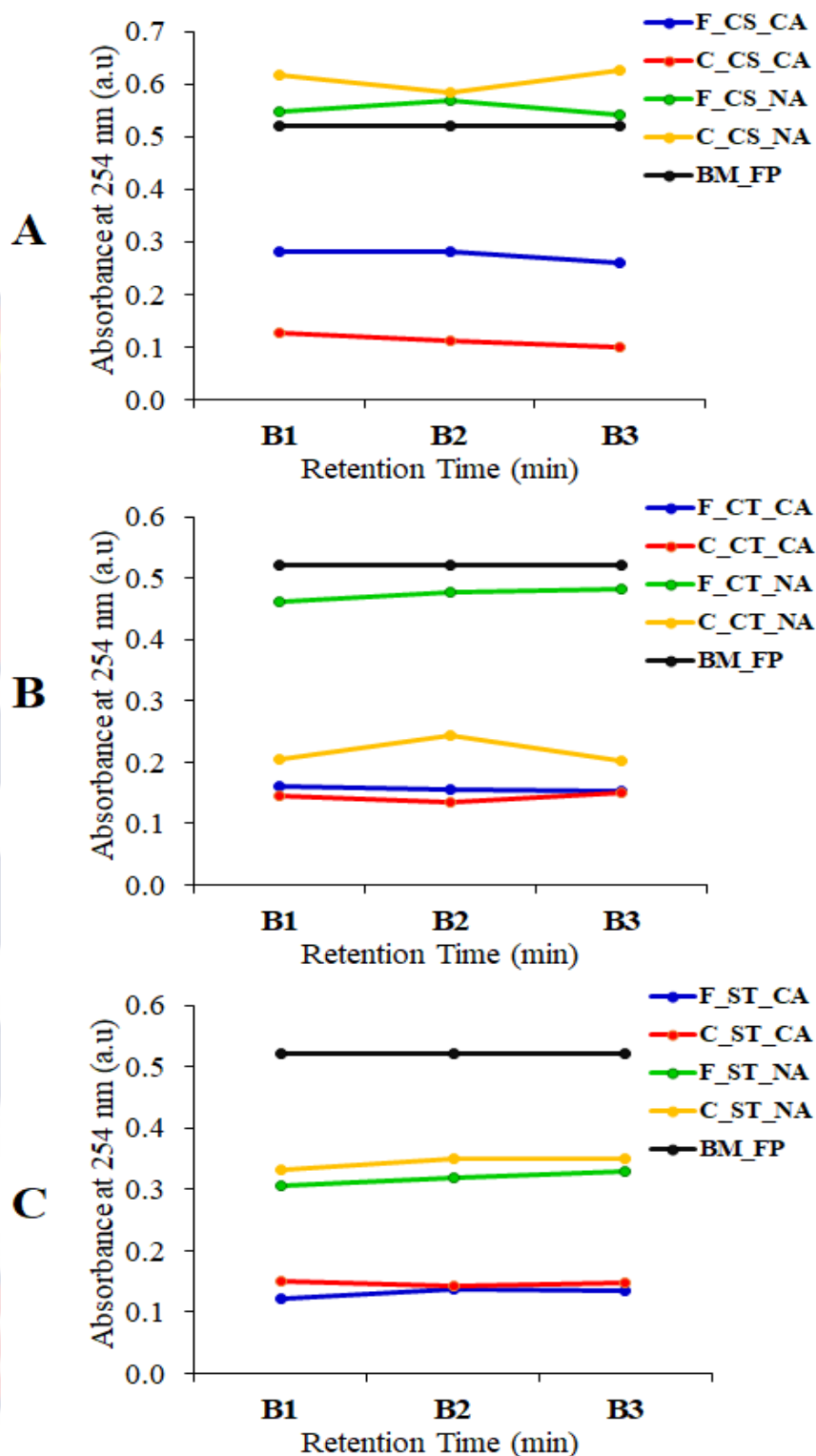
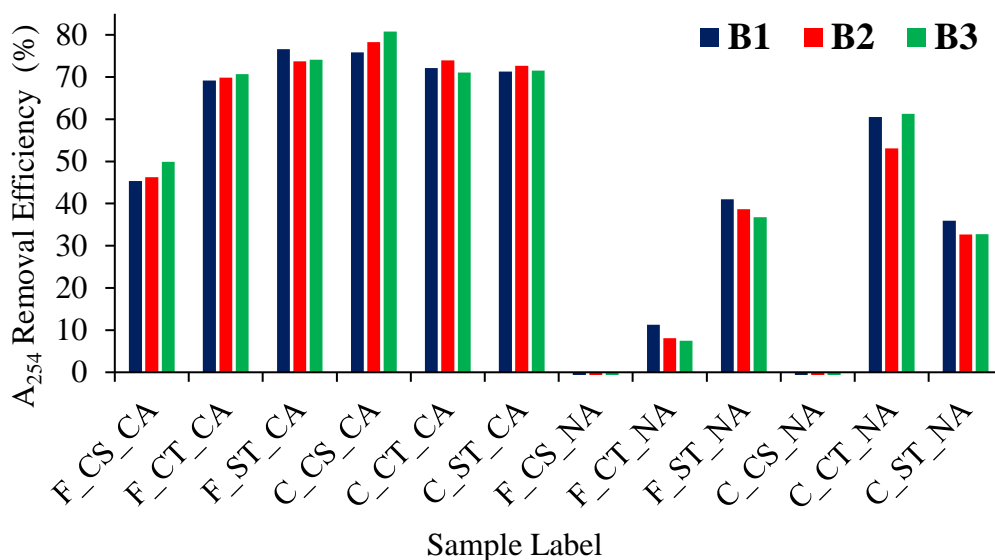


Figure 25: Absorbance at 254 nm for water samples filtered with 10 g of the furnace and conventionally carbonized (A) coconut shell, (B) cassia siamea tree branch, and (C) shea nut tree branch activated carbon adsorbents at 5(B1), 10(B2), and 15(B3) minutes retention times



*Figure 26:* Absorbance removal efficiency for samples filtered with 10 g of the furnace and conventionally carbonized coconut shell (CS), cassia siamea tree (CT) branch, and shea nut tree (ST) branch activated carbon adsorbents at 5(B1), 10(B2), and 15(B3) minutes retention times

A generally high absorbance removal efficiency was also observed for water samples filtered with 20 g of all CaCl<sub>2</sub> GAC adsorbents (Figure 27). C\_CT\_CA gave the highest A<sub>254</sub> removal efficiency of 82% minimum and 85% maximum. This performance was followed closely by F\_ST\_CA with a removal efficiency of 79% minimum and 80% maximum, then C\_ST\_CA with 75% minimum and 79% maximum, C\_CS\_CA with 76% minimum and 77% maximum, F\_CT\_CA with 74% minimum and 76% maximum, and lastly F\_CS\_CA with 58% minimum and 64% maximum (Figure 28).

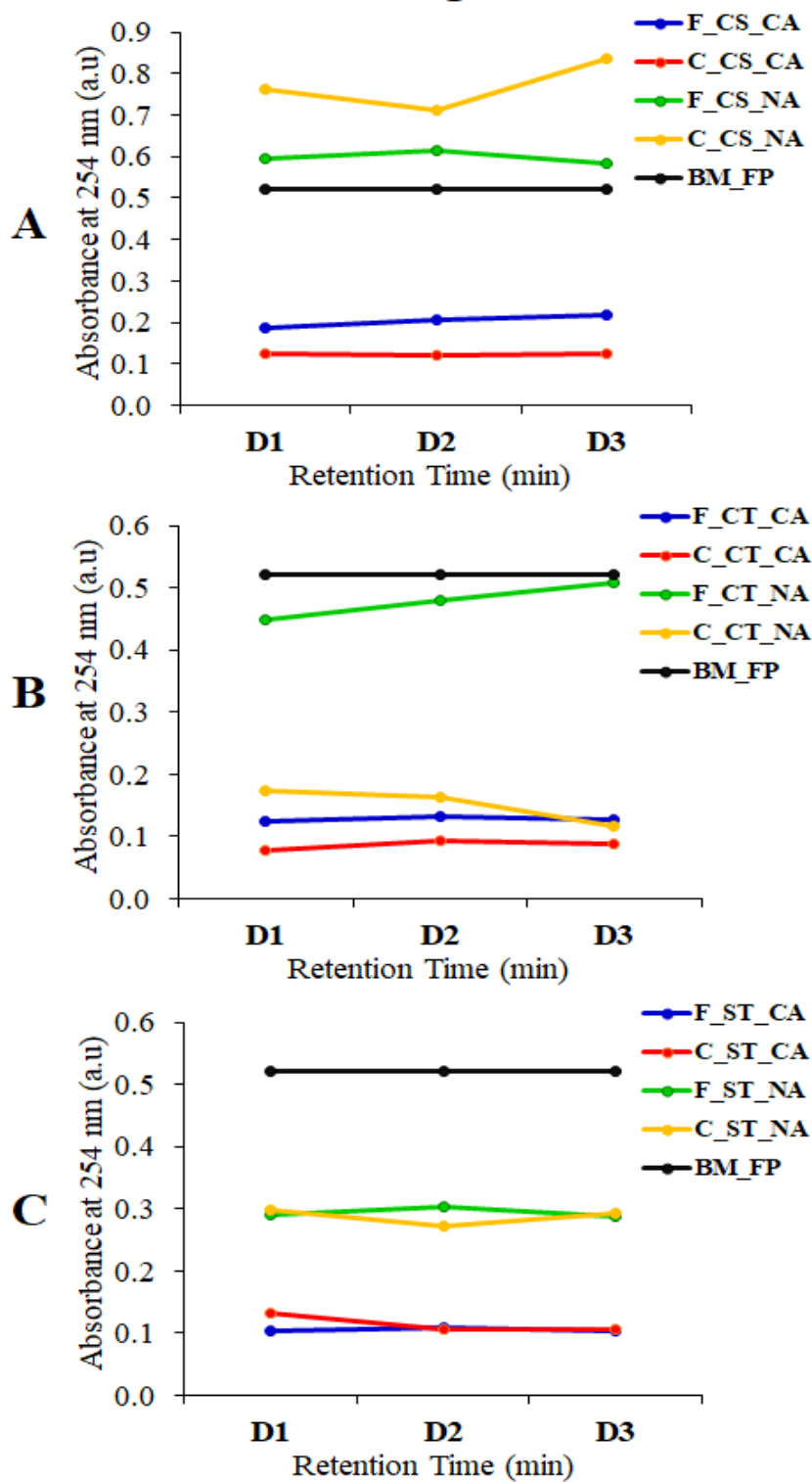


Figure 27: Absorbance at 254 nm for water samples filtered with 20 g of the furnace and conventionally carbonized (A) coconut shell, (B) cassia siamea tree branch, and (C) shea nut tree branch activated carbon adsorbents at 5(D1), 10(D2), and 15(D3) minutes retention times

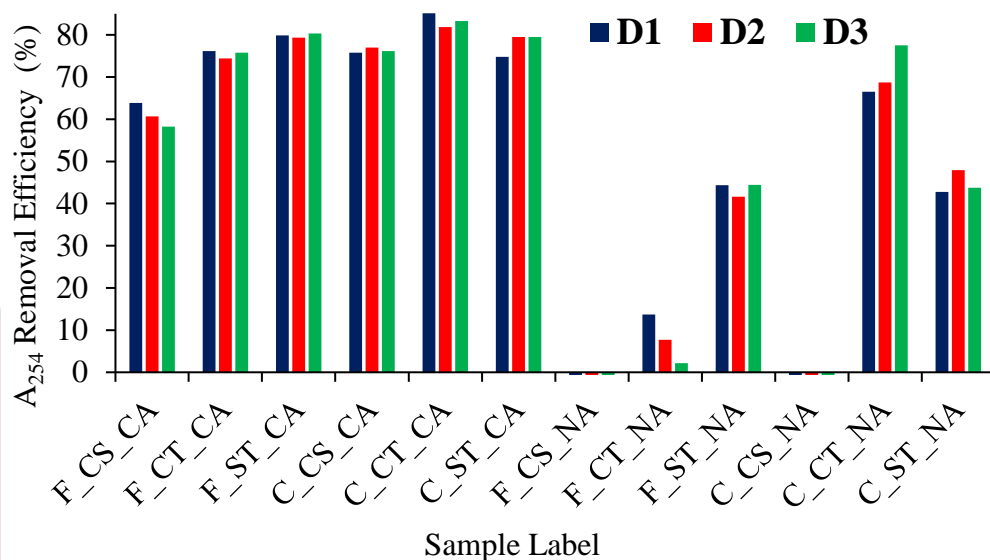


Figure 28: Absorbance removal efficiency for samples filtered with 20 g of the furnace and conventionally carbonized coconut shell (CS), cassia siamea tree (CT) branch, and shea nut tree (ST) branch activated carbon adsorbents at 5(D1), 10(D2), and 15(D3) minutes retention times

Similar trends were also observed for the samples filtered with 30 g of the GAC adsorbent (Figure 29), with C\_CT\_CA giving the highest removal efficiency (88 % minimum and 91 % maximum) for the different retention times. The trend of the other GAC adsorbents, following C\_CT\_CA in terms of performance are as follows; C\_ST\_CA (84% minimum and 86% maximum), F\_ST\_CA (82% minimum and 84% maximum), F\_CT\_CA (74% minimum and 80% maximum), C\_CS\_CA (73% minimum and 77% maximum), and lastly F\_CS\_CA (63% minimum and 67% maximum) as shown in Figure 30.

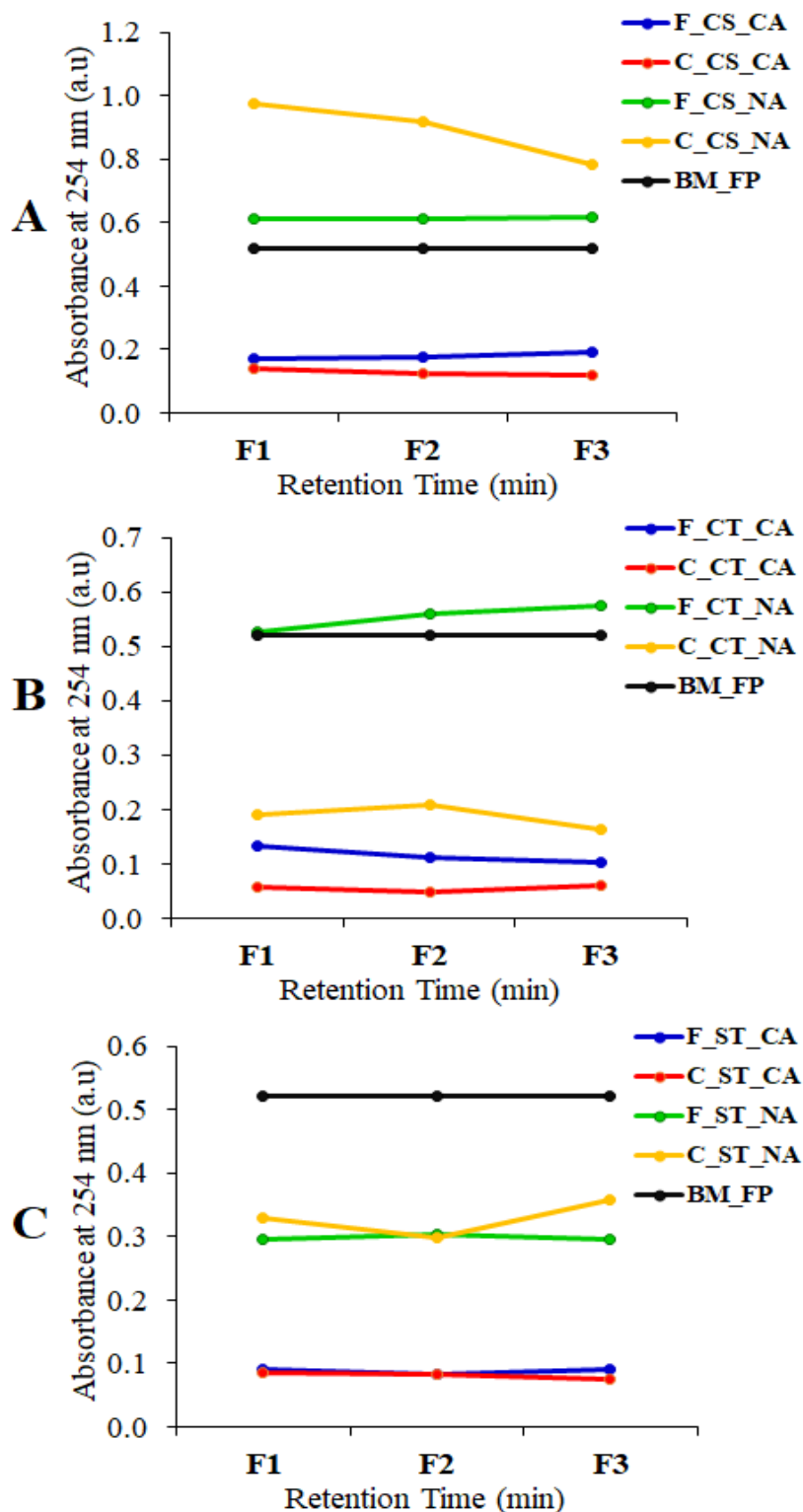
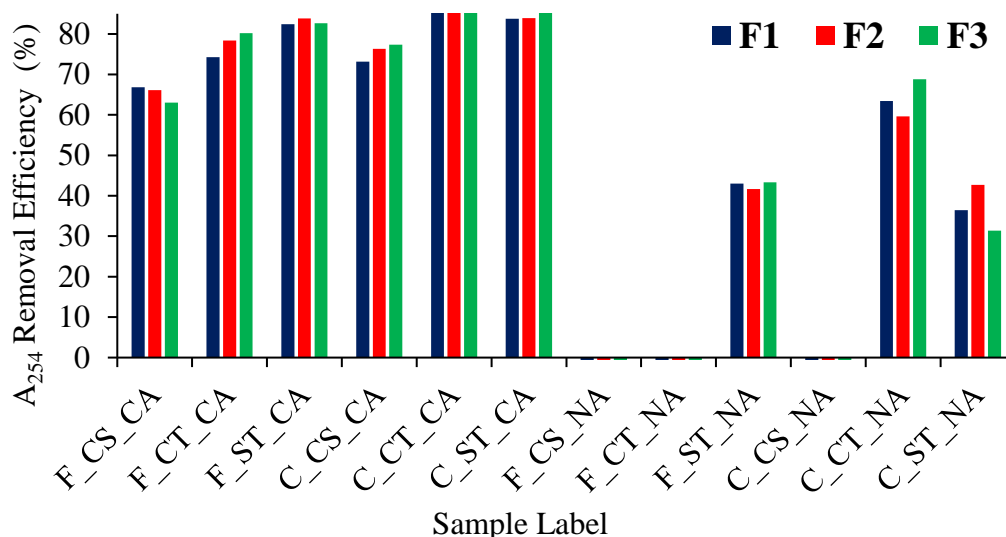


Figure 29: Absorbance at 254 nm for water samples filtered with 30 g of the furnace and conventionally carbonized (A) coconut shell, (B) cassia siamea tree branch, and (C) shea nut tree branch activated carbon adsorbents at 5(F1), 10(F2), and 15(F3) minutes retention times





*Figure 30:* Absorbance removal efficiency for samples filtered with 30 g of the furnace and conventionally carbonized coconut shell (CS), cassia siamea tree (CT) branch, and shea nut tree (ST) branch activated carbon adsorbents at 5(F1), 10(F2), and 15(F3) minutes retention times

Despite the generally good performance of the  $\text{CaCl}_2$ -activated carbon adsorbent, C\_CT\_CA emerged with an averagely high absorbance removal efficiency. Also, the direct effect of retention or contact time on the reduction of absorbance was not consistent for all samples at different adsorbent doses (masses) (Figures 26, 28, and 30). This inconsistency may be attributed to the small-time intervals used and the lack of agitation. The stages of contaminant adsorption onto the GAC may also be controlled by several other factors due to the heterogeneous nature of the GAC (Ndi & Ketcha, 2013).

#### **Absorbance with USB4000 spectrometer**

The absorbance spectra for all filtered and unfiltered water samples from the USB4000 spectrometer system are shown in Figures 31, 33, and 35. The spectra exhibited single peaks for all samples, with the peak intensities at approximately 245 nm, representing the corresponding sample's absorbance.

The standard water sample (distilled water) exhibited the absence of any absorbing contaminant, thus showcasing a zero (0) absorbance peak intensity at 245 nm. This standard absorbance value was used to standardise the absorbance for all other samples, as illustrated in Figures 31, 33, and 35.

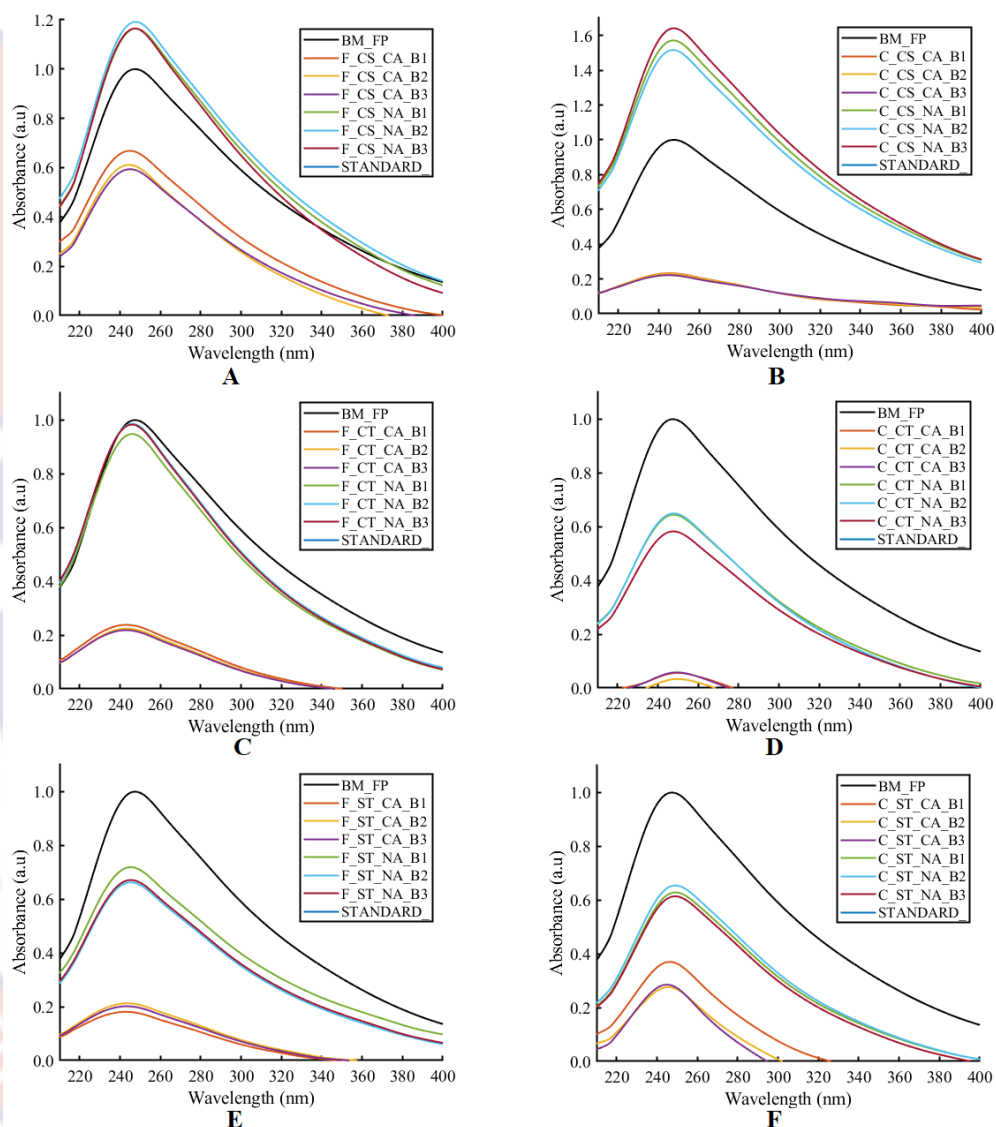


*Figure 31:* Absorbance spectra for samples filtered with 10 g of the (A) furnace carbonized coconut shell, (B) conventionally carbonized coconut shell, (C) furnace carbonized cassia siamea tree branch, (D) conventionally carbonized cassia siamea tree branch, (E) furnace carbonized shea nut tree branch, and (F) conventionally carbonized shea nut tree branch activated carbon adsorbents

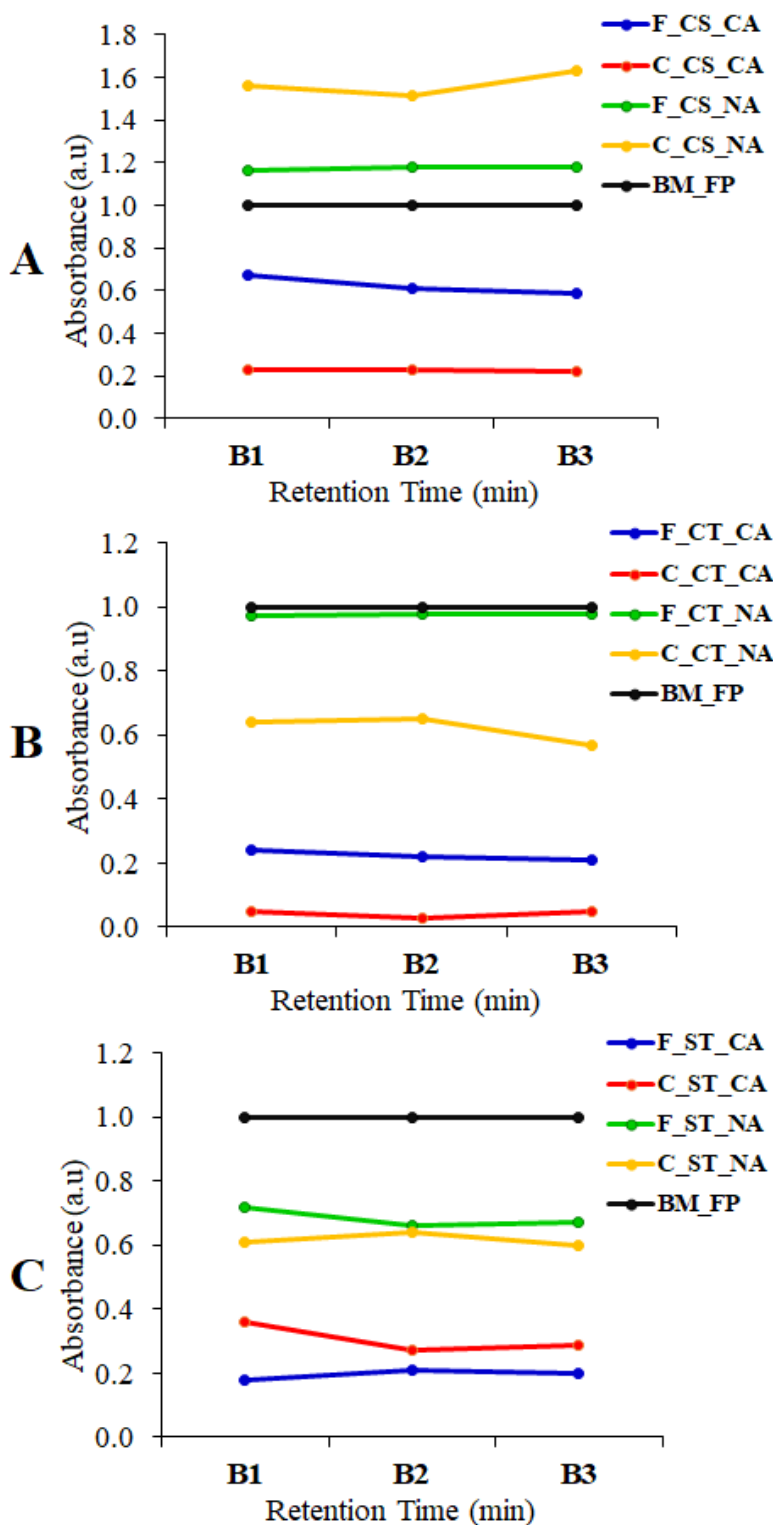


Figure 32: Absorbance peaks at 245 nm for samples filtered with 10 g of the furnace and conventionally carbonized (A) coconut shell, (B) cassia siamea tree branch, and (C) shea nut tree branch activated carbon adsorbents at 5(B1), 10(B2), and 15(B3) minutes retention times

The peak absorbance intensities were also extracted at 245 nm wavelength for each sample, and plotted against the retention or contact time as shown in Figures 32, 34, and 36 for 10 g, 20 g, and 30 g adsorbent doses. Again, all samples filtered with  $\text{CaCl}_2$ -activated GAC adsorbents showed generally low absorbance intensities (0.05 to 0.65 a.u) compared to those filtered with the NaCl-activated adsorbents (0.5 to 2.2 a.u) (Figures 32 to 36).

For samples filtered with 10 g of the prepared GAC, C\_CT\_CA gave the lowest absorbance peak intensity range of 0.03 – 0.05 a.u at 245 nm. This performance was followed closely by the performance of F\_ST\_CA (0.18 – 0.21 a.u), F\_CT\_CA (0.21 – 0.24 a.u), C\_CS\_CA (0.23 a.u), C\_ST\_CA (0.27 – 0.36 a.u), and then F\_CS\_CA (0.59 – 0.67 a.u) as seen in Figure 32.

The absorbance spectra for samples filtered with 20 g of GAC adsorbents are shown in Figure 33. C\_CT\_CA again gave the lowest absorbance intensity of zero (0) at 245 nm for all three different retention times, indicating a 100 % reduction in the absorbance of the surface water sample (Figure 27). This was followed immediately by F\_ST\_CA, then F\_CT\_CA, C\_ST\_CA, C\_CS\_CA, and lastly, F\_CS\_CA (Figure 27).

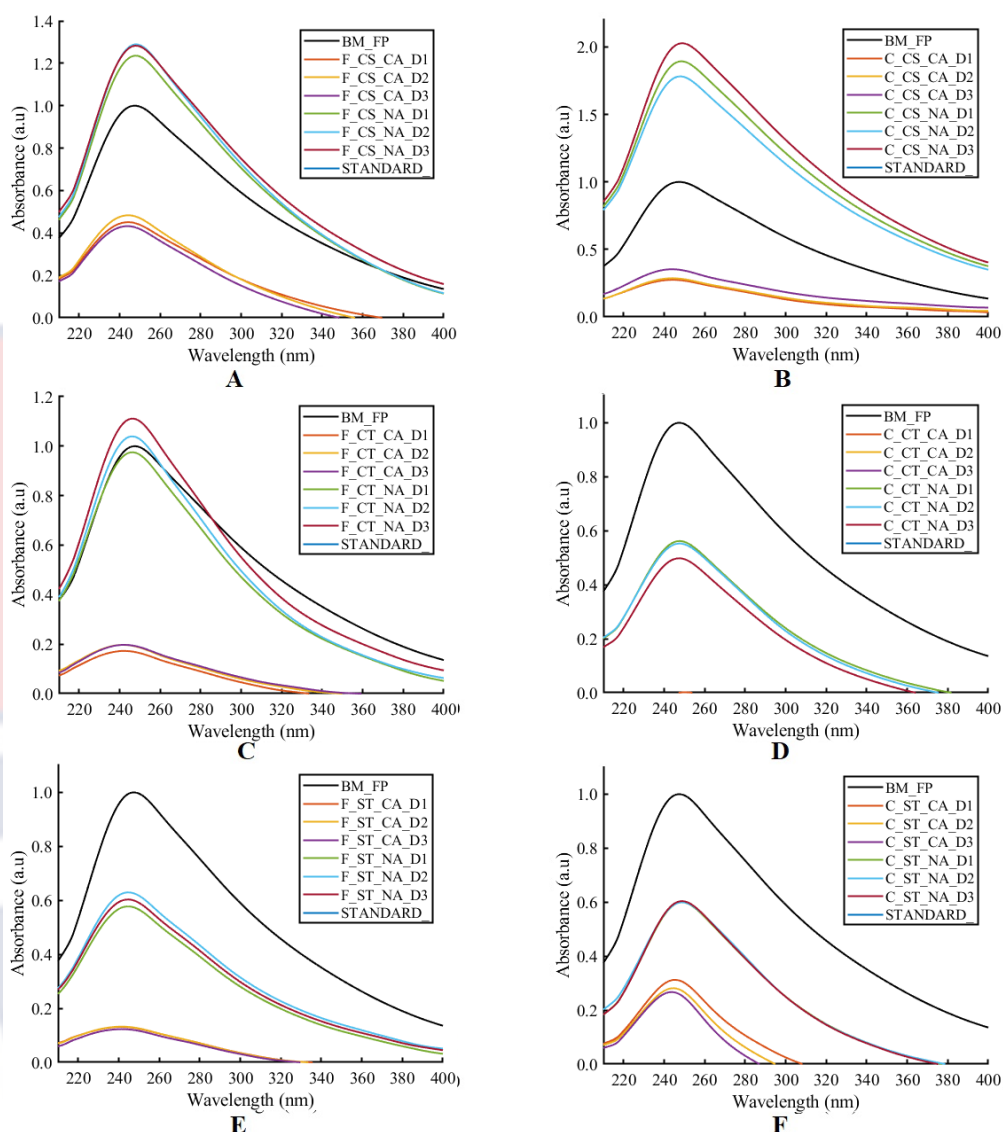


Figure 33: Absorbance spectra for samples filtered with 20 g of the (A) furnace carbonized coconut shell, (B) conventionally carbonized coconut shell, (C) furnace carbonized cassia siamea tree branch, (D) conventionally carbonized cassia siamea tree branch, (E) furnace carbonized shea nut tree branch, and (F) conventionally carbonized shea nut tree branch activated carbon adsorbents



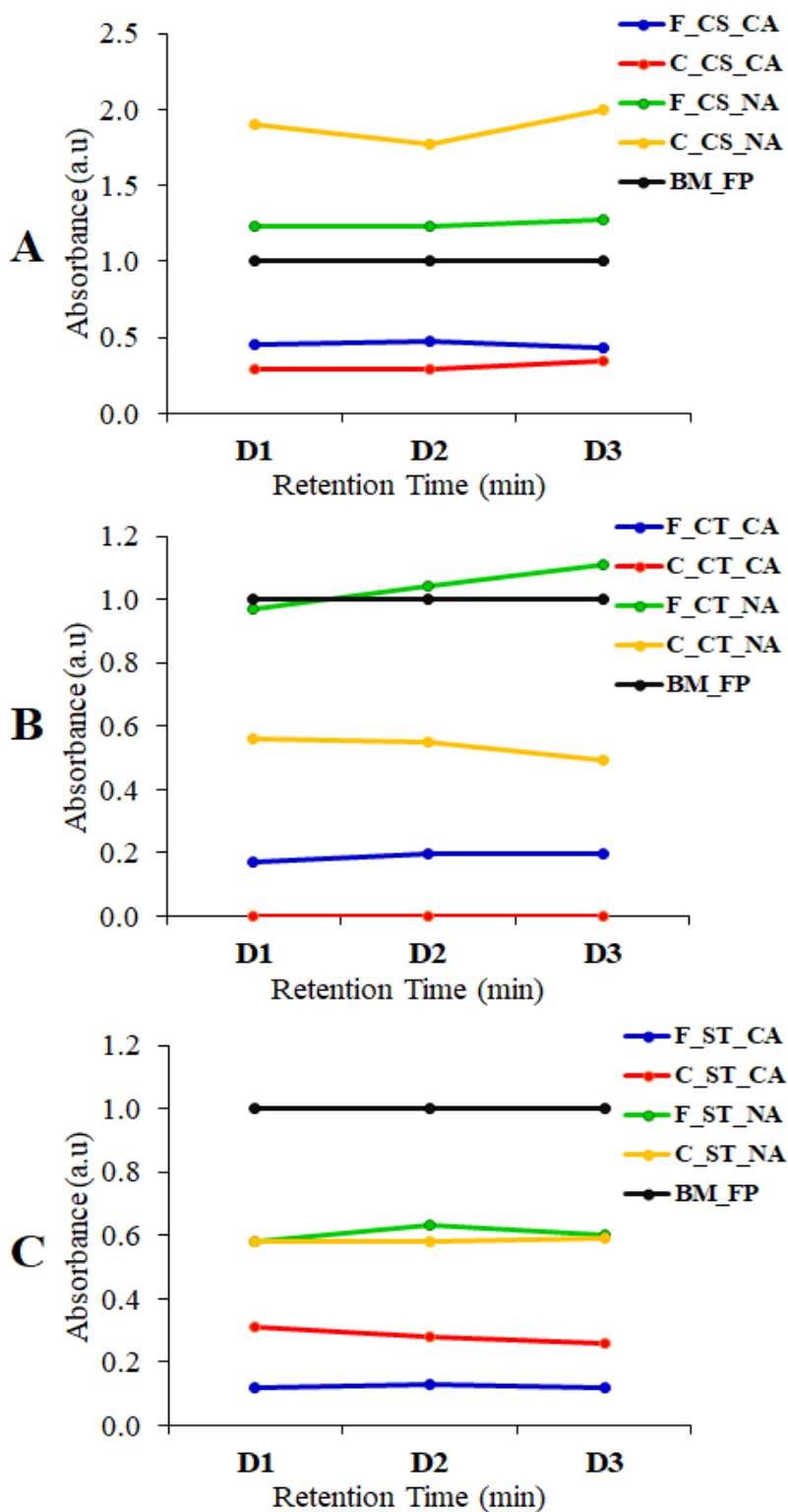
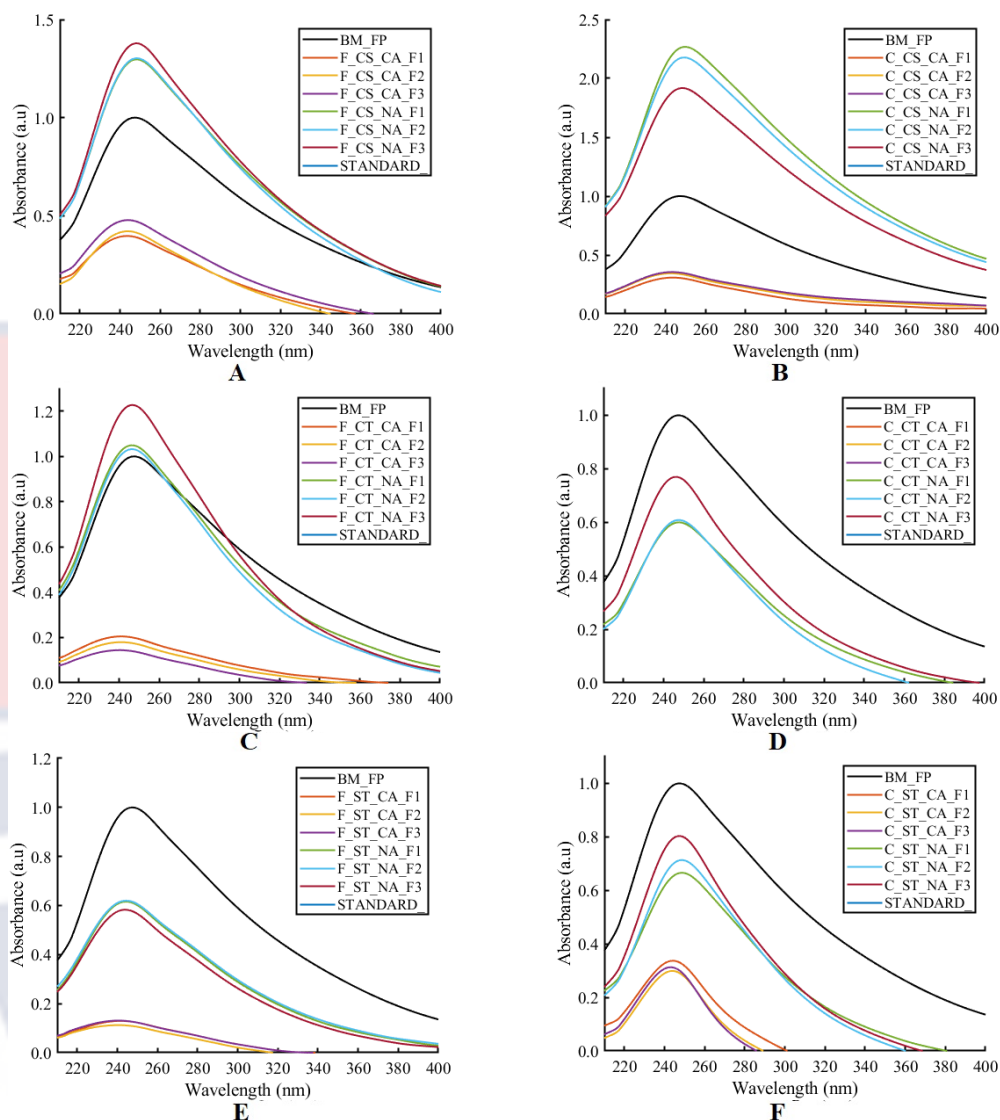


Figure 34: Absorbance peaks at 245 nm for samples filtered with 20 g of the furnace and conventionally carbonized (A) coconut shell, (B) cassia siamea tree branch, and (C) shea nut tree branch activated carbon adsorbents at 5(D1), 10(D2), and 15(D3) minutes retention times



**Figure 35:** Absorbance spectra for samples filtered with 30 g of the (A) furnace carbonized coconut shell, (B) conventionally carbonized coconut shell, (C) furnace carbonized cassia siamea tree branch, (D) conventionally carbonized cassia siamea tree branch, (E) furnace carbonized shea nut tree branch, and (F) conventionally carbonized shea nut tree branch activated carbon adsorbents

The absorbance spectra for samples filtered with 30 g of the prepared GAC adsorbents are also illustrated in Figure 35. C\_CT\_CA once again gave the lowest absorbance intensity of zero (0 a.u) at 245 nm for all three different retention times, indicating a 100 % reduction in the absorbance of the surface water sample (Figure 36).

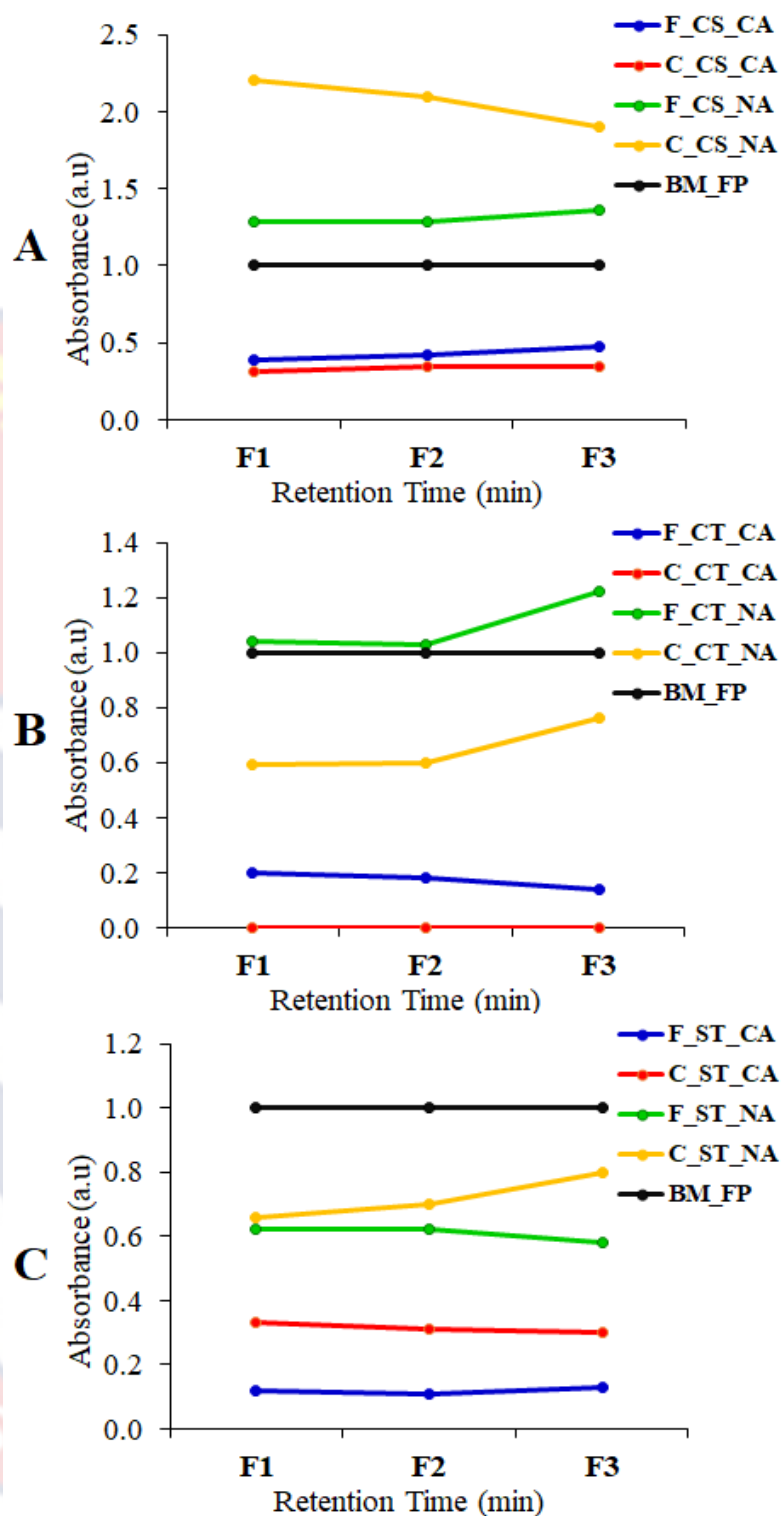


Figure 36: Absorbance peaks at 245 nm for samples filtered with 30 g of the furnace and conventionally carbonized (A) coconut shell, (B) cassia siamea tree branch, and (C) shea nut tree branch activated carbon adsorbents at 5(F1), 10(F2), and 15(F3) minutes retention times

This performance was followed immediately by F\_ST\_CA (0.11 – 0.12 a.u), then F\_CT\_CA (0.14 – 0.20 a.u), C\_ST\_CA (0.30 – 0.33 a.u), C\_CS\_CA (0.31 – 0.35 a.u), and lastly, F\_CS\_CA (0.40 – 0.48 a.u) (Figure 36). The same trend in adsorbent performance was observed for all three masses of the CaCl<sub>2</sub>-activated adsorbents used, with C\_ST\_CA and C\_CS\_CA switching positions due to the very slight difference in their performance. The performance observation trends closely resemble the absorbance measurements at 254 nm, as depicted in Figure 25 to 30, in terms of the absorbance ranges for CaCl<sub>2</sub> and NaCl. This suggests a strong correlation between the two analytical techniques

However, the direct effect of the retention or contact time on the reduction of absorbance was not consistent for all adsorbents and the different masses (Figures 32, 34, and 36). This may be attributed to the small-time intervals and the lack of agitation. The stages of contaminant adsorption onto the GAC may also be controlled by several other factors due (porosity, microspheres, pore surface area, particle size, etcetera) to the heterogeneous nature of the GAC (Ndi & Ketcha, 2013).

### **Ultraviolet Light Emitting Diode Transmittance**

In water quality assessment, Ultraviolet (UV) LED-induced transmittance is the percentage of UV light transmitted through a water sample at a specific UV wavelength. The inverse correlation between transmitted intensity and contaminant concentration is illustrated in Figures 37 to 39. These transmittance spectra also demonstrate the DOM removal capacity of the CaCl<sub>2</sub>-activated adsorbents compared to their NaCl-activated counterparts.

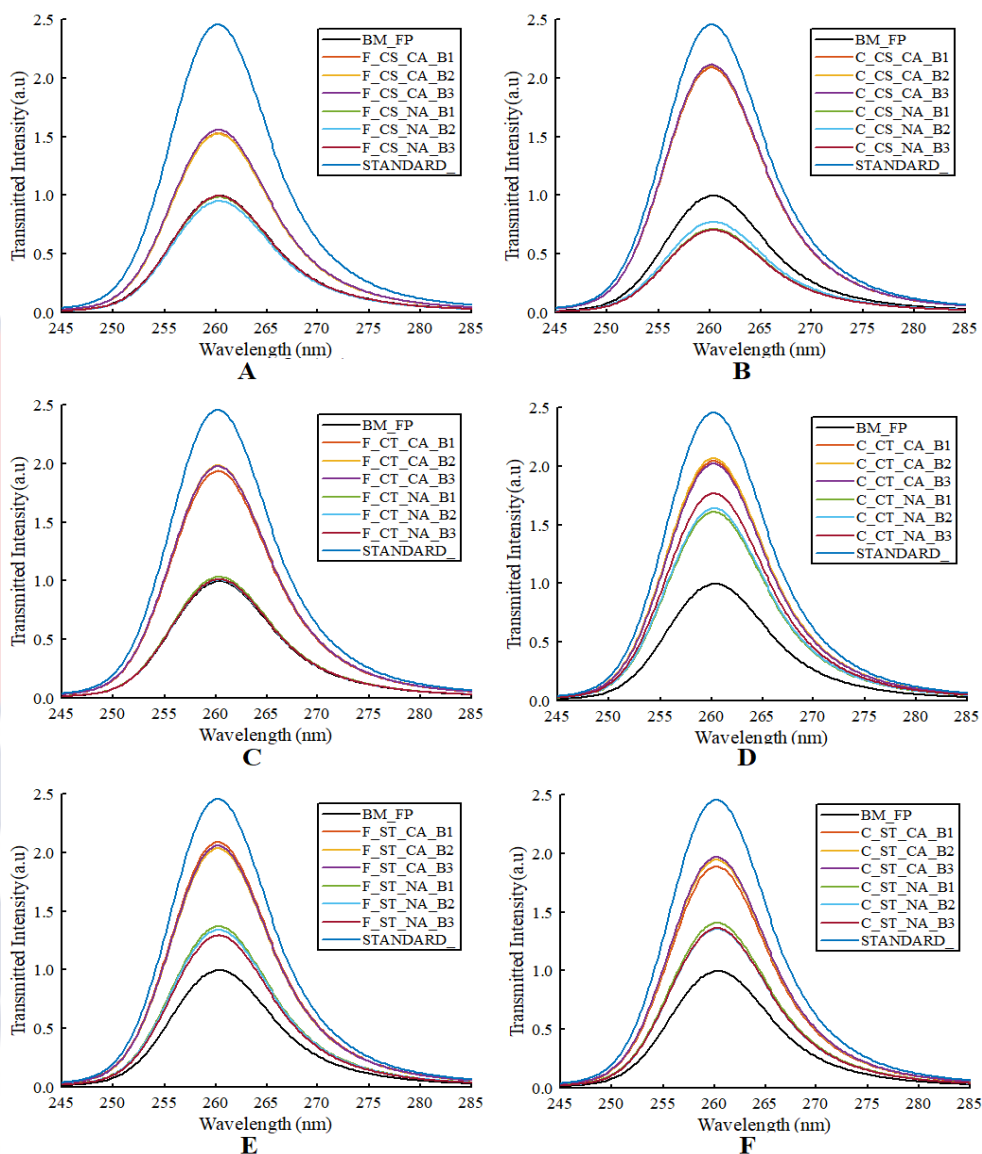


Figure 37: UV LED induced transmittance for samples filtered with 10 g of the (A) furnace carbonized coconut shell, (B) conventionally carbonized coconut shell, (C) furnace carbonized cassia siamea tree branch, (D) conventionally carbonized cassia siamea tree branch, (E) furnace carbonized shea nut tree branch, and (F) conventionally carbonized shea nut tree branch activated carbon adsorbents.

The good performance of  $\text{CaCl}_2$ -activated adsorbents was observed for the different adsorbent masses as showcased in the line plots of the extracted peak intensities at 260 nm. All the  $\text{CaCl}_2$ -activated adsorbents showed more significant DOM removal potential (Figures 38, 40, and 42).



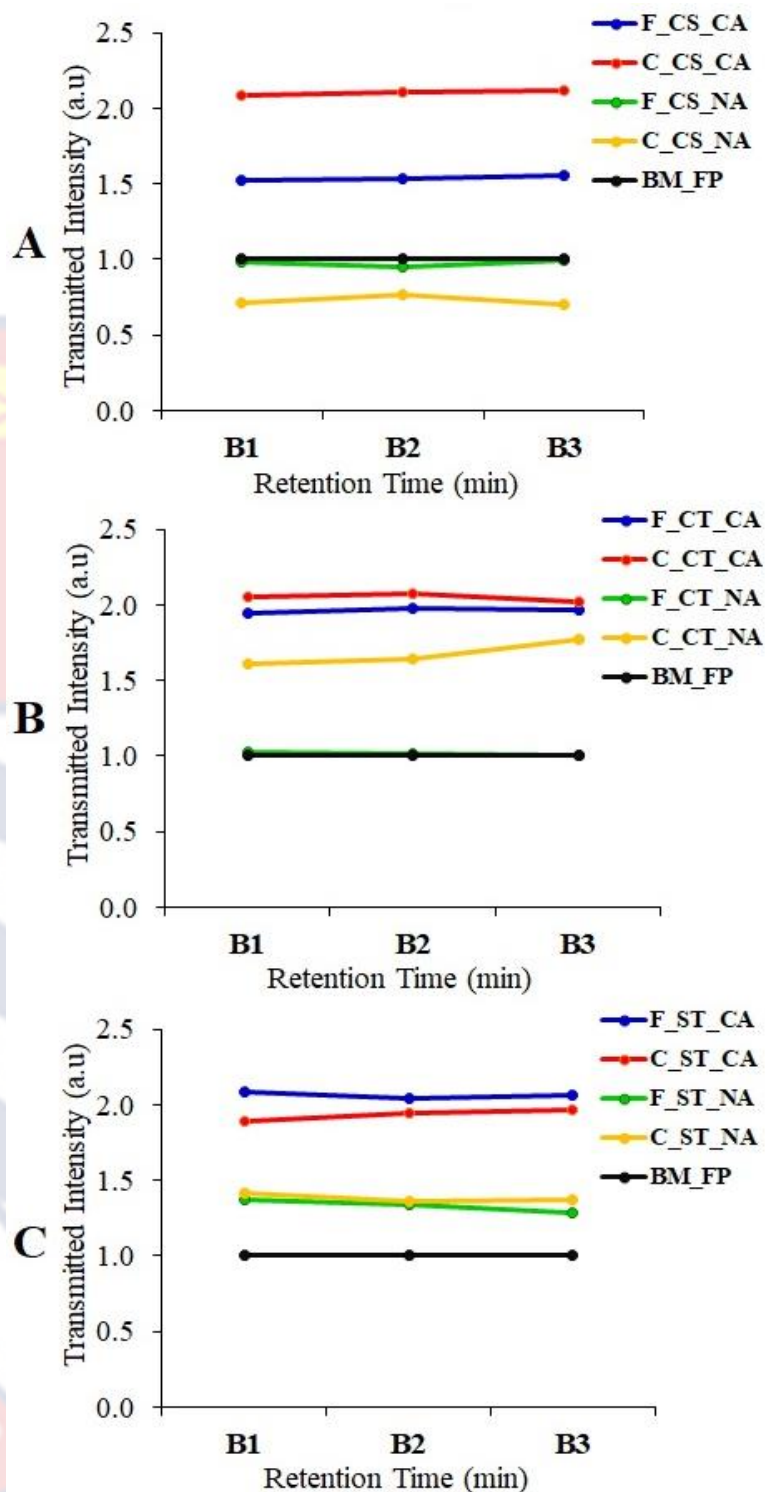


Figure 38: UV LED induced transmittance for samples filtered with 10 g of the furnace and conventionally carbonized (A) coconut shell, (B) cassia siamea tree branch, and (C) shea nut tree branch activated carbon adsorbents at 5(B1), 10(B2), and 15(B3) minutes retention times

Figures 37 and 38, illustrate the transmittance for samples filtered with 10 g of each prepared GAC adsorbent. C\_CS\_CA was observed to give the highest transmitted intensity at the selected peak wavelength of 260 nm (2.09 minimum and 2.12 maximum). This performance was, however, matched by the transmitted intensities of F\_ST\_CA (2.06 minimum and 2.09 maximum) and C\_CT\_CA (2.02 minimum and 2.07 maximum). The performance of these three GAC adsorbents was followed by that of F\_CT\_CA (1.94 minimum and 1.98 maximum), C\_ST\_CA (1.89 minimum and 1.97 maximum), and F\_CS\_CA (1.52 minimum and 1.56 maximum) (Figure 38).

Similarly, Figures 39 and 40, illustrates the transmittance for samples filtered with 20 g of each prepared GAC adsorbent. A slight change in the adsorbent performance trend was observed for the 20 g adsorbent dose, with C\_CT\_CA giving the highest transmitted intensity (2.23 minimum and 2.27 maximum). This performance was comparable to F\_ST\_CA (2.19 minimum and 2.22 maximum) and F\_CT\_CA (2.12 minimum and 2.15 maximum). These performances were followed by those of C\_ST\_CA (2.06 minimum and 2.09 maximum), C\_CS\_CA (1.86 minimum and 1.97 maximum), and F\_CS\_CA (1.62 minimum and 1.72 maximum), as shown in Figure 40.

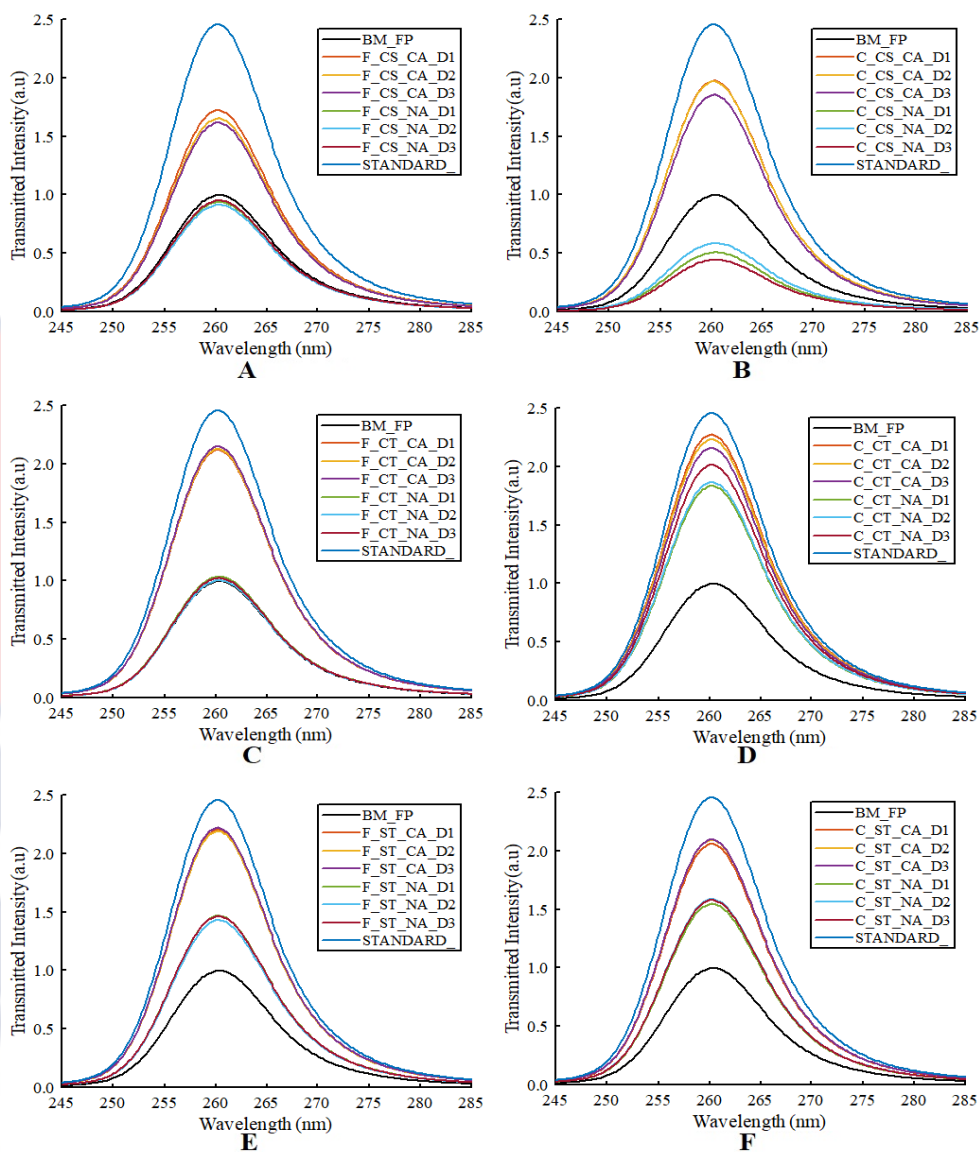


Figure 39: UV LED induced transmittance for samples filtered with 20 g of the (A) furnace carbonized coconut shell, (B) conventionally carbonized coconut shell, (C) furnace carbonized cassia siamea tree branch, (D) conventionally carbonized cassia siamea tree branch, (E) furnace carbonized shea nut tree branch, and (F) conventionally carbonized shea nut tree branch activated carbon adsorbents

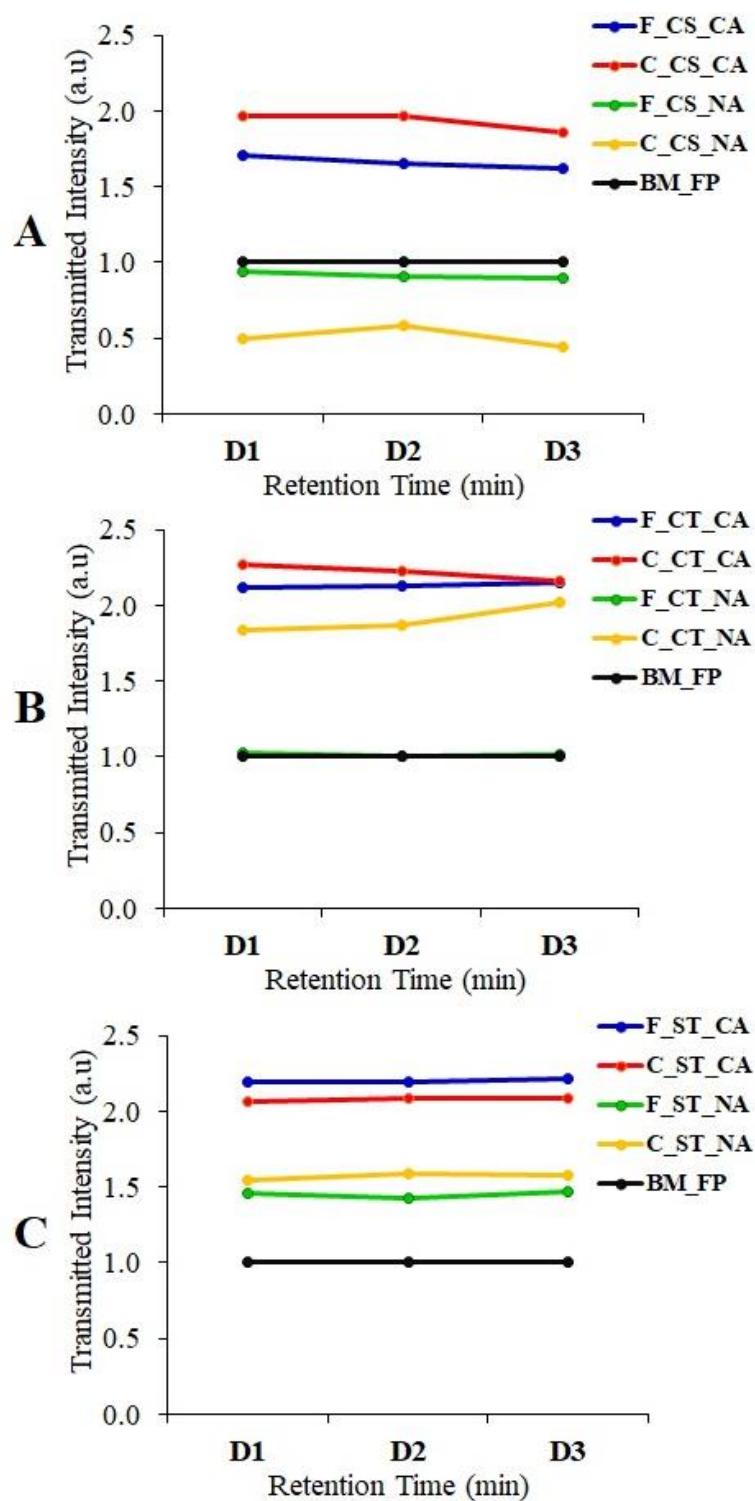


Figure 40: UV LED induced transmittance for samples filtered with 20 g of the furnace and conventionally carbonized (A) coconut shell, (B) cassia siamea tree branch, and (C) shea nut tree branch activated carbon adsorbents at 5(D1), 10(D2), and 15(D3) minutes retention times

On the other hand, Figures 41 and 42, show the transmittance for samples filtered with 30 g of each prepared GAC adsorbent. For this adsorbent dose, C\_CT\_CA was again observed to give the highest transmitted intensity (2.21 minimum and 2.29 maximum).

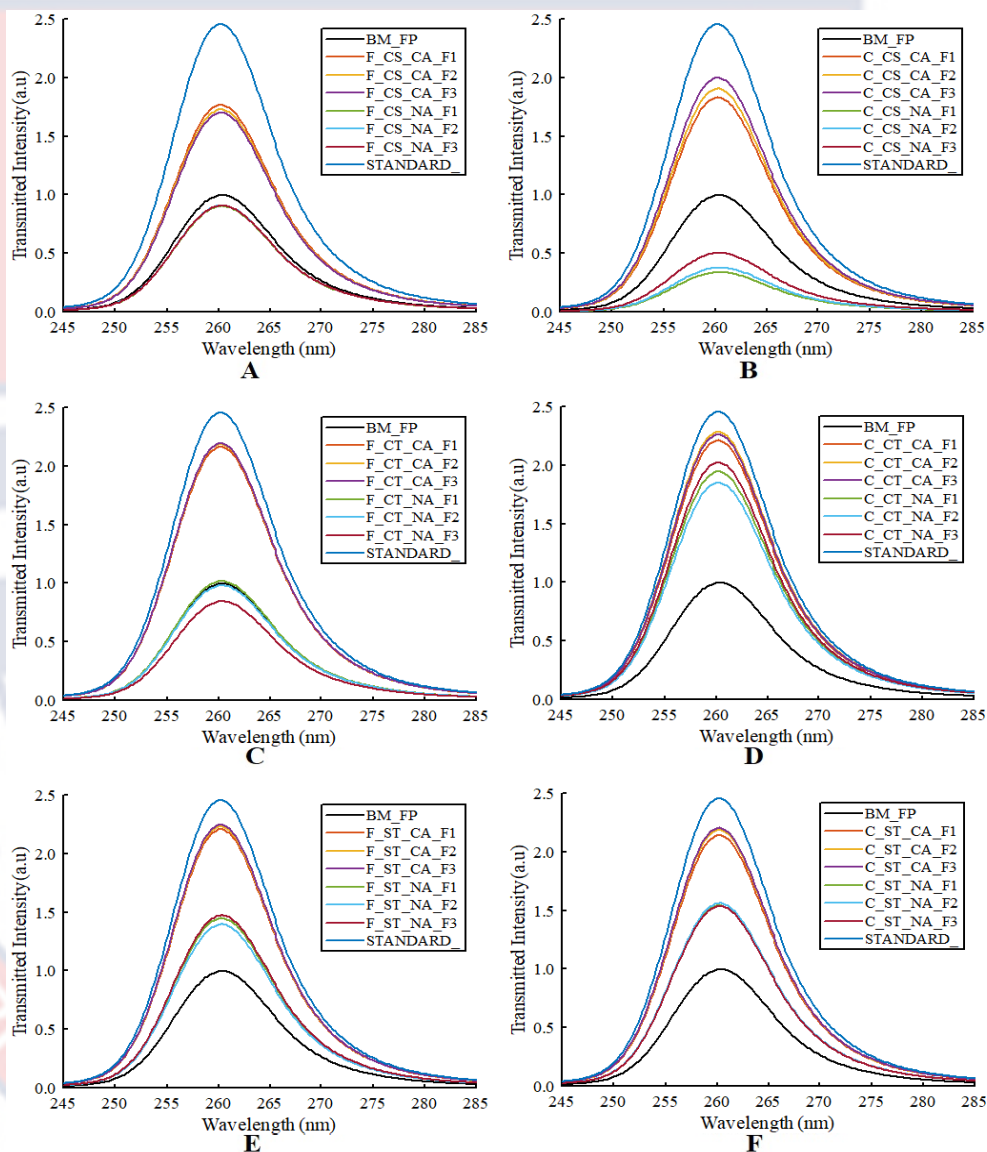


Figure 41: UV LED induced transmittance for samples filtered with 30 g of the (A) furnace carbonized coconut shell, (B) conventionally carbonized coconut shell, (C) furnace carbonized cassia siamea tree branch, (D) conventionally carbonized cassia siamea tree branch, (E) furnace carbonized shea nut tree branch, and (F) conventionally carbonized shea nut tree branch activated carbon adsorbents



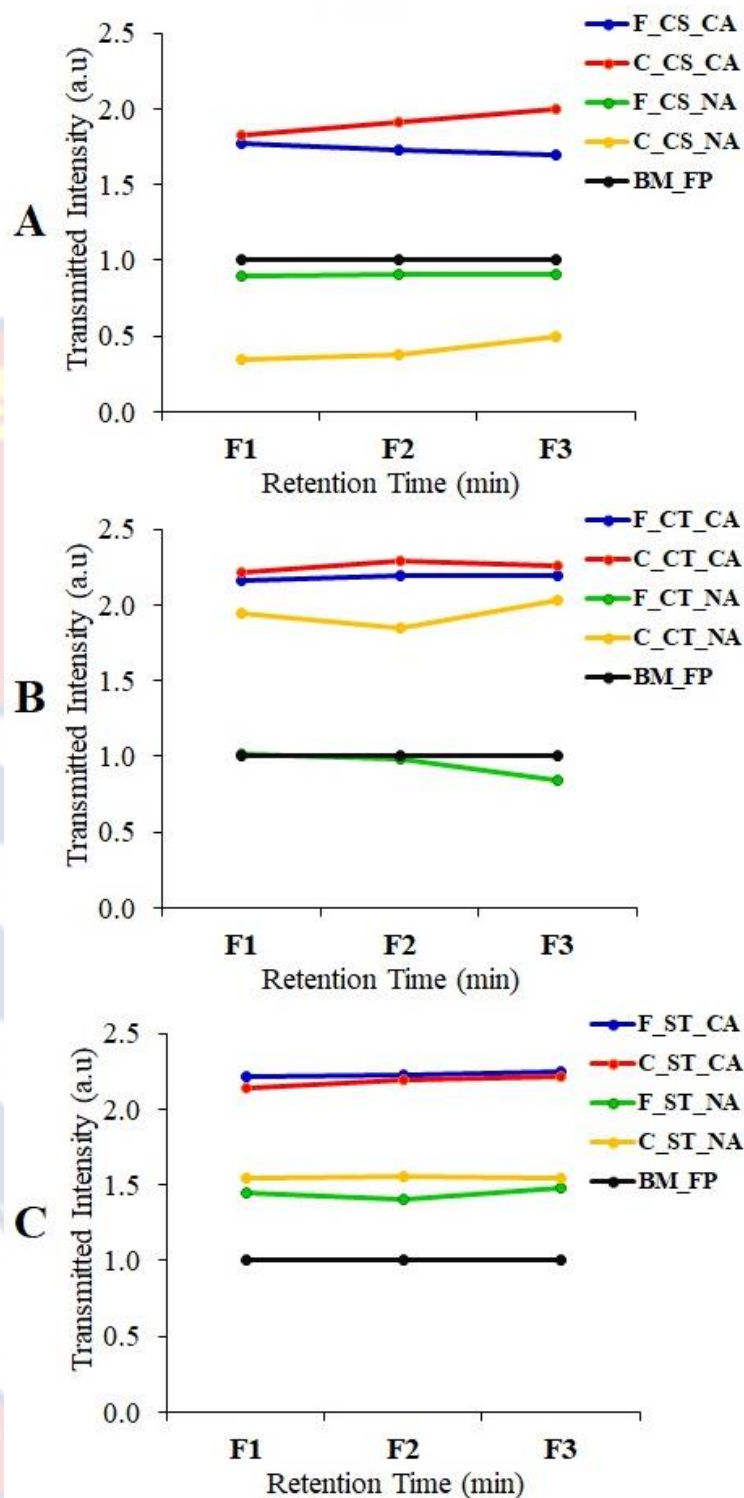


Figure 42: UV LED induced transmittance for samples filtered with 30 g of the furnace and conventionally carbonized (A) coconut shell, (B) cassia siamea tree branch, and (C) shea nut tree branch activated carbon adsorbents at 5(F1), 10(F2), and 15(F3) minutes retention times.

This result was matched by the transmitted intensities of F\_ST\_CA (2.21 minimum and 2.25 maximum) and C\_ST\_CA (2.14 minimum and 2.21 maximum). The contaminant removal performance of these three GAC adsorbents was followed by those of F\_CT\_CA (2.16 minimum and 2.19 maximum), C\_CS\_CA (1.83 minimum and 2.00 maximum), and F\_CS\_CA (1.7 minimum and 1.73 maximum, as shown in Figure 42).

The difference in the trend of adsorbent performance for the different adsorbent doses (10 g, 20 g, and 30 g) may be attributed to the fact that, as the adsorbent mass or dose increases, there is a general decrease in adsorption sites caused by overlapping sites as the surface area increases (Ndi & Ketcha, 2013). Conversely, a slight difference was also observed in the trends between the absorbance and transmittance techniques at low adsorbent doses. This contrast may be due to the use of different excitation or fingerprint wavelengths (254 nm, 245 nm, and 225 nm), thus, indicating the different components of DOM (Bolton, 2003; Carstea et al., 2020; Hudson, Baker, & Reynolds, 2007).

The results of this UV LED transmittance technique offer valuable insight into the protein component of the DOM concentration in each filtered and unfiltered water sample. Moreover, due to its correlation with  $A_{254}$  at higher adsorbent dose, UV LED-IT is a cost-effective surrogate for rapid point-of-use water quality assessment, which is critical in water delivery systems.

### **Laser-Induced Fluorescence**

The laser-induced fluorescence (LIF) emission spectra for the unfiltered and standard (distilled) water samples were compared to the emission spectra of the water samples filtered with the twelve (12) prepared GAC adsorbents; F\_CS\_CA, F\_CS\_NA, C\_CS\_CA, C\_CS\_NA, F\_CT\_CA, F\_CT\_NA,

C\_CT\_CA, C\_CT\_NA, F\_ST\_CA, F\_ST\_NA, C\_ST\_CA, and C\_ST\_NA, at the selected adsorbent masses and retention times.

The emission spectra in Figures 43, 44, and 45, were induced by a 405 nm excitation wavelength, which produced spectra with single peaks representing the humic substance concentration in the samples (Hudson et al., 2007; Khan et al., 2014; Yunus, 2018). Figures 43 to 48 depict that samples filtered with CaCl<sub>2</sub>-activated adsorbents showed higher DOM fluorescence reduction than those filtered with the NaCl-activated adsorbents

For water samples filtered with 10 g of each adsorbent (Figures 43 and 44), a clear distinction between the performances of CaCl<sub>2</sub>-activated and NaCl-activated adsorbents was again observed. F\_CS\_NA, C\_CS\_NA, and F\_CT\_NA showed DOM fluorescence intensities above that of the raw water sample (Bm\_FP). This increase in DOM fluorescence intensity for samples filtered with the NaCl-activated adsorbents indicates the addition of colour. This may be attributed to the tanning effect of these adsorbents. Moona (2021), asserted that, although, the predominance of micro-pores in most shell-based GAC gives it a brittle touch and high mechanical strength, the inadequacy of macropores may lead to a tanning effect at smaller sieve sizes.

The performance of C\_CS\_CA with DOM removal efficiencies of 86% and 92.5% are shown in Figures 43 and 44, respectively. This performance was compared with F\_CT\_CA (74%) and F\_ST\_CA (72% minimum and 77% maximum). These were followed closely by C\_CT\_CA (69% minimum and 73% maximum) and C\_ST\_CA (57% minimum and 69% maximum).

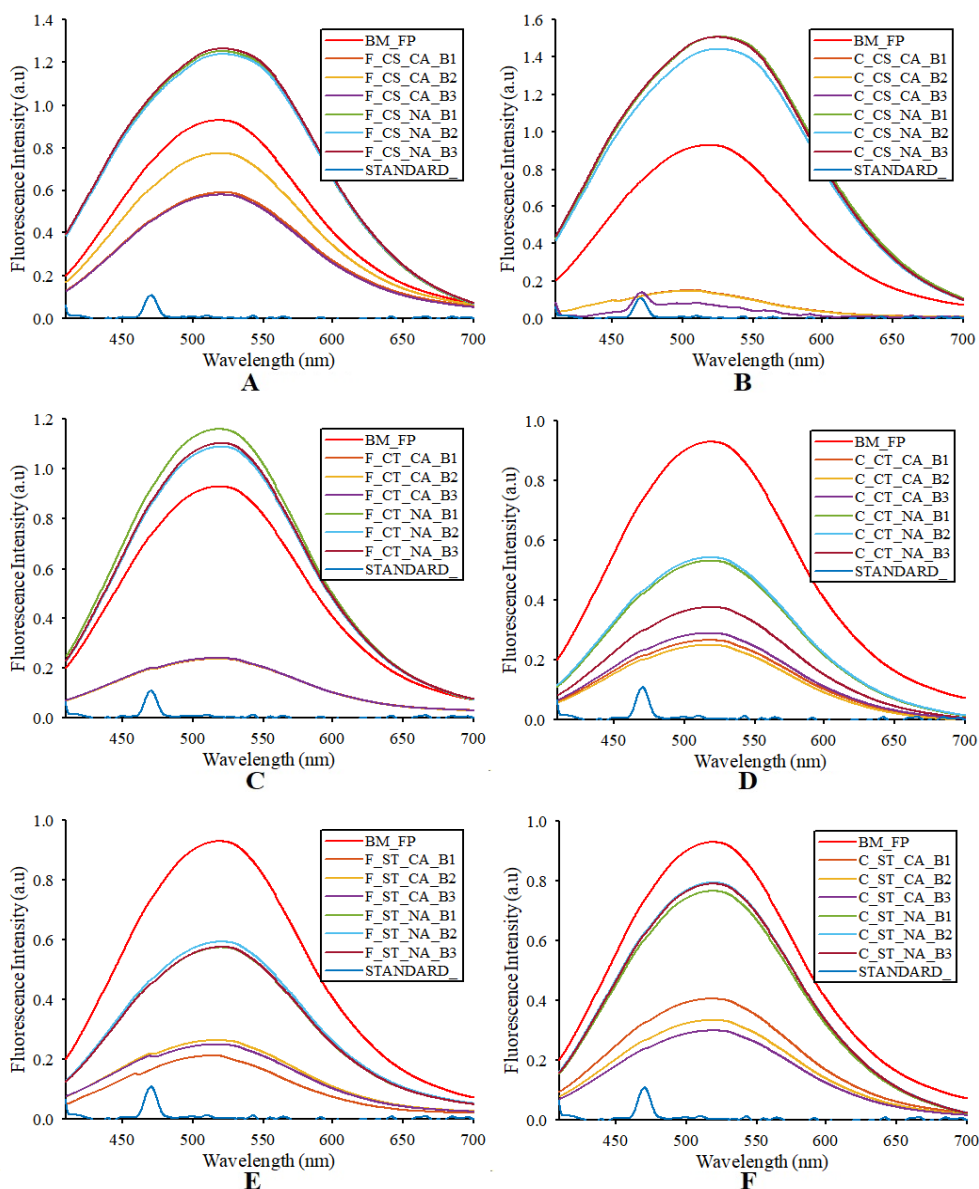


Figure 43: LIF spectra of all samples filtered with 10 g of the (A) furnace carbonized coconut shell, (B) conventionally carbonized coconut shell, (C) furnace carbonized cassia siamea tree branch, (D) conventionally carbonized cassia siamea tree branch, (E) furnace carbonized shea nut tree branch, and (F) conventionally carbonized shea nut tree branch activated carbon adsorbents.

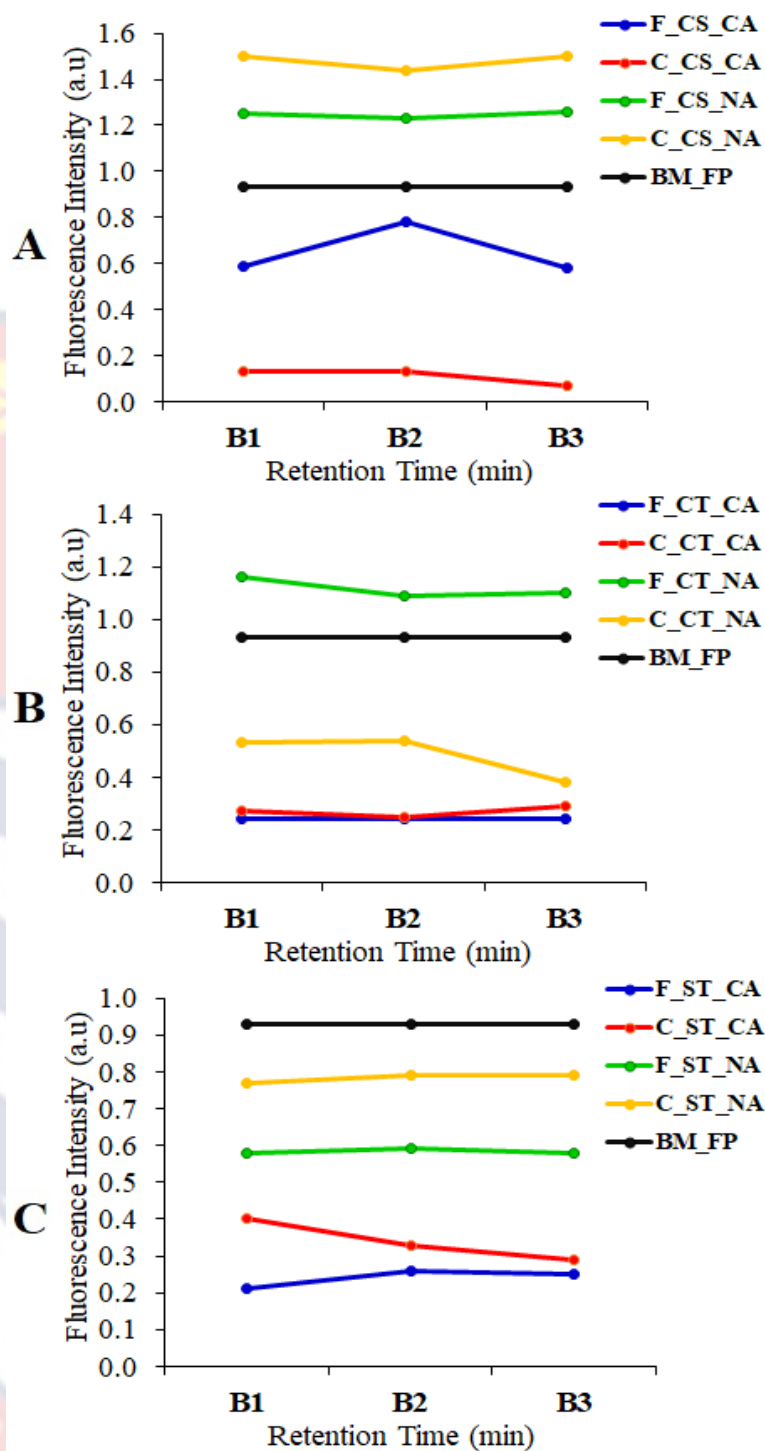


Figure 44: LIF peak intensities at 520 nm for samples filtered with 10 g of the furnace and conventionally carbonized (A) coconut shell, (B) cassia siamea tree branch, and (C) shea nut tree branch activated carbon adsorbents at 5(B1), 10(B2), and 15(B3) minutes retention times.



Figures 45 and 46, revealed a similar trend in performance for the 20 g adsorbent dose, with C\_CT\_CA giving a minimum and maximum DOM removal efficiency of 84% and 85%, respectively.

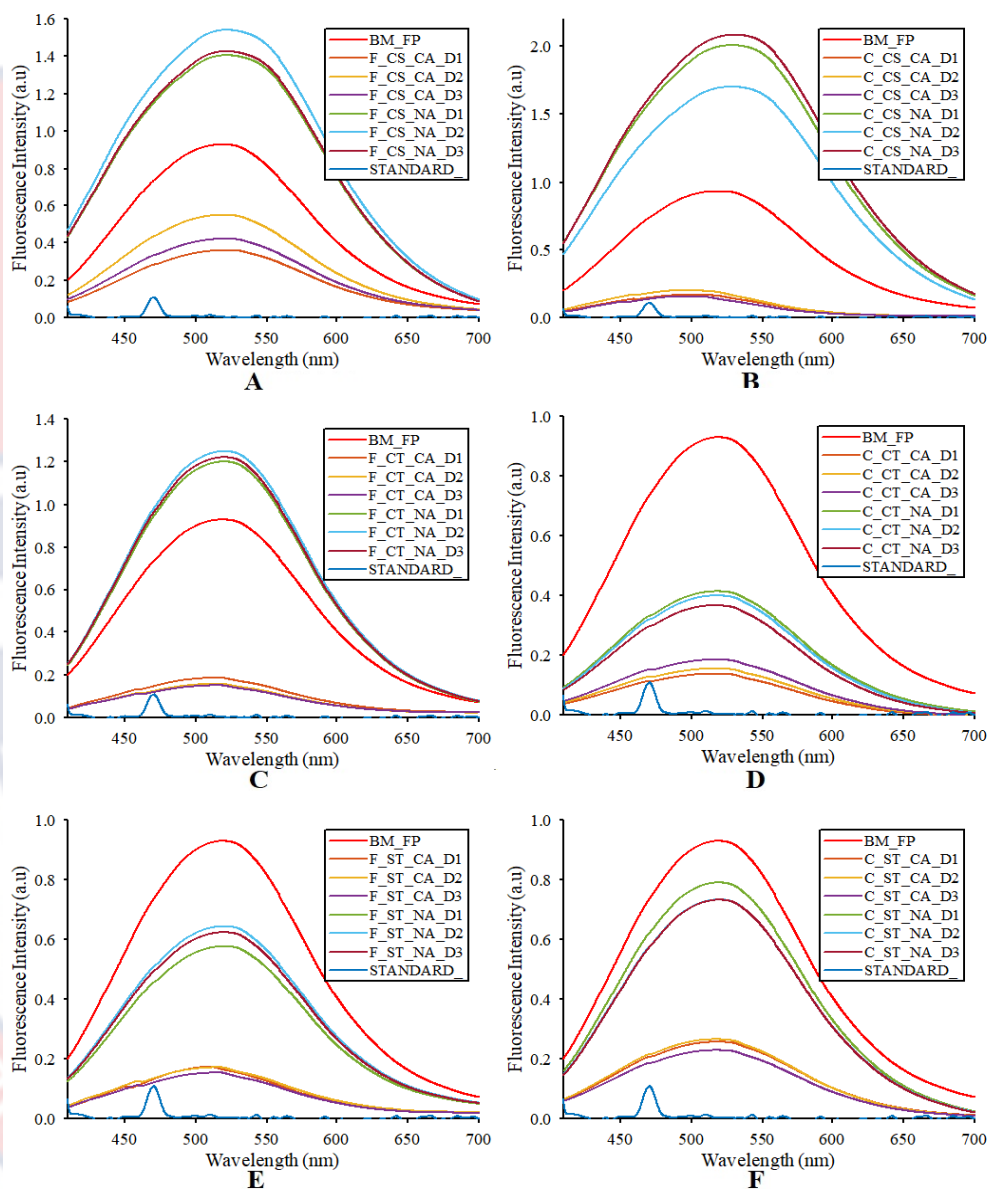


Figure 45: LIF spectra of all samples filtered with 20 g of the (A) furnace carbonized coconut shell, (B) conventionally carbonized coconut shell, (C) furnace carbonized cassia siamea tree branch, (D) conventionally carbonized cassia siamea tree branch, (E) furnace carbonized shea nut tree branch, and (F) conventionally carbonized shea nut tree branch activated carbon adsorbents.

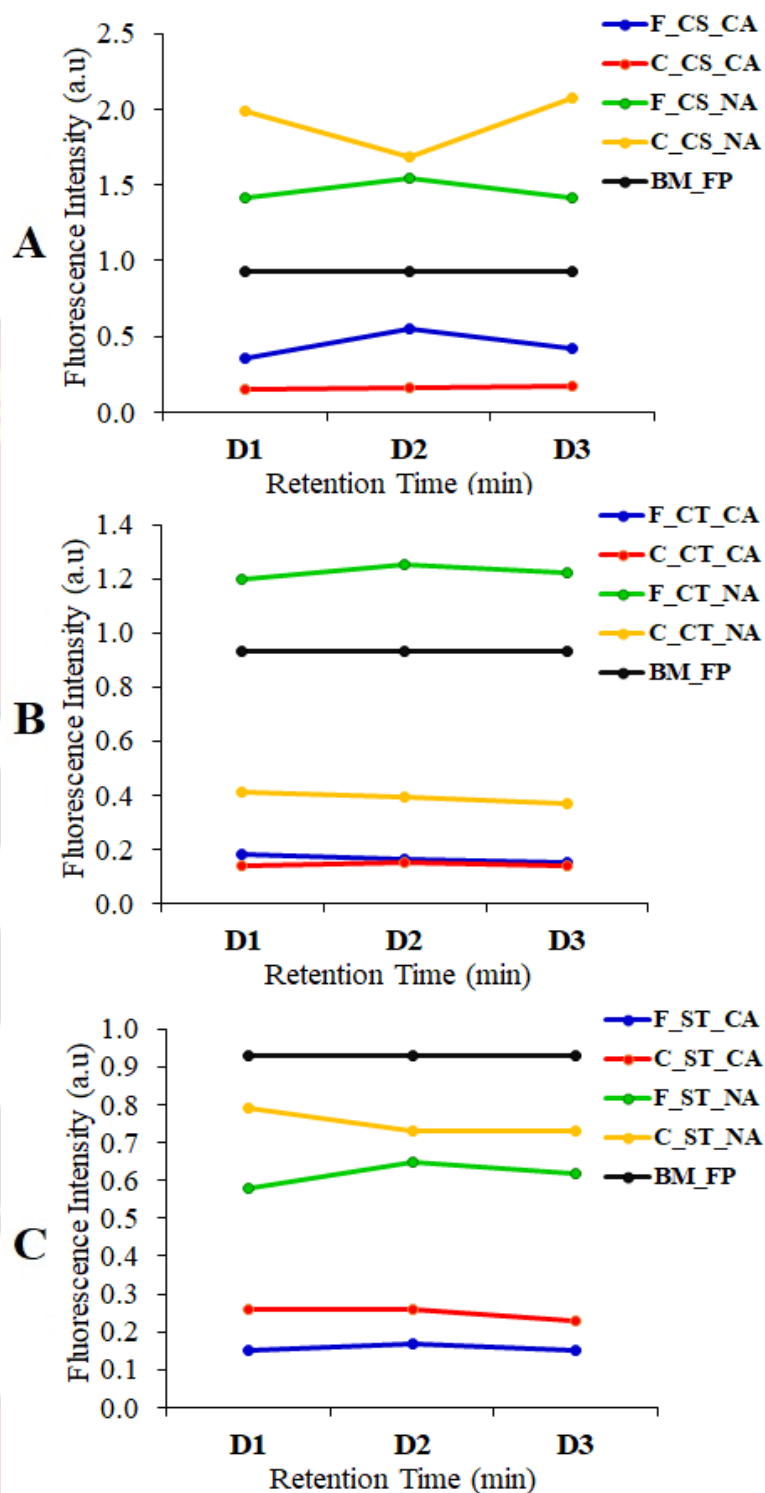


Figure 46: LIF peak intensities at 520 nm for samples filtered with 20 g of the furnace and conventionally carbonized (A) coconut shell, (B) cassia siamea tree branch, and (C) shea nut tree branch activated carbon adsorbents at 5(D1), 10(D2), and 15(D3) minutes retention times.

This contaminant removal performance was matched closely with C\_CS\_CA (82% minimum and 84% maximum) and F\_ST\_CA (82% minimum and 84% maximum). These were then followed closely by F\_CT\_CA (81% minimum and 84% maximum), C\_ST\_CA (72% minimum and 75% maximum), and F\_CS\_CA (41% minimum and 61% maximum).

The spectra for the 30 g adsorbent dose (Figures 47 and 48) revealed a slight shift in the trend of adsorbent performance, with F\_ST\_CA giving a minimum and maximum DOM removal efficiency of 86% and 87%, respectively. The next best-performing adsorbent for this dosage (30 g) was found to be F\_CT\_CA (86%), followed by C\_CT\_CA (84% minimum and 86% maximum), then C\_ST\_CA (75% minimum and 82% maximum), C\_CS\_CA (54% minimum and 59% maximum) and F\_CS\_CA (50% minimum and 58% maximum).

The observed difference in the trend of adsorbent performance for the different adsorbent doses (10 g, 20 g, and 30 g) may be attributed to the overlapping of adsorption sites caused by the increase in adsorbent mass or dosage (Ndi & Ketcha, 2013). The adsorbent performance was also observed to increase for most adsorbents in the first two retention or contact times (5 and 10 minutes) but decreased after the third retention time (15 minutes). This inconsistency may be due to the slow contaminant adsorption rate in the first 5 minutes, followed by a slightly rapid adsorption rate that diminishes as equilibrium is attained after 15 minutes (Ndi & Ketcha, 2013).

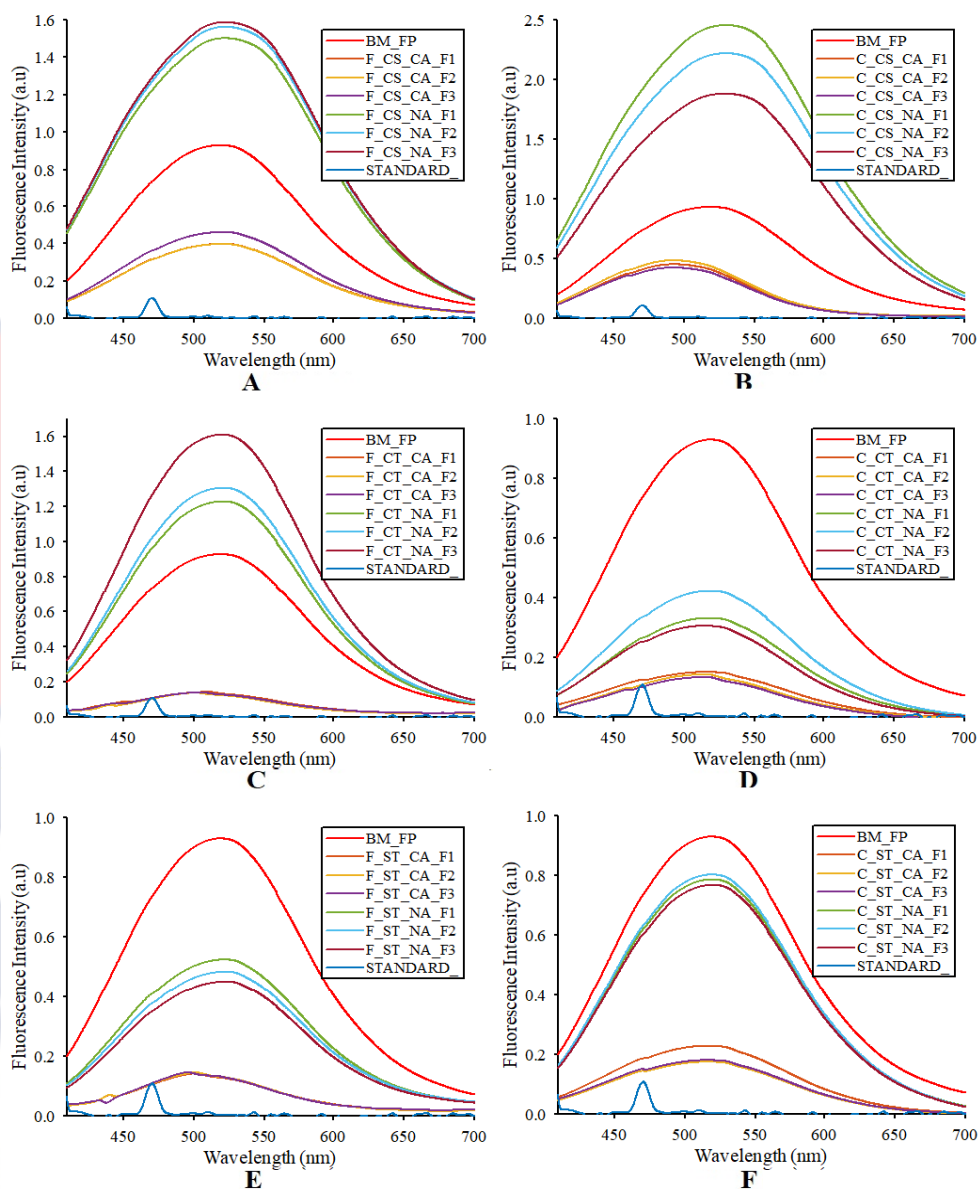


Figure 47: LIF spectra of all samples filtered with 30 g of the (A) furnace carbonized coconut shell, (B) conventionally carbonized coconut shell, (C) furnace carbonized cassia siamea tree branch, (D) conventionally carbonized cassia siamea tree branch, (E) furnace carbonized shea nut tree branch, and (F) conventionally carbonized shea nut tree branch activated carbon adsorbents

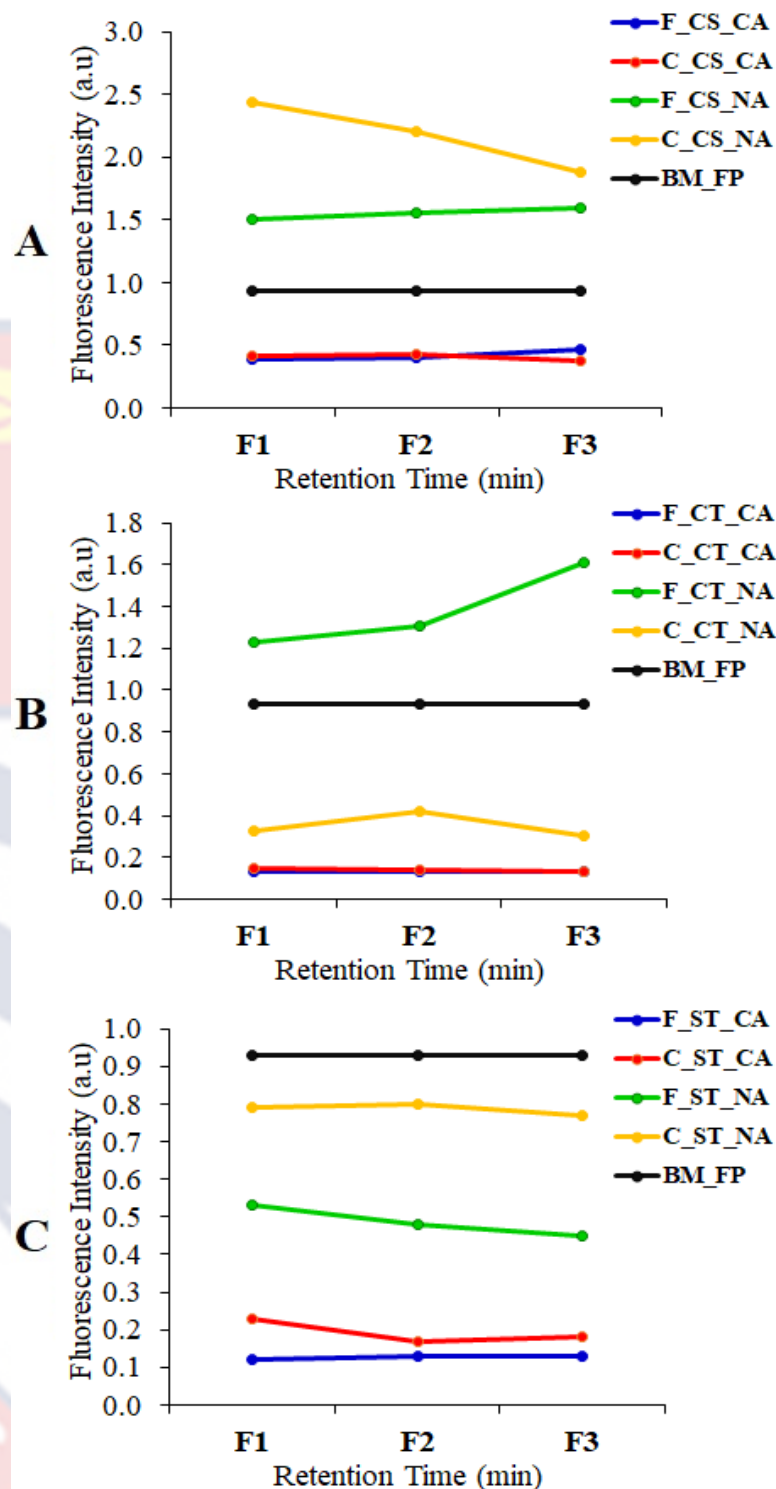


Figure 48: LIF peak intensities at 520 nm for samples filtered with 30 g of the furnace and conventionally carbonized (A) coconut shell, (B) cassia siamea tree branch, and (C) shea nut tree branch activated carbon adsorbents at 5(F1), 10(F2), and 15(F3) minutes retention times



The observations from the LIF emission spectra, as in Figures 43, 45, and 47, were visually illustrated using hierarchical clustering analysis (HCA). The HCA technique was employed to further determine the similarities or dissimilarities between the water samples filtered with the twelve prepared GAC adsorbents. The cluster trees from the cluster analysis categorized the different filtered and unfiltered samples based on their similarities to the standard sample clusters and their dissimilarities among the other categories. Figures 49 to 51 are clusters for CT\_CA and ST\_CA observed to relate very closely with the standard water sample, but with the CS\_CA clusters showing greater proximity to the standard.

The C\_CS\_CA samples showed an outstanding DOM removal efficiency for the 10 g adsorbent mass (Figure 49). Again, the hierarchical cluster analysis showed that the water samples filtered with the furnace and conventionally carbonized, CaCl<sub>2</sub>-activated adsorbents performed better in terms of DOM removal efficiencies. The wood-based GAC adsorbents depicted a low tanning effect, with both the CaCl<sub>2</sub>- and NaCl-activated adsorbents giving high DOM removal efficiencies.

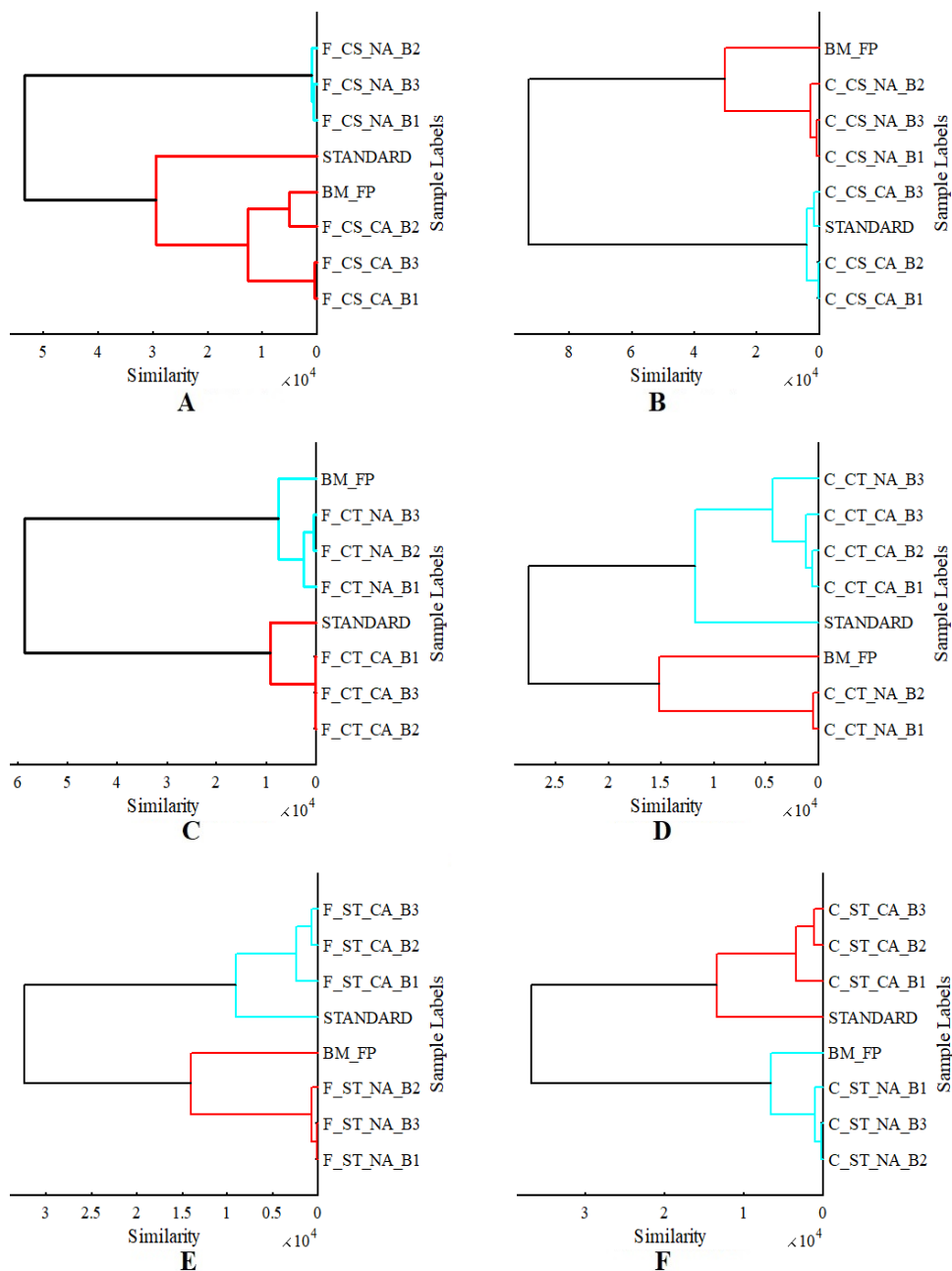
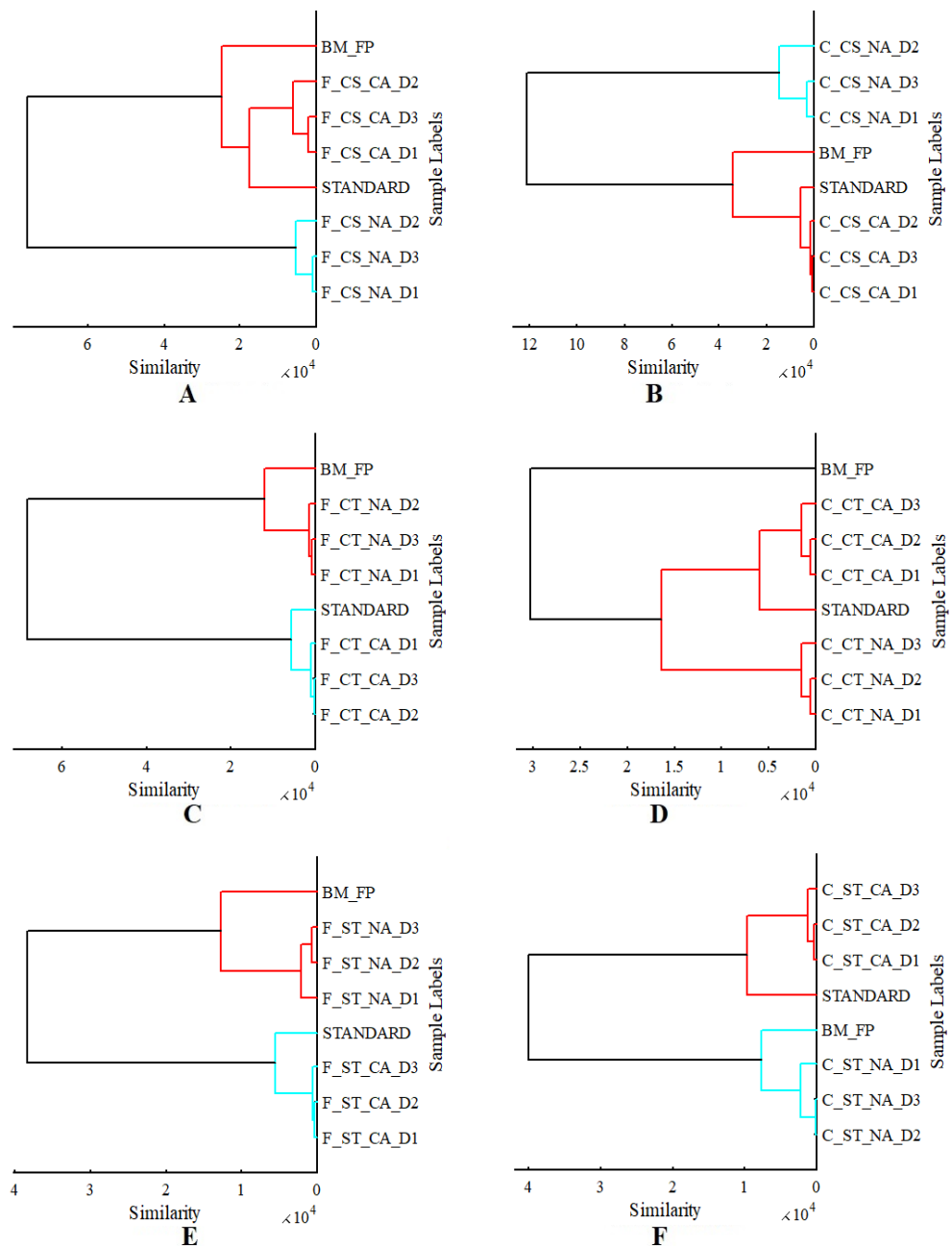
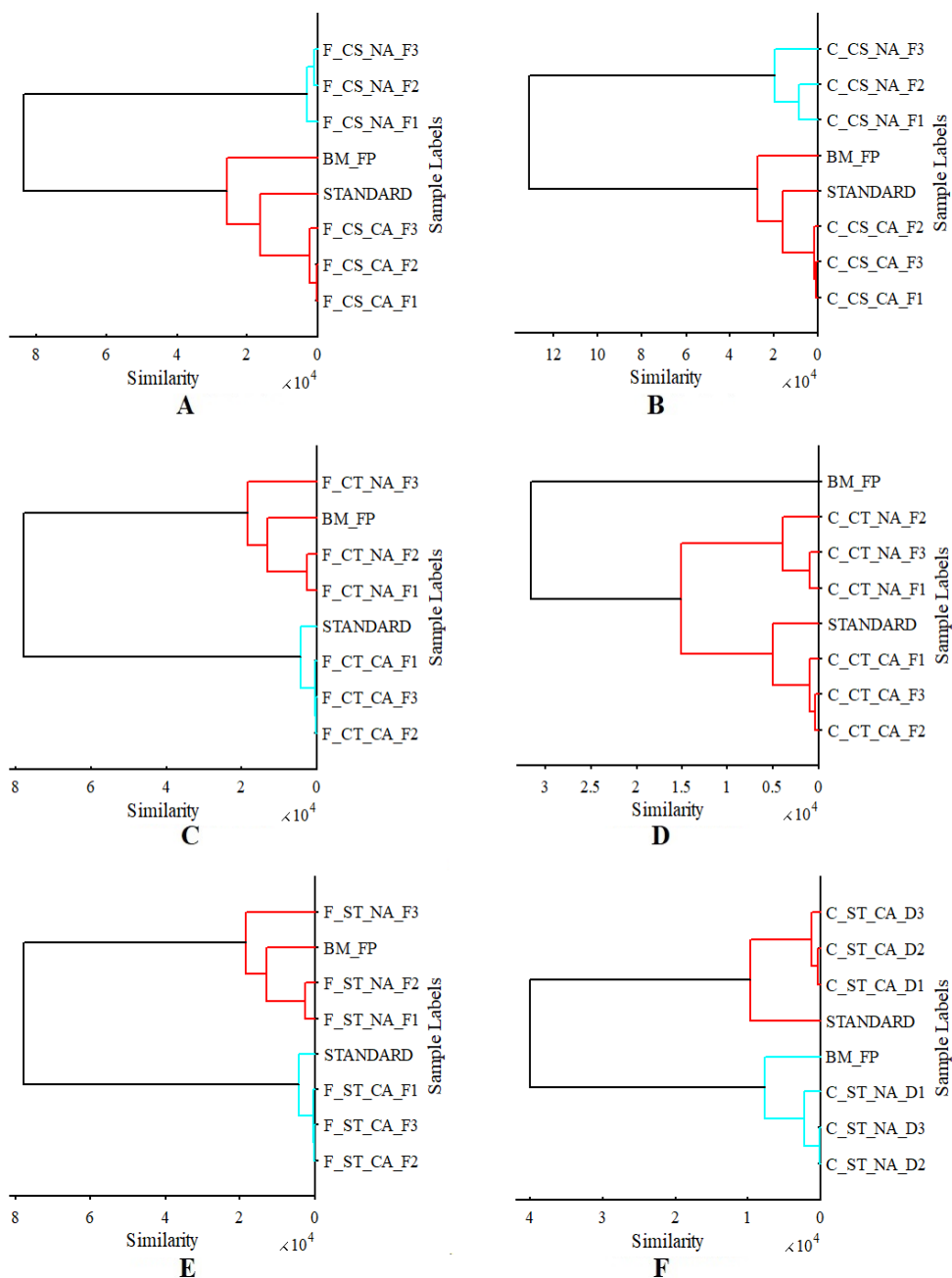


Figure 49: Cluster analysis based on ward method of normalized data for samples filtered with 10 g of the (A) furnace carbonized coconut shell, (B) conventionally carbonized coconut shell, (C) furnace carbonized cassia siamea tree branch, (D) conventionally carbonized cassia siamea tree branch, (E) furnace carbonized shea nut tree branch, and (F) conventionally carbonized shea nut tree branch activated carbon adsorbents



*Figure 50:* Cluster analysis based on ward method of normalized data for samples filtered with 20 g of the (A) furnace carbonized coconut shell, (B) conventionally carbonized coconut shell, (C) furnace carbonized cassia siamea tree branch, (D) conventionally carbonized cassia siamea tree branch, (E) furnace carbonized shea nut tree branch, and (F) conventionally carbonized shea nut tree branch activated carbon adsorbents



*Figure 51:* Cluster analysis based on ward method of normalized data for samples filtered with 30 g of the (A) furnace carbonized coconut shell, (B) conventionally carbonized coconut shell, (C) furnace carbonized cassia siamea tree branch, (D) conventionally carbonized cassia siamea tree branch, (E) furnace carbonized shea nut tree branch, and (F) conventionally carbonized shea nut tree branch activated carbon adsorbents

The observations from the LIF emission spectra, as in Figures 43, 45, and 47, were again visually illustrated using principal component analysis (PCA). The plot of the eigenvalues generated from the PCA algorithm, known as the scree plot, was made for the first 3 PCs, as shown in Figure 52.

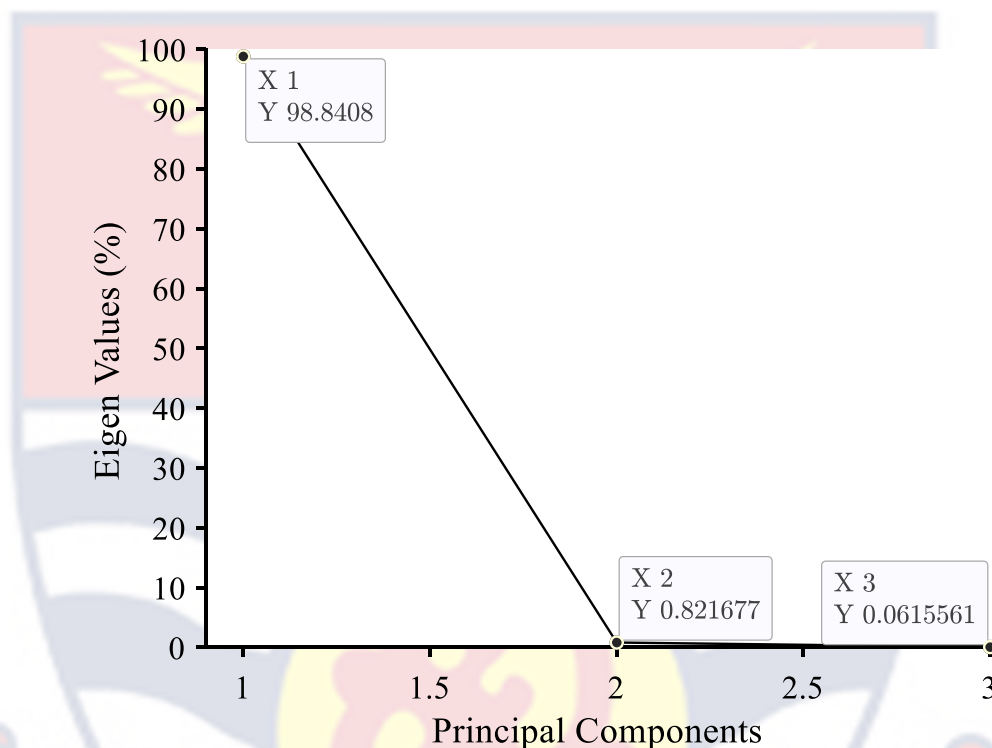


Figure 52: Scree plot of the eigenvalues of the principal components for the LIF spectra

From the scree plot, a steady drop in the eigenvalues was observed from the first principal component (PC1) to the second principal component (PC2) and then the third principal component (PC3). Hence, the first three PCs, which showed a higher combined percentage variability of over 99.7 %, were used due to their ability to retain the maximum variance of the filtered and unfiltered water samples.

The 3-dimensional score plots for all water samples filtered with 10g, 20 g, and 30 g of all prepared GAC adsorbents are shown in Figures 53 to 55. Each score plot for the filtered and unfiltered water samples showed four



distinct clusters, with all  $\text{CaCl}_2$ -activated adsorbent filtered samples which are comparable to the standard water sample than those filtered with the  $\text{NaCl}$ -activated adsorbents (Figure 53 to 55), as seen in the LIF spectra (Figures 43, 45, and 47).

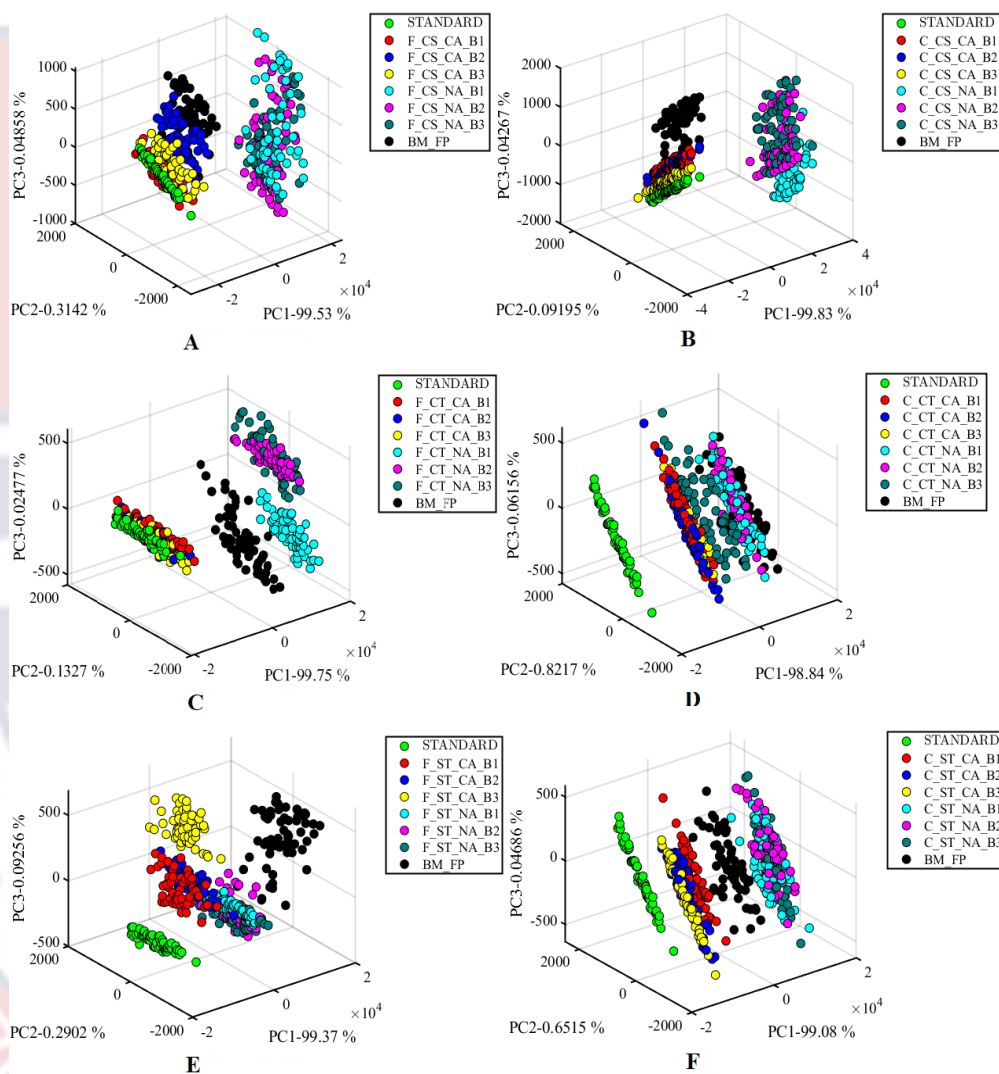


Figure 53: Score plots for samples filtered with 10 g of the (A) furnace carbonized coconut shell, (B) conventionally carbonized coconut shell, (C) furnace carbonized cassia siamea tree branch, (D) conventionally carbonized cassia siamea tree branch, (E) furnace carbonized shea nut tree branch, and (F) conventionally carbonized shea nut tree branch activated carbon adsorbents

The cluster of samples filtered with the furnace and conventionally carbonized shea nut tree branch GAC adsorbents (F\_ST and C\_ST) illustrated a successful reduction in the DOM fluorescence in all filtered water samples, with all clusters closer to the standard and away from the unfiltered water sample (BM\_FP). This observation was also realised with the conventionally carbonized cassia siamea tree branch (C\_CT) GAC-filtered samples.

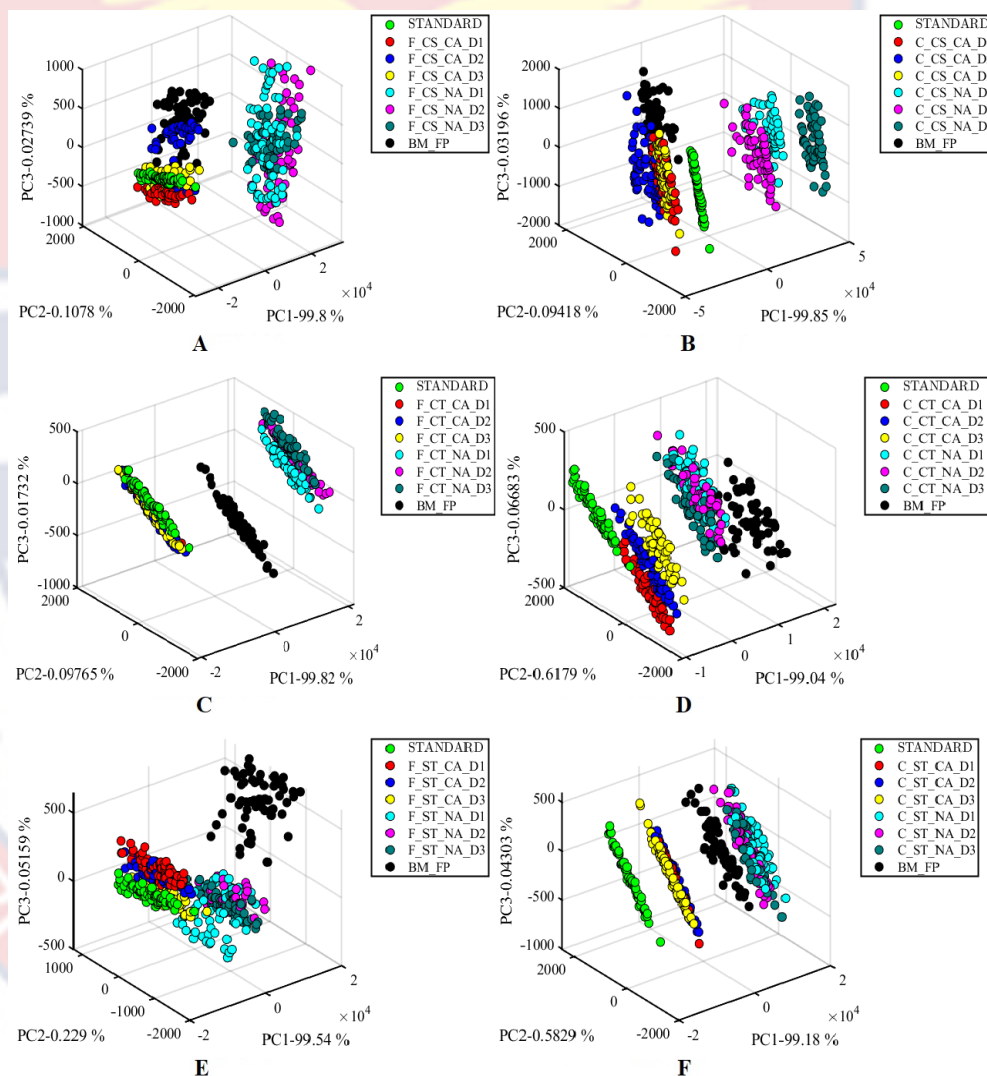


Figure 54: Score plots for samples filtered with 20 g of the (A) furnace carbonized coconut shell, (B) conventionally carbonized coconut shell, (C) furnace carbonized cassia siamea tree branch, (D) conventionally carbonized cassia siamea tree branch, (E) furnace carbonized shea nut tree branch, and (F) conventionally carbonized shea nut tree branch activated carbon adsorbents

However, the samples filtered with NaCl-activated GAC adsorbents showed an increase in DOM fluorescence, as observed in the other spectroscopic techniques, except C\_CT, F\_CT and F\_ST, as shown in Figures 53 and 55.

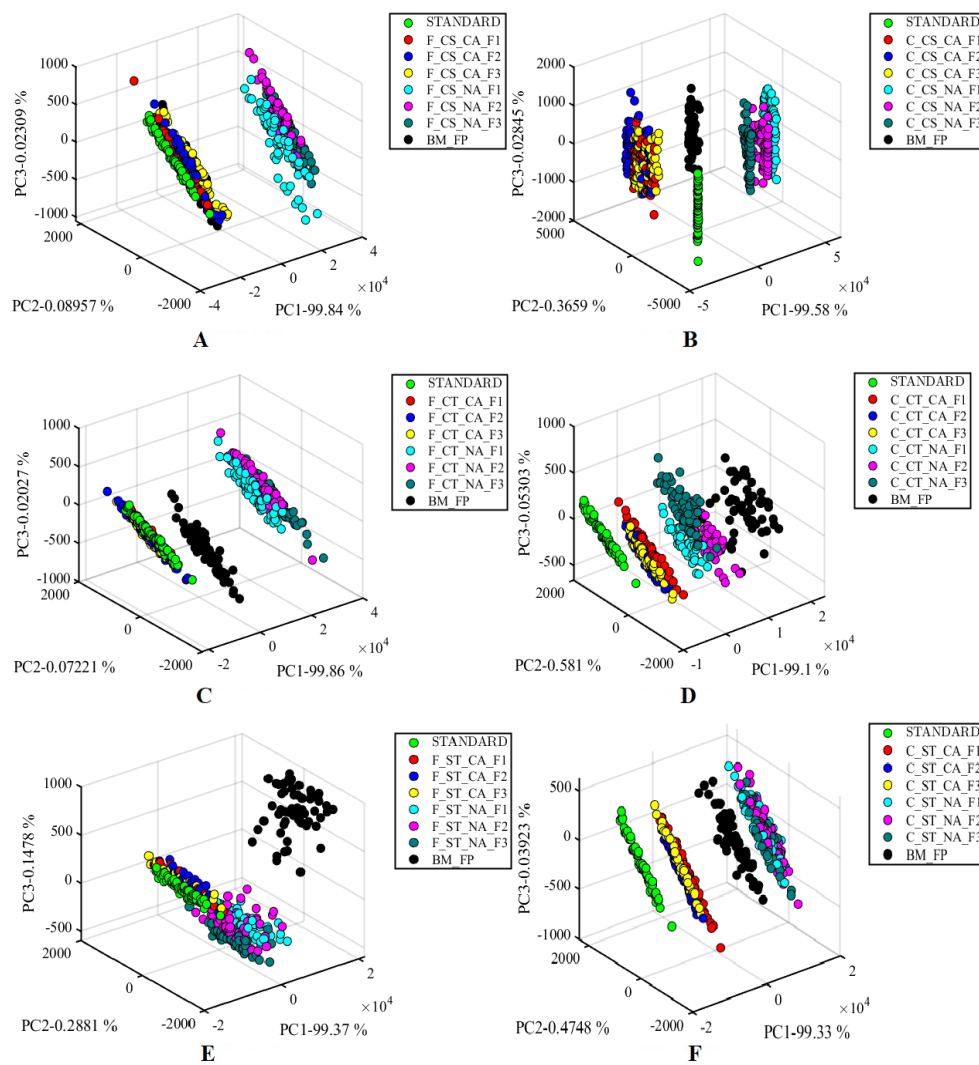


Figure 55: Score plots for samples filtered with 30 g of the (A) furnace carbonized coconut shell, (B) conventionally carbonized coconut shell, (C) furnace carbonized cassia siamea tree branch, (D) conventionally carbonized cassia siamea tree branch, (E) furnace carbonized shea nut tree branch, and (F) conventionally carbonized shea nut tree branch activated carbon adsorbents

In a similar study by Moona (2021), this increase in DOM fluorescence may be attributed to the bleaching effects of the NaCl and the inability of the activation chemical to reduce the general tanning effect of charcoal (Moona, 2021).

F\_CT\_CA\_F filtered samples were also observed to be the closest cluster to the standard sample, indicating a higher reduction (96 %) in DOM fluorescence intensity (Figure 55). A generally high DOM fluorescence intensity reduction was observed for all CaCl<sub>2</sub> AC filtered samples, especially for the cassia siamea and shea nut tree GAC samples for all adsorbent masses and retention times. This reduction in DOM fluorescence intensity by the prepared GAC adsorbents indicates a corresponding reduction in the humic component of DOM, hence a reduction in the DBPs formation rates during chlorination.

The similarity and or dissimilarity between the filtered and unfiltered samples were further elaborated using the Euclidean distance between the clusters and categories (Figures 56 to 58). The Euclidean distances from a singly distilled standard water sample at 0.00 a.u were taken against all samples filtered with the different masses of the furnace and conventionally carbonized GAC adsorbents at varying retention times, and in 2-dimensions using K-nearest neighbour (K-NN) test in the water quality classification (Sefa-Ntiri et al., 2020).

The score plots and cluster analysis again showcased similar DOM removal efficiency trends. With C\_CS\_CA\_B3 (0.02 a.u) having the highest proximity to the standard water sample, followed by C\_CS\_CA\_B1 and C\_CS\_CA\_B2 which were 0.04 a.u away from the standard, for the samples filtered with 10 g of each GAC adsorbent (Figure 56).

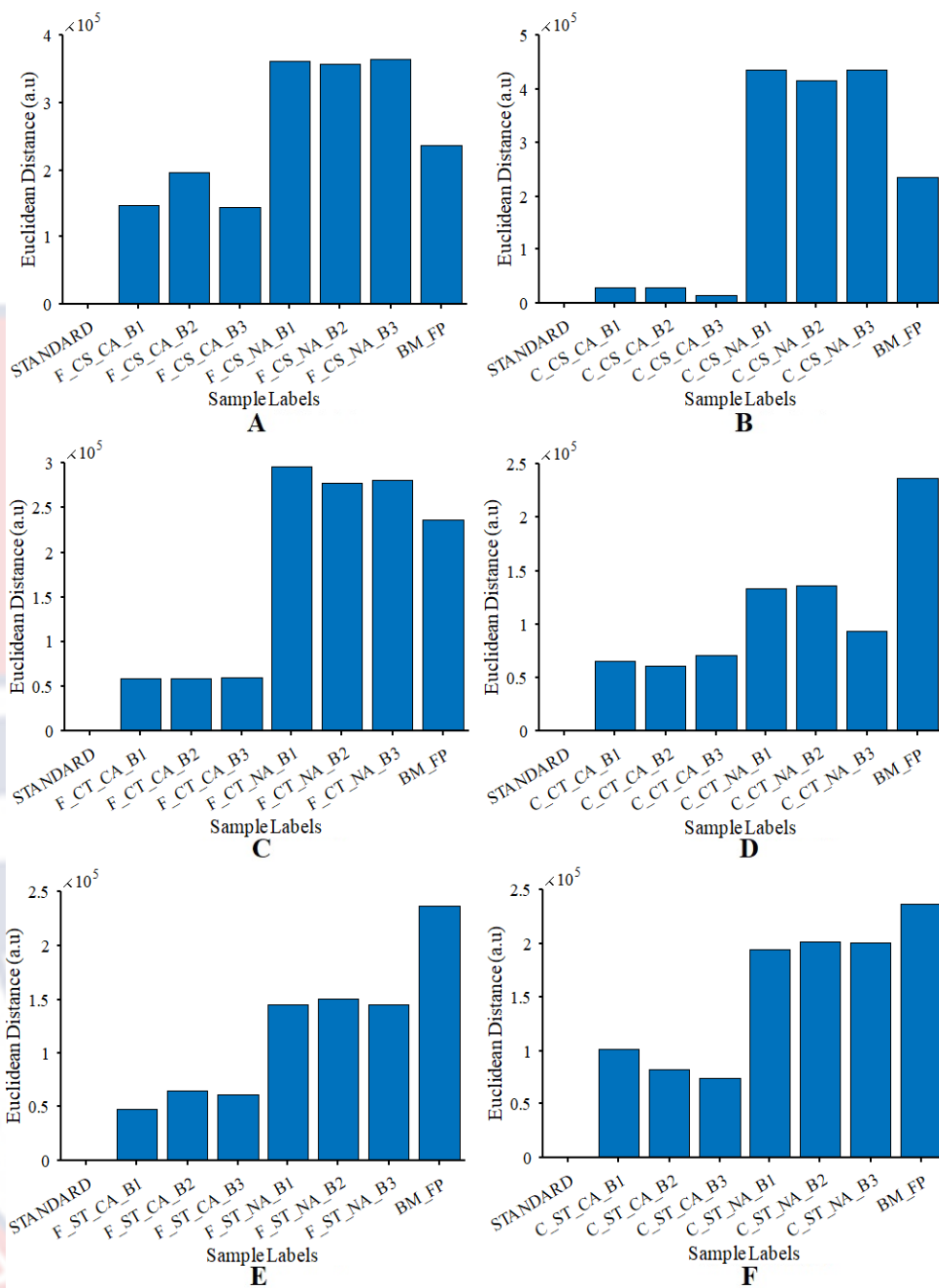


Figure 56: Euclidean distances from the standard water sample to all samples filtered with 10 g of the (A) furnace carbonized coconut shell, (B) conventionally carbonized coconut shell, (C) furnace carbonized cassia siamea tree branch, (D) conventionally carbonized cassia siamea tree branch, (E) furnace carbonized shea nut tree branch, and (F) conventionally carbonized shea nut tree branch activated carbon adsorbents



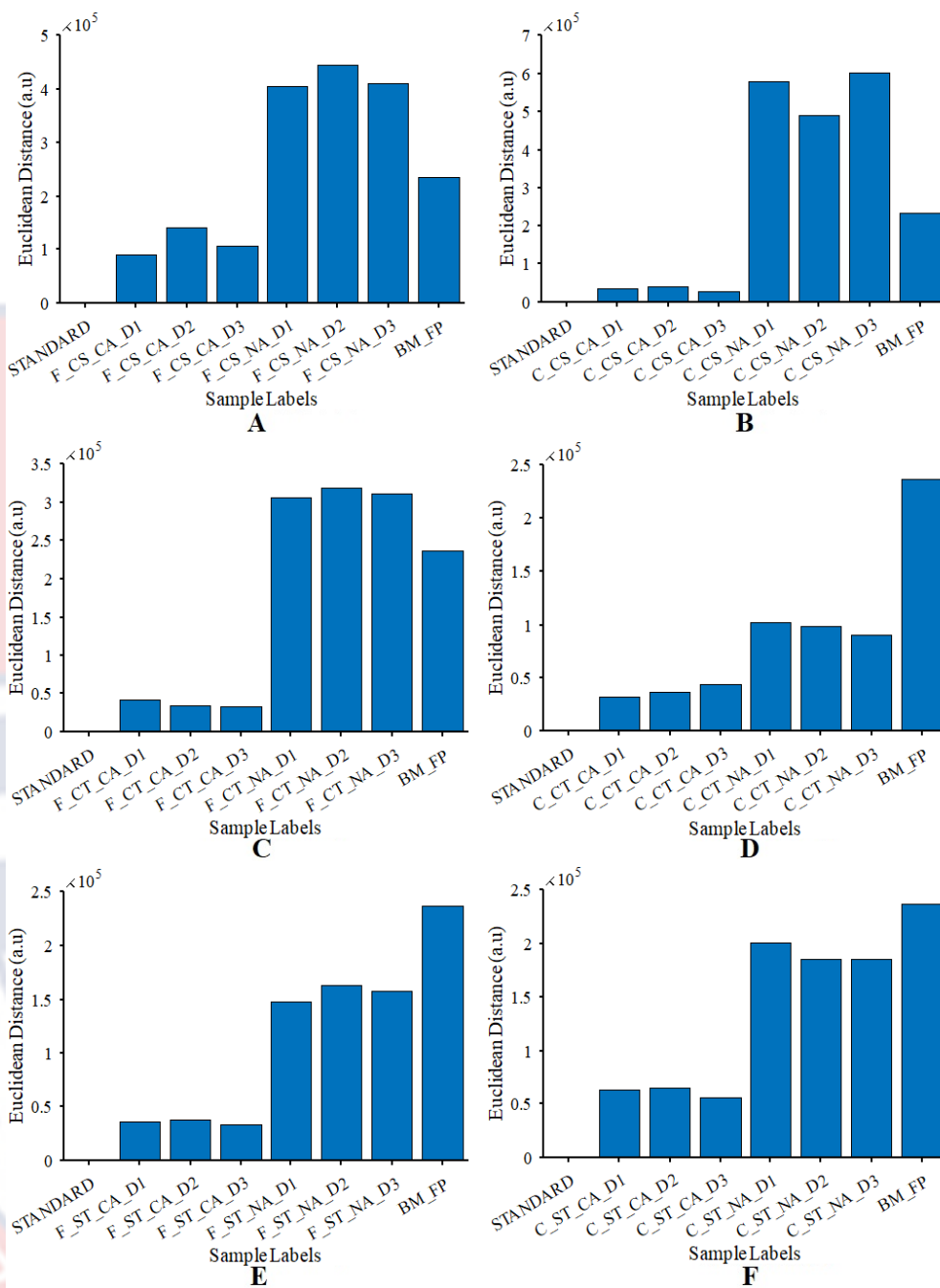


Figure 57: Euclidean distances from the standard water sample to all samples filtered with 20 g of the (A) furnace carbonized coconut shell, (B) conventionally carbonized coconut shell, (C) furnace carbonized cassia siamea tree branch, (D) conventionally carbonized cassia siamea tree branch, (E) furnace carbonized shea nut tree branch, and (F) conventionally carbonized shea nut tree activated carbon adsorbents

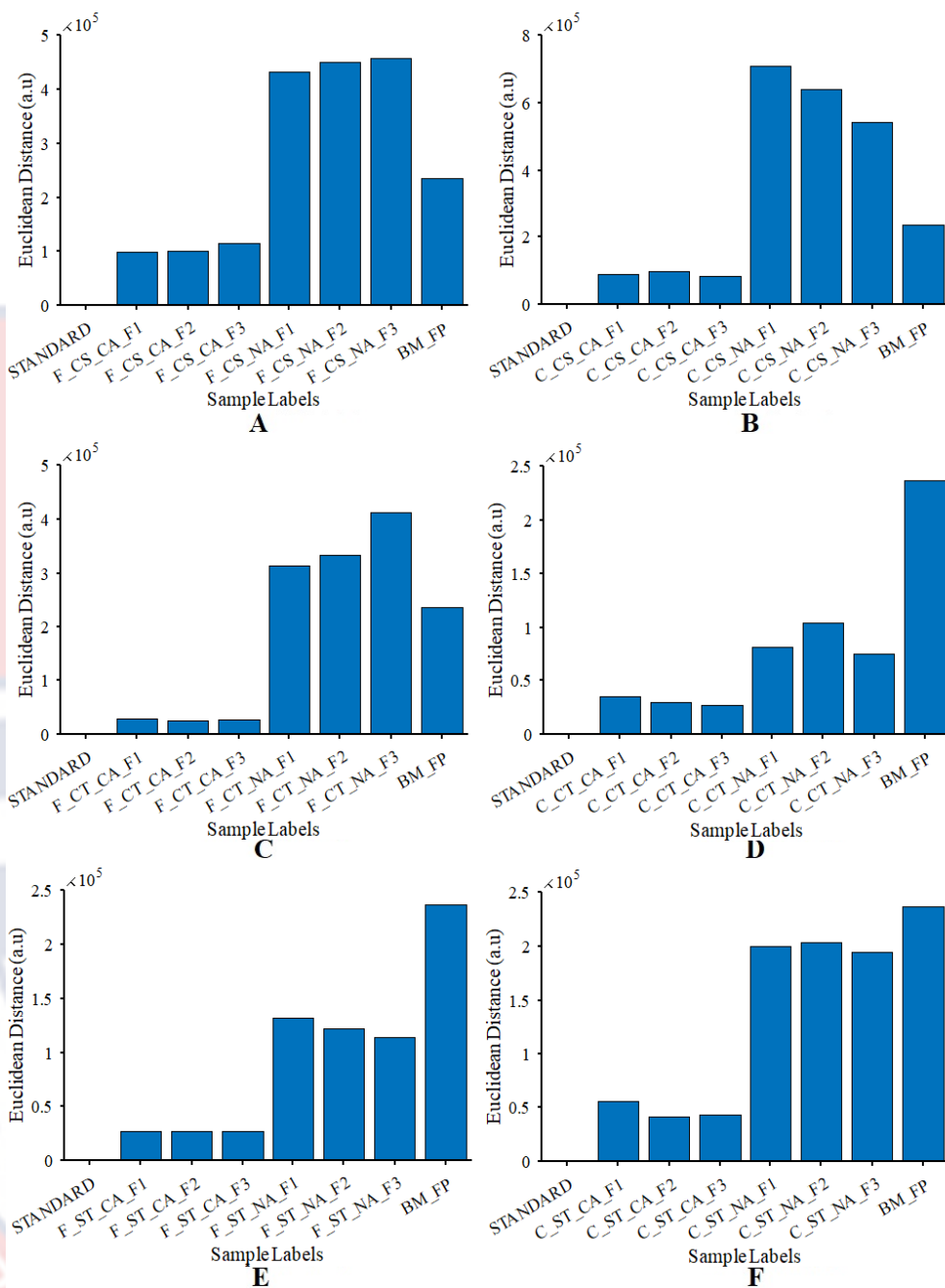


Figure 58: Euclidean distances from the standard water sample to all samples filtered with 30 g of the (A) furnace carbonized coconut shell, (B) conventionally carbonized coconut shell, (C) furnace carbonized cassia siamea tree branch, (D) conventionally carbonized cassia siamea tree branch, (E) furnace carbonized shea nut tree branch, and (F) conventionally carbonized shea nut tree branch activated carbon adsorbents

For the samples filtered with 20 g of the GAC adsorbent, Figure 57 shows a high proximity to the standard water sample as again observed for C\_CS\_CA\_D3 (0.03 a.u), followed by C\_CS\_CA\_D1 (0.035 a.u) and C\_CS\_CA\_D2 (0.04 a.u). This trend was however, broken for samples filtered with 30 g of each GAC adsorbent (Figure 58), with F\_CT\_CA\_F2 (0.038 a.u) and F\_CT\_CA\_F3 (0.039 a.u) having the highest proximity to the standard water sample, which was followed immediately by F\_CT\_CA\_F1 (0.04 a.u).

### Polarized Light Microscopy

The intensity plot of the polarized light images (Appendix C), for all samples filtered with 30 g of the CaCl<sub>2</sub>- and NaCl- activated adsorbents; F\_CS, C\_CS, F\_CT, C\_CT, F\_ST, and C\_ST, is shown in Figure 59 for a polarization angle of 90°. As observed in the other spectroscopic techniques, the samples filtered with CaCl<sub>2</sub>-activated adsorbents gave higher polarized image intensities compared to those filtered with NaCl-activated adsorbents.

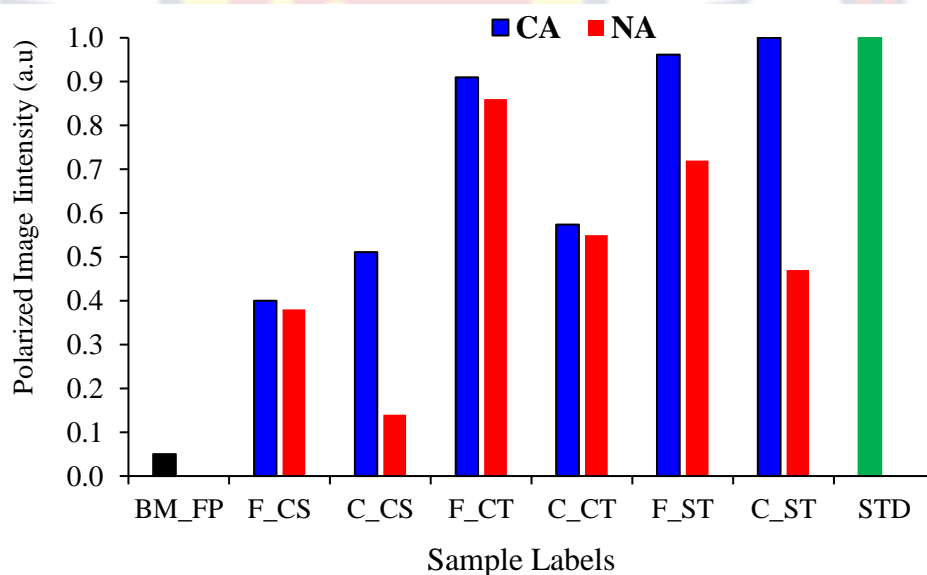


Figure 59: Polarized light intensity plot of all samples filtered with 30 g of the CaCl<sub>2</sub>-activated adsorbents

The performance trends were also observed to be similar to the results of the LED-IT spectroscopy, with C\_ST\_CA\_F3, F\_ST\_CA\_F3, F\_CT\_CA\_F3, and C\_CT\_CA\_F3 exhibiting similar image intensities as the standard (STD) water sample. The results from this study depict the optical turbidity of the water samples, which is why the performance trends under this technique relate to those under the LED-induced transmittance technique. The LEGO-based polarization imaging system for water quality analysis is a novel and cost-effective approach to discriminate filtered and unfiltered water samples. The results obtained using this technique demonstrated its accuracy as a good surrogate in assessing the efficiency of the prepared GAC adsorbents in DOM and turbidity treatment.

#### Average Adsorption Capacity of Prepared GAC Adsorbents

The averaged DOM removal efficiency for the different adsorbent doses was plotted for the two activating agents (chemicals), as shown in Figure 60.

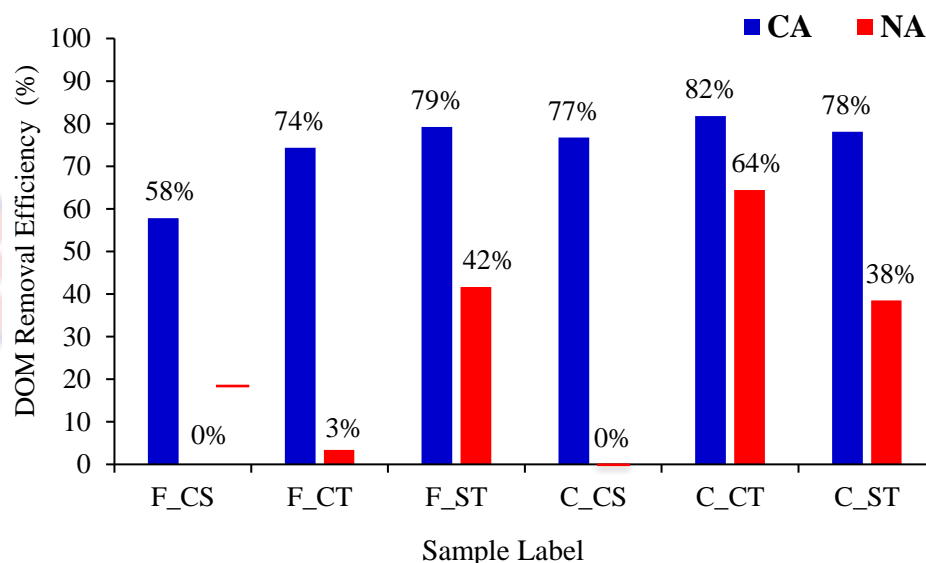


Figure 60: DOM removal efficiency for samples filtered with CaCl<sub>2</sub>- and NaCl- activated carbon adsorbents

The bar graph expounded the good performance of the samples filtered with  $\text{CaCl}_2$ -activated adsorbents against those filtered with  $\text{NaCl}$ -activated carbon adsorbents. This was further elaborated by the bar plot in Figure 61, establishing the good performance of all the  $\text{CaCl}_2$ -activated adsorbents with an average DOM removal efficiency of 75 %, against the  $\text{NaCl}$ -activated adsorbents with an average DOM removal efficiency of 25 % (Figure 61).

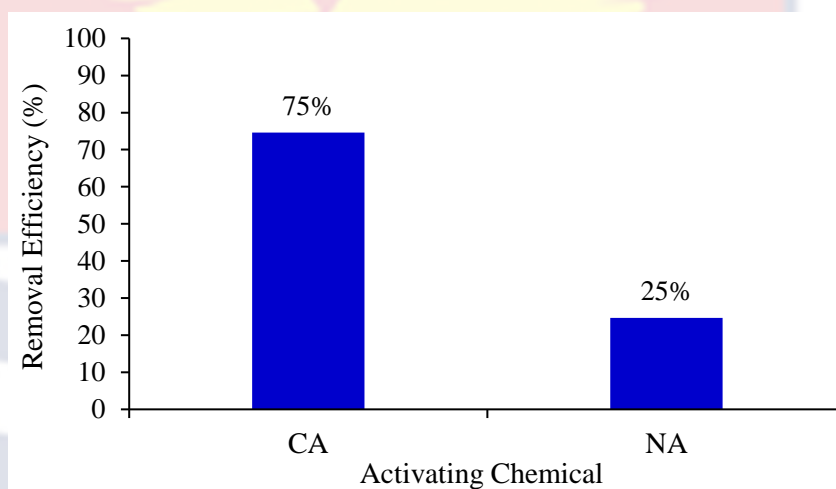


Figure 61: DOM removal efficiency for the different activating chemicals

However, despite the generally good performance of the  $\text{CaCl}_2$ -activated adsorbent, C\_CT\_CA (82%) emerged with an averagely high absorbance removal efficiency. This performance was matched up closely by F\_ST\_CA (79 %) and C\_ST\_CA (78 %), followed by C\_CS\_CA (77 %), F\_CT\_CA (74 %), C\_CT\_NA (64 %), and F\_CS\_CA (58 %), with the rest of the  $\text{NaCl}$ -activated carbon adsorbent filtered samples giving efficiencies below 50 %.

Samples F\_CS\_NA and C\_CS\_NA however, gave 0 % DOM removal efficiency due to the raw material and activating chemical used. Moreover, although C\_CT\_NA (64 %) is a  $\text{NaCl}$ -activated adsorbent, it performed slightly better than the  $\text{CaCl}_2$ -activated adsorbent, F\_CS\_CA (58 %). Based on this



observation, it could be concluded that, aside from the activating chemical, the adsorbent capacity or efficiency also depends on the type of raw water used. But on average, the results showed the good performance of the  $\text{CaCl}_2$ -activated adsorbents compared to the  $\text{NaCl}$ -activated adsorbents as observed by other researchers (Cobb, Warms, Maurer, & Chiesa, 2012; Zanella, Tessaro, & F  ris, 2014).

### COMSOL Multiphysics Simulation

The post-processing results from the free and porous media flow interface, coupled with the transport of diluted species interface, are shown in Figures 62 to 65. The surface and contour velocity profiles (Figure 62) showed higher fluid flow velocity at the filter's centre, which decreased and approached zero at the walls. This observation of decreasing fluid velocity toward the walls exhibited a no-slip boundary condition at the walls of the filter, with most water directed toward the filter's centre. The high flow rate towards the centre may be attributed to the inlet's narrow diameter (6 cm) compared to the inner diameter (7 cm). This difference between the inlet and inner diameter also led to a slightly lower flow velocity towards the walls of the filter column.

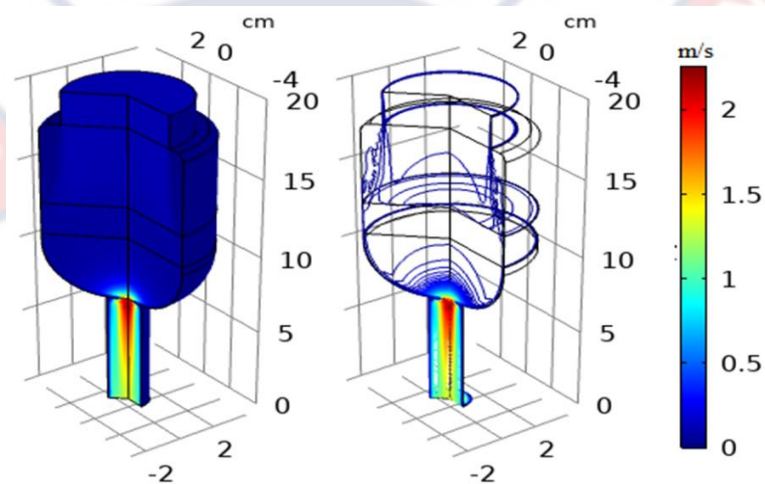


Figure 62: (A) Surface plot and (B) Contour plot of the velocity profile of water flow through the designed filter

However, as the water enters the funnel section, there was a sharp increase in flow velocity due to the change in diameter (7 cm to 2 cm). This change in diameter caused a slightly turbulent flow from the funnel neck to the outlet. The increase in velocity with decreasing diameter is also shown mathematically in the flow rate equation shown in equation (22). The flow rate equation exhibited the inverse relation between the flow velocity and the cross-sectional area (equation 22), where  $v$  is the magnitude of the flow velocity,  $Q$  is the flow rate, and  $A$  is the column's cross-sectional area.

$$v = \frac{Q}{A} \quad (22)$$

The velocity change showed the porosity difference as water moved from the adsorbent to the PU foam, as illustrated by the line plot in Figure 63. A sharp decrease in flow velocity from the top of the funnel through the funnel neck (2 m/s) towards the outlet (1.3 m/s), may be attributed to the change in porosity and diameter. This sharp change in diameter forced the water to flow towards the filter's centre with an increase in velocity due to the decrease in area.

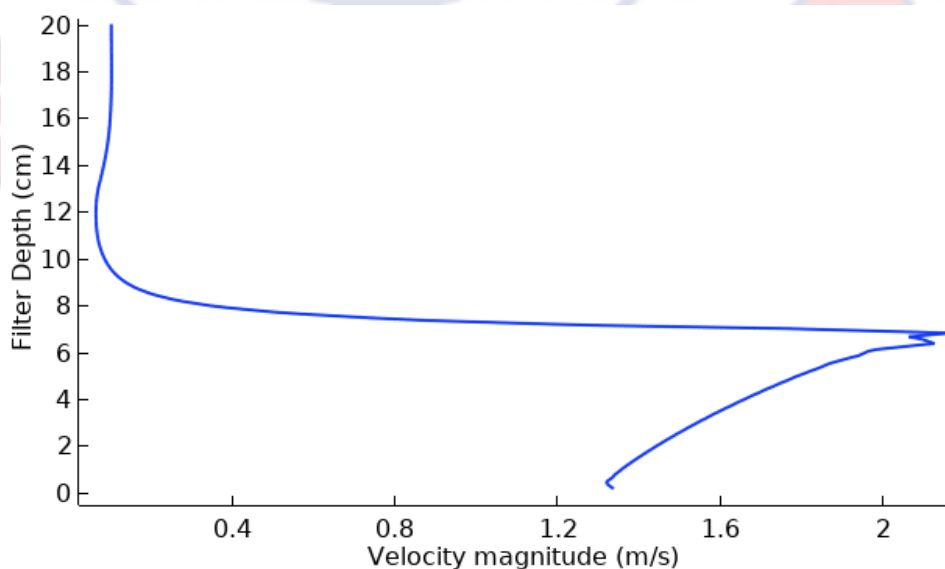


Figure 63: Line plot of the velocity profile of water flow through the filter

The contour plot of the pressure profile of water flow through the designed filter also showed the change in pressure as water entered the free column and passed through the AC adsorbent. This observation illustrates that water flowing under gravity moves from high to low-pressure regions (Figure 64).

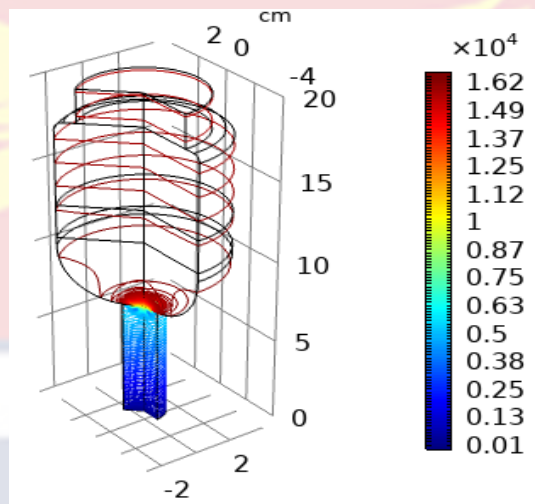
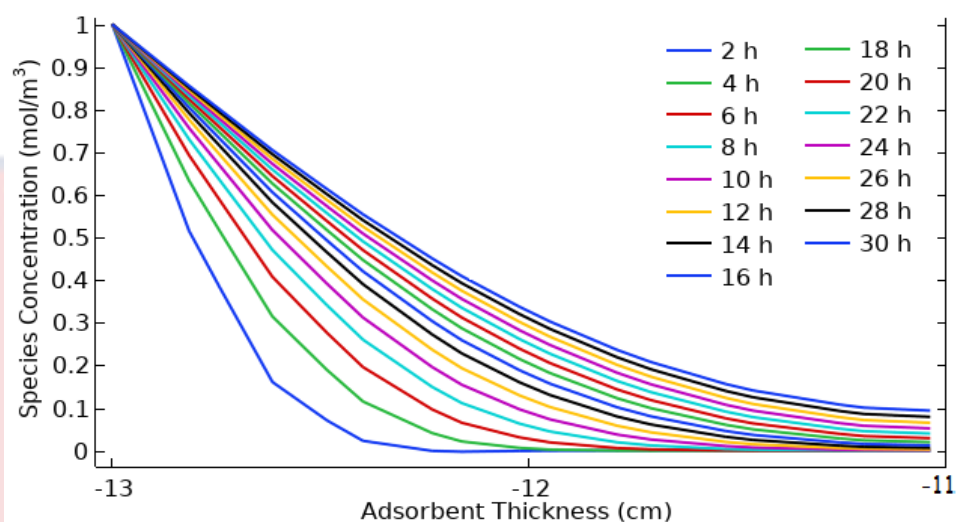


Figure 64: Contour plot of the pressure profile of water flow through the filter

Results from the transport of diluted species interface of the coupled study (Free and porous media flow coupled with the transport of diluted species) also illustrated a decrease in water contaminant concentration as it passes through the GAC adsorbent section. This decrease in contaminant concentration was due to the adsorption of contaminants by the porous adsorbent as it stays in contact with the water. The results from this simulation also showed that the adsorption rate decreases with time. That is, the adsorption sites get used up with time, thus, giving way for some contaminants to escape into the permeate after a certain threshold of time (Kim et al., 2019).

The line plot in Figure 65 showed the change in permeate concentration with time, indicating how long a GAC adsorbent of 2 cm thickness can be used for 100 % adsorption. From Figure 65, the permeate concentration increased

significantly after 30 hours of filtration, with  $0.1 \text{ mol/m}^3$  (10 %) of contaminants escaping into the permeate.



*Figure 65: Change in species concentration with adsorbent thickness for 30 hours*

However, as the adsorbent thickness increased from 2 cm to 4 cm, a significant increase in permeate concentration ( $> 10\%$ ) was only observed on the 5<sup>th</sup> day (120 hours) of filtration (Figure 66). This observation indicates a 90% contaminant removal efficiency for the prescribed AC adsorbent (Filter diameter = 8 cm, Adsorbent thickness = 4 cm, porosity = 0.3). The increase in the adsorbent lifetime (30 hrs to 120 hrs) as the adsorbent thickness and mass increased was again observed in the experimental results.

The transport of diluted species interface in COMSOL Multiphysics was, therefore, successfully used to demonstrate the transport of some contaminant species in a dead-end fluid flow through a prescribed GAC adsorbent. The rate of contaminant removal by adsorption and the adsorbent lifetime was also observed to depend on the adsorbent thickness and hence, the mass. The results of this simulation are also significant in improving filter



efficiency by informing the optimization of filter design parameters for future applications (Kim et al., 2019).

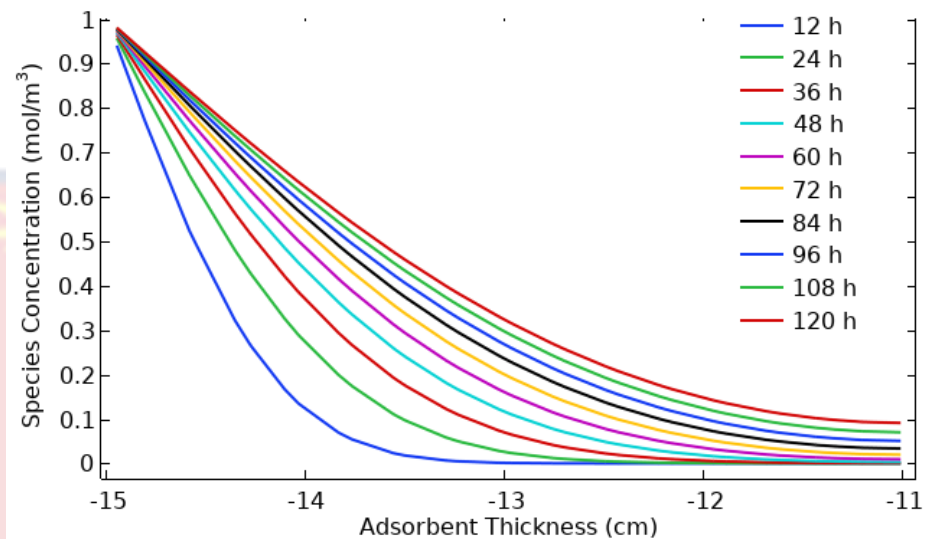


Figure 66: Change in concentration with adsorbent thickness for 120 hours

### Chapter Summary

The chapter has presented and discussed results from the six (6) optical spectroscopic techniques used in characterising and assessing DOM removal efficiency of some prepared GAC adsorbents. The flow regime and adsorbent behaviour of the modelled filtration system were mimicked in the COMSOL Multiphysics simulations and the results were discussed. PCA and some hierarchical clustering techniques were employed to further discriminate between water samples filtered with the differently prepared adsorbents. The simulation results informed the structure and the flow mechanics of the designed filtration system. The physiochemical and spectroscopic results also showed the DOM removal capacities of the prepared GAC adsorbents. The effect of the chemical activation agents, proved the highly efficient DOM removal capability (75%) of the CaCl<sub>2</sub>-activated adsorbents, against that of the NaCl-activated adsorbents (25%).



## CHAPTER FIVE

### SUMMARY, CONCLUSIONS, AND RECOMMENDATIONS

#### Overview

This study sought to assess the general characteristic and dissolved organic matter removal performance of twelve (12) prepared granular activated carbon GAC adsorbents to address the challenge of safe water scarcity. The adsorbents were characterised using spectroscopic techniques and tested using a surface water sample at different retention times (5 minutes, 10 minutes, and 15 minutes) and adsorbent masses (10 g, 20 g, and 30 g). The effect of the chemical activating agents on the DOM removal performance was assessed using spectroscopic techniques, assisted by COMSOL Multiphysics simulations. In this chapter, the summary, conclusions, and recommendations for future studies have been presented.

#### Summary

A surface water sample from river Brimsu was used as the primary raw water sample in testing DOM removal efficiency of prepared GAC adsorbents, the effect of the activation processes on some physicochemical properties of the water sample. The general characteristics and DOM removal efficiencies of twelve (12) GAC adsorbents prepared from coconut shell, cassia siamea, and shea nut tree branch samples, were evaluated using six spectroscopic techniques, vis-à-vis, X-ray diffraction spectroscopy (XRD), Fourier transform infrared spectroscopy (FTIR), UV-Visible absorbance, LED induced transmission spectroscopy (LED-IT), Laser induced fluorescence (LIF) and polarized light microscopy. The LIF data obtained were further analysed using

some multivariate data analysis techniques such as cluster analysis (CA) and principal component analysis (PCA). The study was assisted with the use of COMSOL Multiphysics simulation which has thrown light on the filtration system, the fluid flow dynamics, and the transport of diluted species in the modelled adsorbent bed. The main limitation of this study is the interference of some compounds (chromium, nitrite, sodium nitrate, sodium sulphate, sodium phosphate, chloride, etcetera) in the raw water with the spectral analysis. These, however, do not mean the analysis is inaccurate.

### **Conclusions**

This study prepared and characterized twelve (12) GAC adsorbents; F\_CS\_CA, F\_CS\_NA, C\_CS\_CA, C\_CS\_NA, F\_CT\_CA, F\_CT\_NA, C\_CT\_CA, C\_CT\_NA, F\_ST\_CA, F\_ST\_NA, C\_ST\_CA and C\_ST\_NA, using XRD and FTIR. These spectroscopic techniques showcased the elemental composition of the prepared GAC adsorbents as well as the molecular arrangements and bonds present. The two characterization techniques used complimented each other in the efficient characterization of the GAC adsorbents.

The study also evaluated the DOM removal efficiency of the twelve prepared GAC adsorbents in a surface water sample using four other spectroscopic techniques; absorbance, transmission, fluorescence, and polarized light imaging. This was achieved by comparing the concentration in the filtered water samples to the unfiltered water samples. The DOM removal efficiency of the adsorbents was successfully demonstrated, and the results indicated the close matching capabilities of the GAC adsorbents prepared from the three different agricultural by-products. The cassia siamea tree and the shea

nut tree branch AC adsorbents, were highly efficient (80 % to 100 %) in removing DOM from the surface water sample, compared to the coconut shell GAC adsorbent. All the spectroscopic techniques proved useful in DOM characterization. The polarized light imaging technique was also successfully used in water quality assessment for the first time with a polarization angle of 90 degrees showing a good distinction between water samples.

The effect of the chemical activating agents on the DOM removal performance of the GAC adsorbents was also established. Compared to its NaCl counterpart, a generally high DOM removal efficiency (75 %) was observed for all CaCl<sub>2</sub>-activated adsorbents in the results from all the spectroscopic techniques used in characterizing the DOM in each sample. The unique performance of these prepared GAC adsorbents was seen in their elemental and molecular nature as outlined by the XRD and FTIR results.

In general, the effect of the different adsorbent masses and retention times were not prominent. The study has also successfully shown a novel solution to upgrading the rapid sand filtration technique used in most centralized water purification and distribution systems, as an efficient point-of-use water purification technique. This novel solution to safe water scarcity was achieved by establishing the DOM removal capabilities of GAC adsorbents prepared from different agricultural by-products. The simulation results also proved the workability of the proposed filter design as a stand-alone point-of-use water filtration system. The study again revealed that wood samples could be an excellent raw material for preparing cost-effective and efficient GAC adsorbents for removing DOM in surface samples.

The study was assisted with a COMSOL Multiphysics simulation using version 5.6 (Free and porous media interface and the transport of diluted species in porous media interface). The simulation results established the fluid flow dynamics, in terms of the velocity profiles and pressure fields, and the transport of diluted species through the modelled adsorbent bed. The simulation results again successfully exhibited the fluid flow mechanics of proposed filter design as well as its future success and failures, whilst indicating the adsorbent's approximate lifetime under the predetermined conditions.

Moreover, although GAC adsorbents generally have a high potential in removing organic and chemical contaminants in water, its high production cost is a significant obstacle. Hence with the adoption of the methods used in this study with the modelled filtration system, the issue of safe drinking water scarcity could be solved in Africa, especially Ghana, using cost-effective chemicals and available agricultural by-products. But due to the vast applications of GAC, the prepared GAC adsorbents could be used in several other fields such as; manufacturing battery components, toothpaste, gas purification, precious mineral recovery, etcetera.

On the whole, the conventionally carbonized GAC adsorbents were observed to be more efficient in DOM removal, compared to the furnace carbonized GAC adsorbents, and hence the conventional technique has proven to be a better and cost-effective option than the furnace carbonization method.

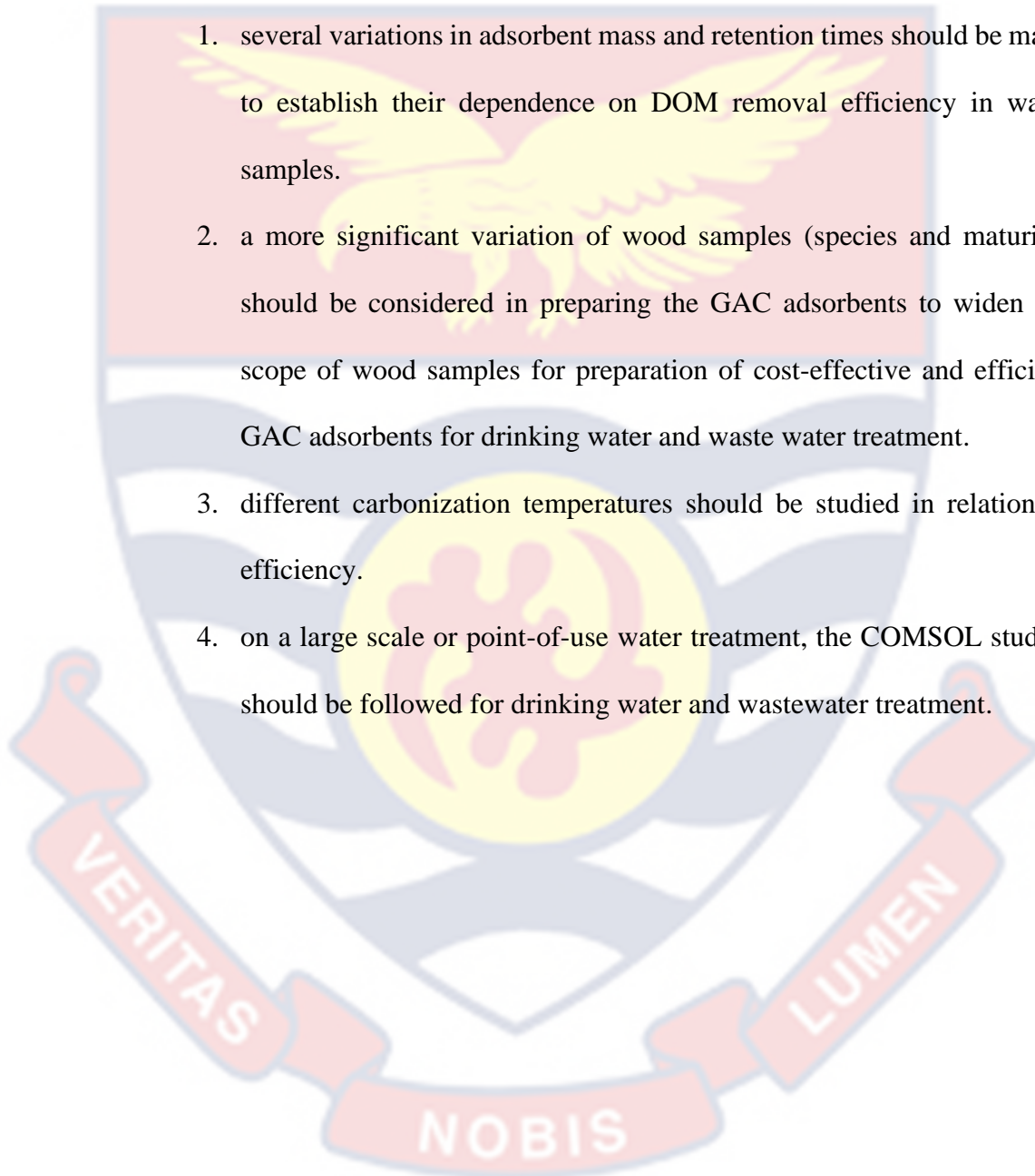
Hence, the study has provided novelty and has added knowledge to research and academia, through the development of a new method (APPENDIX A) for the preparation of effective GAC adsorbents in drinking water and waste water treatment. Moreover, the use of spectroscopy in assessing the DOM

removal efficiency of the prepared GAC adsorbents in a natural water sample is the first of its kind to the best of my knowledge.

### **Recommendations**

This study recommends the following:

1. several variations in adsorbent mass and retention times should be made to establish their dependence on DOM removal efficiency in water samples.
2. a more significant variation of wood samples (species and maturity) should be considered in preparing the GAC adsorbents to widen the scope of wood samples for preparation of cost-effective and efficient GAC adsorbents for drinking water and waste water treatment.
3. different carbonization temperatures should be studied in relation to efficiency.
4. on a large scale or point-of-use water treatment, the COMSOL studies should be followed for drinking water and wastewater treatment.





## REFERENCES

- Ahamed, K. R., Chandrasekaran, T., & Kumar, A. A. (2013). Characterization of Activated Carbon prepared from Albizia lebeck by Physical Activation. *International Journal of Interdisciplinary Research and Innovations (IJIRI)*, 1(1), 26–31.
- Ahmad, O. (2013). The effect of salt concentration on the pH of aqueous solution Question. Retrieved, October, 25, 2020, from, <https://www.researchgate.net/post/>
- Ali, R., Aslam, Z., Shawabkeh, R. A., Asghar, A., & Hussein, I. A. (2020). BET, FTIR, and RAMAN characterization of activated carbon from waste oil fly ash. *Turkish Journal of Chemistry*, 44(2), 279–295.
- Amuah, C. L. (2020). *Spectroscopic studies of some selected anti-malarial herbal plants sample combined with multivariate data analysis* (Doctoral thesis, University of Cape Coast). Retrieved, January, 30, 2021, from, <https://erl.ucc.gh/jspui>
- Arneli, Safitri, Z. F., Pangestika, A. W., Fauziah, F., Wahyuningrum, V. N., & Astuti, Y. (2017). The influence of activating agents on the performance of rice husk-based carbon for sodium lauryl sulfate and chrome (Cr) metal adsorptions. *IOP Conference Series: Materials Science and Engineering*, 172(2017), 1–8.
- Aziz, F., Ouazzani, N., Mandi, L., Assaad, A., Pontvianne, S., Poirot, H., & Pons, M. N. (2018). Characterization by fluorescence of dissolved organic matter in rural drinking water storage tanks in Morocco. *Journal of Water and Health*, 16(2), 321–328.
- Bagnell, R. (2012). Polarized light microscopy. *Pathology 464 Light Microscopy*. (2012). 1–6.

- Bakti, A. I., & Gareso, P. L. (2018). Characterization of active carbon prepared from coconuts shells using FTIR, XRD and SEM techniques. *Jurnal Ilmiah Pendidikan Fisika Al-Biruni*, 7(1), 33–39.
- Barker, J., Dubnick, A., Lyons, W., & Chin, Y. P. (2013). Changes in dissolved organic matter (DOM) fluorescence in proglacial antarctic streams. *Arctic, Antarctic, and Alpine Research*, 45(3), 305–317.
- Bazzi, A. (2020). *The Navier-Stokes equation*. Cantor's Paradise. Retrieved from <https://www.cantorsparadise.com>
- Bedru, D. D., Fufa, F., Navarro, I., Vachot, C., Kaushik, S., & Gutie, J. (2019). Removal of natural organic matter from water using chemically activated coffee husk. *American Journal of Chemical Research*, 3(14), 1–10.
- Bergna, D., Hu, T., Prokkola, H., Romar, H., & Lassi, U. (2020). Effect of some process parameters on the main properties of activated carbon produced from peat in a Lab-scale process. *Waste and Biomass Valorization*, 11(6), 2837–2848.
- Berthomieu, C., & Hienerwadel, R. (2009). Fourier transform infrared (FTIR) spectroscopy. *Photosynthesis Research*, 101(2–3), 157–170.
- Birkner, N., & Wang, Q. (2023). *How an FTIR Spectrometer Operates* (pp. 1–8). LibreTexts. Retrieved, November, 25, 2020, from, <https://chem.libretexts.org/>
- Bolton, L. (2003). *The application of excitation-emission fluorescence spectrophotometry to the monitoring of dissolved organic matter in upland catchments in the United Kingdom* (Doctoral thesis, University of Newcastle). Retrieved, November, 25, 2020, from, [papers2://publication/uuid/](https://papers2://publication/uuid/)
- Carstea, E. M., Popa, C. L., Baker, A., & Bridgeman, J. (2020). In situ

fluorescence measurements of dissolved organic matter: A review. *Science of the Total Environment*, 699, 1–45.

Cengel, Y. A., & Cimbala, J. M. (2006). *Fluid Mechanics: Fundamentals and Applications* (1st ed.). Nevada, USA: McGraw-Hill series in mechanical engineering. Retrieved from [www.mhhe.com/cengel](http://www.mhhe.com/cengel)

Chemistry LibreTexts. (2019). *The electromagnetic spectrum*. Retrieved from <https://chem.libretexts.org>

Chiu, T. P., Huang, W. S., Chen, T. C., & Yeh, Y. L. (2019). Fluorescence characteristics of dissolved organic matter (DOM) in percolation water and lateral seepage affected by soil solution (s-s) in a lysimeter test. *Sensors*, 19(4016), 1–13.

Cobb, A., Warms, M., Maurer, E. P., & Chiesa, S. (2012). Low-tech coconut shell activated charcoal production. *International Journal for Service Learning in Engineering, Humanitarian Engineering and Social Entrepreneurship*, 7(1), 93–104.

COMSOL Multiphysics®. (2017). Finite Element Mesh Refinement. <https://www.COMSOL.com>

COMSOL Multiphysics®. (2020). Porous Media Flow Module. <https://www.COMSOL.com>

Das, D., Samal, D. P., & Meikap. (2015). Preparation of activated carbon from green coconut shell and its characterization. *Journal of Chemical Engineering & Process Technology*, 06(05), 4–6.

Dewi, R., Agusnar, H., Alfian, Z., & Tamrin. (2018). Characterization of technical kaolin using XRF, SEM, XRD, FTIR and its potentials as industrial raw materials. *Journal of Physics: Conference Series*, 1116(4), 1–6.

- Dobek, S. (2012). *Fluid dynamics and the Navier-Stokes equation* (pp. 1–13). Retrieved from <http://scholar.google.com/>
- Dungani, R., Munawar, S. S., Karliati, T., Malik, J., Aditiawati, P., & Sulistyono. (2022). Study of characterization of activated carbon from coconut shells on various particle scales as filler agent in composite materials. *Journal of the Korean Wood Science and Technology*, 50(4), 256–271.
- Dutrow, B. L. (2022). *X-ray Powder Diffraction ( XRD )* (pp. 1–4). Louisiana: Louisiana State University.
- Edinburgh Instruments. (2022). *What is laser induced fluorescence?* (pp. 1–11). Retrieved from <https://www.edinst.com/us/blog/what-is-laser-induced-fluorescence/>
- Farma, R., Wahyuni, F., & Awitdrus. (2019). Physical properties analysis of activated carbon from oil palm empty fruit bunch fibre on methylene blue adsorption. *Journal of Technomaterial Physics*, 1(1), 69–75.
- Ferris, D. G., Li, W., Gustafsson, U., Lieberman, R. W., Galdos, O., & Santos, C. (2010). Enhancing colposcopy with polarized light. *Journal of Lower Genital Tract Disease*, 14(3), 149–154.
- Galvão, R. B., da Silva Moretti, A. A., Fernandes, F., & Kuroda, E. K. (2021). Post-treatment of stabilized landfill leachate by upflow gravel filtration and granular activated carbon adsorption. *Environmental Technology (United Kingdom)*, 42(26), 4179–4188.
- García, I. (2011). *Removal of Natural Organic Matter to reduce the presence of Trihalomethanes in drinking water*. Royal Institute of Technology.
- Gonite, T. (2015). *Simulation of water transport through nano-foam filter*. Addis Ababa University.



- Griesmer, A. (2013). *What Is COMSOL Multiphysics?* (pp. 1–2). Retrieved from <https://www.COMSOL.com/blogs/>
- Griesmer, A. (2014). Size Parameters for Free Tetrahedral Meshing in COMSOL Multiphysics. *COMSOL Blog*.
- Gryczynski, Z., & Gryczynski, I. (2020). *Practical fluorescence spectroscopy*. <https://doi.org/10.1201/9781315374758>
- Halliday, A. (2017). Creating a New Material in COMSOL Multiphysics. *COMSOL Blog*.
- Hansen, A. M., Kraus, T. E. C., Pellerin, B. A., Fleck, J. A., Downing, B. D., & Bergamaschi, B. A. (2016). Optical properties of dissolved organic matter (DOM): Effects of biological and photolytic degradation. *Limnology and Oceanography*, *61*(3), 1015–1032.
- Hardesty, J., & Attili, B. (2010). *Spectrophotometry and the Beer-Lambert Law: An Important Analytical Technique in Chemistry* (pp. 1–6).
- Health Canada. (2019). *Guidance on natural organic matter in drinking water*. Ottawa, Ontario, Canada.
- Heibati, M., Stedmon, C. A., Stenroth, K., Rauch, S., Toljander, J., Säve-Söderbergh, M., & Murphy, K. R. (2017). Assessment of drinking water quality at the tap using fluorescence spectroscopy. *Water Research*, *125*, 1–10.
- Hidayah, E. N., Chou, Y. C., & Yeh, H. H. (2018). Characterization and removal of natural organic matter from slow sand filter effluent followed by alum coagulation. *Applied Water Science*, *8*(3), 1–7.
- Hoslett, J., Massara, T. M., Malamis, S., Ahmad, D., van den Boogaert, I., Katsou, E., ... Jouhara, H. (2018). Surface water filtration using granular media and membranes: A review. *Science of the Total Environment*, *128*



639(2018), 1268–1282.

Hudson, N., Baker, A., & Reynolds, D. (2007). Fluorescence Analysis of Dissolved Organic Matter in Natural, Waste and Polluted Waters—A Review. *River Research and Applications*, 30(2), 307–328.

Hussain, A. F. (2019). *UV-Visible spectrometry* (pp. 1–16). ResearchGate.

Jjagwe, J., Olupot, P. W., Menya, E., & Kalibbala, H. M. (2021). Synthesis and application of granular activated carbon from biomass waste materials for water treatment: A Review. *Journal of Bioresources and Bioproducts*, 6(4), 292–322.

Joshi, S. (2018). Comparative Study on the Adsorption Capacity of Activated Carbon Prepared from Lapsi Seed Stone and Betel nut using Phosphoric Acid. *Journal of the Institute of Engineering*, 13(1), 153–159.

Khan, I., Memon, A. A., Memon, M. A., Bhatti, K., Shaikh, G. M., Baleanu, D., & Alhussain, Z. A. (2020). Finite Element Least Square technique for Newtonian fluid flow through a semicircular cylinder of recirculating region via COMSOL Multiphysics. *Journal of Mathematics*, 2020, 1–11.

Khan, S., Yaoguo, W., Xiaoyan, Z., Jingtao, L., Jichao, S., & Sihai, H. (2014). Relationship for the Concentration of Dissolved Organic Matter from Corn Straw with Absorbance by using UV-Visible Spectrophotometer. *International Journal of Environmental Pollution and Remediation*, 2(1), 10–15.

Kim, C., Ji, T., & Eom, J. B. (2018). Determination of organic compounds in water using ultraviolet LED. *Measurement Science and Technology*, 29(4), 1–7.

Kim, J., Morgott, A., Wu, Z., Hopaluk, L., Miles, M., Stoner, W., & Li, Q. (2019). Simulating transport and adsorption of organic contaminants in 3D

- porous activated carbon block media. *COMSOL Conference*, 1–7. Boston.
- Korak, J. A., Rosario-Ortiz, F. L., & Scott Summers, R. (2015). Evaluation of optical surrogates for the characterization of DOM removal by coagulation. *Environmental Science: Water Research and Technology*, *1*(4), 493–506.
- Kudela, H. (2022). *Viscous flow in pipe* (pp. 1–6). Retrieved from <http://www.itcmp.pwr.wroc.pl/>
- Kwasi Opoku, B., Ogbonna Friday, J., David Kofi, E., & Benson Osa, E. (2020). Adsorption of heavy metals contaminants in used lubricating oil using palm kernel and coconut shells activated carbons. *American Journal of Chemical Engineering*, *8*(1), 11–18.
- Lakowicz, J. R. (2006). Principles of fluorescence spectroscopy. In *Principles of Fluorescence Spectroscopy*. <https://doi.org/10.1007/978-0-387-46312-4>
- Lee, S. M., Lee, S. H., & Roh, J. S. (2021). Analysis of activation process of carbon black based on structural parameters obtained by XRD analysis. *Crystals*, *11*(2), 1–11.
- Liao, Y. (2013). *Practical Electron Microscopy and Database*. GlobalSino. Retrieved from <https://www.techuk.org/insights/opinions/item>
- Lu, Z., Sun, W., Li, C., Cao, W., Jing, Z., Li, S., ... Liu, S. (2020). Effect of granular activated carbon pore-size distribution on biological activated carbon filter performance. *Water Research*, *177*(2020), 1–11.
- Mensah, E. E., Abbas, Z., Azis, R. S., Khamis, N. A. I., & Mamoun, A. (2019). Complex Permittivity and Microwave Absorption Properties of OPEFB Fiber–Polycaprolactone Composites Filled with Recycled Hematite ( $\alpha$ -Fe<sub>2</sub>O<sub>3</sub>) Nanoparticles. *Polymers*, *11*(918), 1–11.
- Mohammad Razi, M. A., Al-Gheethi, A., Al-Qaini, M., & Yousef, A. (2018).

- Efficiency of activated carbon from palm kernel shell for treatment of greywater. *Arab Journal of Basic and Applied Sciences*, 25(3), 103–110.
- Moona, N. (2021). *Assessing and optimizing biofilter performance in drinking water treatment*. Chalmers University of Technology.
- Mopoung, S., Moonsri, P., Palas, W., & Khumpai, S. (2015). Characterization and properties of activated carbon prepared from tamarind seeds by KOH activation for Fe ( III ) adsorption from aqueous solution. *The Scientific World Journal*, 2015, 1–7.
- Multiphysics. (2022). *Physics, PDEs, and Numerical Modeling* (pp. 1–3). COMSOL Multiphysics.
- Munir, A., & Spirka, T. (2013). An Introduction to COMSOL Multiphysics v4.3b & Subsurface Flow Simulation. COMSOL Conference, Boston, COMSOL Multiphysics
- Muniz, F. T. L., Santos, M., Miranda, M. A. R., & Universidade, J. M. S. (2016). The Scherrer equation and the dynamical theory of X-ray diffraction. *Acta Cryst*, A72(August), 1–6.
- Murphy, K. R., Graeber, D., Stedmon, C. A., & Bro, R. (2013). Fluorescence spectroscopy and multi-way techniques. PARAFAC. *Royal Society of Chemistry*, 5(23), 1–10.
- Ndi Nsami, J., & Ketcha Mbadcam, J. (2013). The adsorption efficiency of chemically prepared activated carbon from cola nut shells by ZnCl<sub>2</sub> on methylene blue. *Journal of Chemistry*, 2013, 1–7.
- Nwosu, F. O., Ajala, O. J., Owoyemi, R. M., & Raheem, B. G. (2018). Preparation and characterization of adsorbents derived from bentonite and kaolin clays. *Applied Water Science*, 8(7), 1–10.
- Okache, J., Haggett, B., & Ajmal, T. (2015). UV LED fluorescence-based

method for detecting organic contaminants in water: A Review. *Transactions on Machine Design*, 3(1), 1–10.

Osman, A. I., Blewitt, J., Adu-Dahrieh, J. K., Farrell, C., Al-Muhtaseb, A. H., Harrison, J., & Rooney, D. W. (2019). Production and characterisation of activated carbon and carbon nanotubes from potato peel waste and their application in heavy metal removal. *Environmental Science Pollution Research*, 26(2019), 37228–37241.

Pavia, D. L., Lampman, G. M., & Kriz, G. S. (2001). *Introduction to spectroscopy* (3rd ed.; J. Vondeling, Ed.). Thomson Learning, Inc.

Pavia, D. L., Lampman, G. M., Kriz, G. S., & Vyvyan, J. R. (2004). *Introduction to spectroscopy* (5th ed.). Stamford: Cengage Learning. <https://doi.org/10.1887/0750303468/b293c1>

PhysiologyWeb. (2017). *Molar solution concentration calculator* (pp. 1–2). PhysiologyWeb. Retrieved from [www.physiologyweb.com](http://www.physiologyweb.com)

Raja, S. H. (2020). *Clustering analysis & PCA visualisation - A Guide on unsupervised learning* (pp. 1–14). Codepth.

Rančić, D. (2019). Polarized light microscopy. In *Application of Molecular Methods and Raman Microscopy/ Spectroscopy in Agricultural Sciences and Food Technology* (pp. 193–198). <https://doi.org/10.4103/0378-6323.32754>

Rodgers, T. (2013). *Fluid Flow*. Retrieved from <https://vdocuments.mx/>

Sefa-Ntiri, B., Mensah-Amoah, P., Okoto, R. J. S., & Tatchie, E. T. (2014). Measurement of optical turbidity of drinking water samples, using nephelometric and laser light techniques. *American International Journal of Contemporary Scientific Research*, 1(4), 22–33.

Sefa-Ntiri, B., Awuah, B. K., Edziah, R., Anderson, B., Armah, F. A., Mensah,



- P. A., ... Kumi, F. (2020). Dissolved organic matter in hand - dug well water as groundwater quality indicator : assessment using laser - induced fluorescence spectroscopy and multivariate statistical techniques. *SN Applied Sciences*, 2(834), 1–15.
- Shabiimam M., A., Tehsin, K., Anas, P., & Shifa, S. (2018). Treatment of water using various filtration techniques: Review study. *Construction Management Practices*, 1(November 2018), 229–235.
- Sharma, S., & Bhattacharya, A. (2017). Drinking water contamination and treatment techniques. *Applied Water Science*, 7(3), 1043–1067.
- Shepel, D., Goreacioc, T., Lupascu, T., Filippov, M., & Rusu, M. (2015). Method of Infrared spectra registration of activated carbons in Potassium Bromide pellets. *Chemistry Journal of Moldova.*, 10(1), 113–115.
- Shukla, S. K., Al Mushaiqri, N. R. S., Al Subhi, H. M., Yoo, K., & Al Sadeq, H. (2020). Low-cost activated carbon production from organic waste and its utilization for wastewater treatment. *Applied Water Science*, 10(2), 1–9.
- Speakman, S. (2022). Estimating Crystallite Size Using XRD (MIT Center for Materials Science and Engineering. *MIT Center for Materials Science and Engineering*, 1–15.
- Sweetman, M. J., Sebben, D., Noll, B. D., Wang, W. H., May, S., Mebberson, N., ... Hayball, J. D. (2018). *A rapid technique to determine performance and efficiency of activated carbon water filters*. 371–382.
- Tahir, D., Liong, S., & Bakri, F. (2016). Molecular and structural properties of polymer composites filled with activated charcoal particles. *AIP Conference Proceedings*, 1719(March), 1–4.
- United States Environmental Protection Agency. (2012). 2012 Edition of the



drinking water standards and health advisories. In *Spring 2012*. Washington, DC, USA.

Vajdi, M., Moghanlou, F. S., Sharifanajazi, F., Asi, M. S., & Shokouhimehr, M.

(2020). A review on the COMSOL Multiphysics studies of heat transfer in advanced ceramics. *Journal of Composites and Compounds*, 2(2020), 35–43.

Wang, M., & Chen, Y. (2018). Generation and characterization of DOM in wastewater treatment processes. *Chemosphere*, 201(2018), 96–109.

Wang, W., Zheng, B., Jiang, X., Chen, J., & Wang, S. (2020). Characteristics and source of dissolved organic matter in Lake Hulun, A large Shallow Eutrophic Steppe Lake in Northern China. *Water (Switzerland)*, 12(4).

Wasswa, J. (2018). *Application of Fluorescence Spectroscopy to Track Membrane Fouling , Failure , and Contaminants in Water and Wastewater Systems*. San Diego State University.

Watson, K., Farré, M. J., Leusch, F. D. L., & Knight, N. (2018). Using fluorescence-parallel factor analysis for assessing disinfection by-product formation and natural organic matter removal efficiency in secondary treated synthetic drinking waters. *Science of the Total Environment*, 640–641(2018), 31–40.

Williams, C. J., Conrad, D., Kothawala, D. N., & Baulch, H. M. (2019). Selective removal of dissolved organic matter affects the production and speciation of disinfection byproducts. *Science of the Total Environment*, 652(2019), 75–84.

World Health Organisation, (2017). Guidelines for drinking-water quality. In *Incorporating the first addendum* (Vol. 55). [https://doi.org/10.5005/jp/books/11431\\_8](https://doi.org/10.5005/jp/books/11431_8)

World Health Organisation, (2019). Drinking-water. *World Health Organization*, (pp. 1–7). World Health Organization. Retrieved from <https://www.who.int/news-room/fact-sheets/detail/drinking-water>

World Health Organisation, (2020). Monitoring health for the SDGs. In *World Health Statistics* (Vol. 21).

Xing, X., Li, T., Bi, Z., Qi, P., Li, Z., Wang, H., ... Hu, C. (2020). Efficient removal of disinfection by-products precursors and inhibition of bacterial detachment by strong interaction of EPS with coconut shell activated carbon in ozone/biofiltration. *Journal of Hazardous Materials*, 392(February), 12–27.

Yamada, T., Rosadi, M. Y., Hudori, Suzuki, Y., Ito, E., & Li, F. (2019). Characteristics of dissolved organic matter in a water purification plant and distribution pipes. *MATEC Web of Conferences*, 280, 03007.

Yan, W., Liu, M., & Jing, F. (2018). Shape inverse problem for Stokes-Brinkmann equations. *Applied Mathematics Letters*. <https://doi.org/10.1016/j.aml.2018.09.003>

Yang, L., Chen, W., Zhuang, W. E., Cheng, Q., Li, W., Wang, H., ... Liu, M. (2019). Characterization and bioavailability of rainwater dissolved organic matter at the southeast coast of China using absorption spectroscopy and fluorescence EEM-PARAFAC. *Estuarine, Coastal and Shelf Science*, 217(November 2018), 45–55.

Yunus, S. (2020). *Fabrication of a prototype membrane filter for drinking water purification assisted by COMSOL Multiphysics simulations*. University of Cape Coast.

Yunus, S., Sefa-ntiri, B., Anderson, B., Kumi, F., Mensah-amoaah, P., & Sackey, S. S. (2019). Quantitative pore characterization of polyurethane foam with

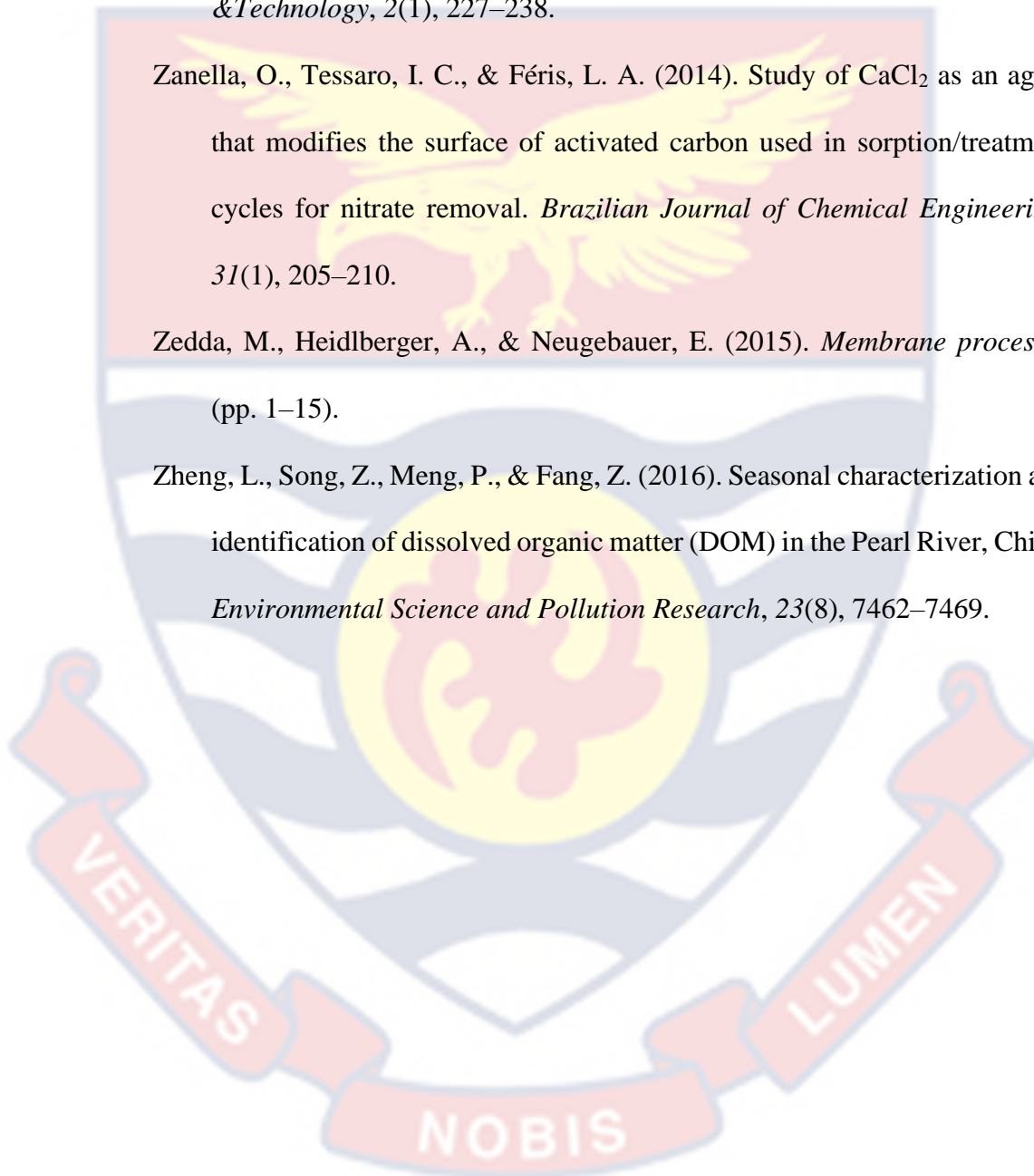
cost-effective imaging tools and image analysis: A proof-of-principle study. *Polymers*, 11(1879), 1–16.

Yusuf, S., & Audu, A. A. (2017). Characterization of Dissolved Organic Matter in selected wetlands from northern Nigeria. *Trends in Science & Technology*, 2(1), 227–238.

Zanella, O., Tessaro, I. C., & Féris, L. A. (2014). Study of  $\text{CaCl}_2$  as an agent that modifies the surface of activated carbon used in sorption/treatment cycles for nitrate removal. *Brazilian Journal of Chemical Engineering*, 31(1), 205–210.

Zedda, M., Heidelberger, A., & Neugebauer, E. (2015). *Membrane processes* (pp. 1–15).

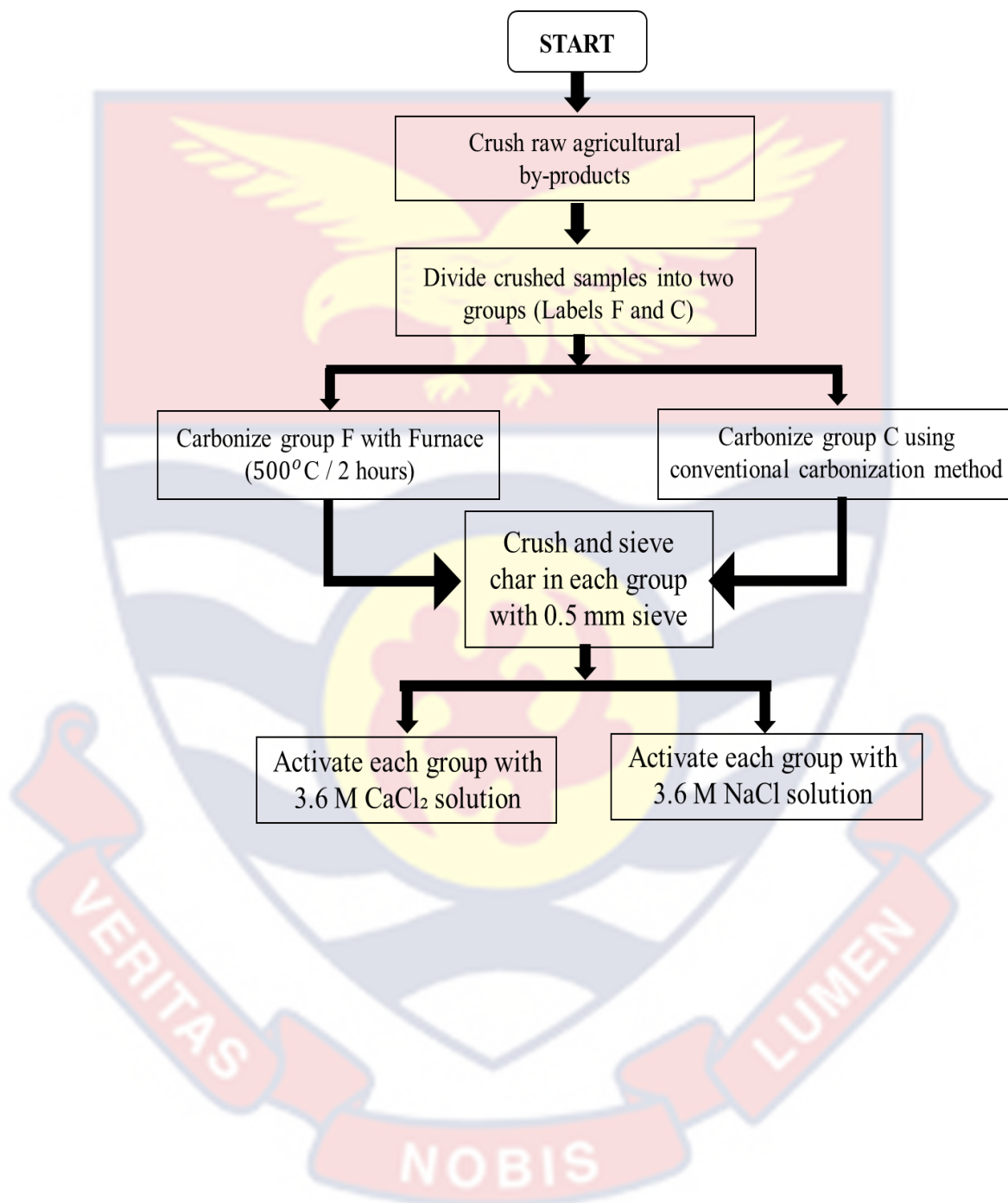
Zheng, L., Song, Z., Meng, P., & Fang, Z. (2016). Seasonal characterization and identification of dissolved organic matter (DOM) in the Pearl River, China. *Environmental Science and Pollution Research*, 23(8), 7462–7469.



## APPENDICES

## APPENDIX A

## GAC ADSORBENT PREPARATION PROTOCOL





## APPENDIX B

## PHYSICOCHEMICAL PARAMETERS

Sample ID	pH	Salinity (PPT)	C_CS_NA(F2)	7.05	0.15	C_CT_NA(F3)	6.88	0.76
			C_CS_NA(F3)	6.99	0.11	F_ST_CA(B1)	7.25	0.32
Bm_FP	7.00	0.08	F_CT_CA(B1)	7.56	0.05	F_ST_CA(B2)	7.24	0.38
F_CS_CA(B1)	7.69	0.07	F_CT_CA(B2)	7.35	0.09	F_ST_CA(B3)	7.32	0.36
F_CS_CA(B2)	7.24	0.07	F_CT_CA(B3)	7.55	0.04	F_ST_CA(D1)	7.77	0.60
F_CS_CA(B3)	7.61	0.13	F_CT_CA(D1)	7.64	0.07	F_ST_CA(D2)	7.18	0.69
F_CS_CA(D1)	7.64	0.20	F_CT_CA(D2)	7.84	0.09	F_ST_CA(D3)	7.36	0.81
F_CS_CA(D2)	7.48	0.09	F_CT_CA(D3)	7.85	0.07	F_ST_CA(F1)	7.93	0.80
F_CS_CA(D3)	7.97	0.12	F_CT_CA(F1)	7.73	0.06	F_ST_CA(F2)	7.13	0.88
F_CS_CA(F1)	7.43	0.16	F_CT_CA(F2)	7.87	0.09	F_ST_CA(F3)	7.26	1.33
F_CS_CA(F2)	7.63	0.14	F_CT_CA(F3)	7.82	0.19	F_ST_NA(B1)	7.42	0.14
F_CS_CA(F3)	7.83	0.15	F_CT_NA(B1)	7.55	0.13	F_ST_NA(B2)	7.43	0.14
F_CS_NA(B1)	7.20	0.27	F_CT_NA(B2)	7.48	0.11	F_ST_NA(B3)	8.07	0.16
F_CS_NA(B2)	7.35	0.15	F_CT_NA(B3)	7.45	0.09	F_ST_NA(D1)	7.89	0.27
F_CS_NA(B3)	7.21	0.20	F_CT_NA(D1)	7.26	0.18	F_ST_NA(D2)	7.48	0.26
F_CS_NA(D1)	7.29	0.33	F_CT_NA(D2)	7.21	0.23	F_ST_NA(D3)	7.58	0.26
F_CS_NA(D2)	8.04	0.42	F_CT_NA(D3)	7.14	0.16	F_ST_NA(F1)	8.84	0.34
F_CS_NA(D3)	7.47	0.15	F_CT_NA(F1)	7.46	0.24	F_ST_NA(F2)	7.56	0.36
F_CS_NA(F1)	7.29	0.38	F_CT_NA(F2)	6.91	0.15	F_ST_NA(F3)	8.50	0.36
F_CS_NA(F2)	7.48	0.23	F_CT_NA(F3)	7.16	0.24	C_ST_CA(B1)	7.55	0.33
F_CS_NA(F3)	7.02	0.15	C_CT_CA(B1)	7.44	0.67	C_ST_CA(B2)	7.54	0.39
C_CS_CA(B1)	7.04	0.10	C_CT_CA(B2)	7.38	0.84	C_ST_CA(B3)	7.52	0.42
C_CS_CA(B2)	7.00	0.11	C_CT_CA(B3)	7.71	0.86	C_ST_CA(D1)	7.78	0.58
C_CS_CA(B2)	7.59	0.11	C_CT_CA(D1)	7.14	1.67	C_ST_CA(D2)	7.28	0.59
C_CS_CA(D1)	7.25	0.17	C_CT_CA(D2)	7.40	1.70	C_ST_CA(D3)	7.46	0.80
C_CS_CA(D2)	7.05	0.18	C_CT_CA(D3)	7.64	1.66	C_ST_CA(F1)	7.69	0.82
C_CS_CA(D3)	7.56	0.11	C_CT_CA(F1)	7.45	2.21	C_ST_CA(F2)	7.51	0.90
C_CS_CA(F1)	7.08	0.28	C_CT_CA(F2)	7.51	2.32	C_ST_CA(F3)	7.46	1.36
C_CS_CA(F2)	6.95	0.26	C_CT_CA(F3)	7.17	0.64	C_ST_NA(B1)	7.52	0.17
C_CS_CA(F3)	7.15	0.20	C_CT_NA(B1)	7.97	0.29	C_ST_NA(B2)	7.54	0.15
C_CS_NA(B1)	6.88	0.07	C_CT_NA(B2)	8.05	0.81	C_ST_NA(B3)	8.29	0.10
C_CS_NA(B2)	6.85	0.06	C_CT_NA(B3)	7.93	0.41	C_ST_NA(D1)	7.99	0.32
C_CS_NA(B3)	6.88	0.07	C_CT_NA(D1)	8.26	0.76	C_ST_NA(D2)	7.58	0.31
C_CS_NA(D1)	6.71	0.11	C_CT_NA(D2)	8.21	0.82	C_ST_NA(D3)	7.58	0.30
C_CS_NA(D2)	6.75	1.01	C_CT_NA(D3)	8.35	0.68	C_ST_NA(F1)	8.43	0.35
C_CS_NA(D3)	6.91	0.12	C_CT_NA(F1)	8.42	1.62	C_ST_NA(F2)	7.67	0.38
C_CS_NA(F1)	6.91	0.15	C_CT_NA(F2)	8.50	1.28	C_ST_NA(F3)	8.20	0.40



APPENDIX C

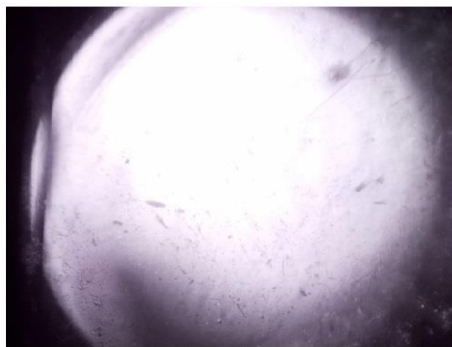
POLARIZED LIGHT IMAGES



F\_CS\_CA



F\_CS\_NA



C\_CS\_CA



C\_CS\_NA



F\_CT\_CA



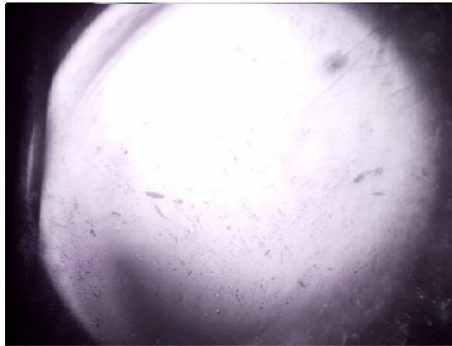
F\_CT\_NA



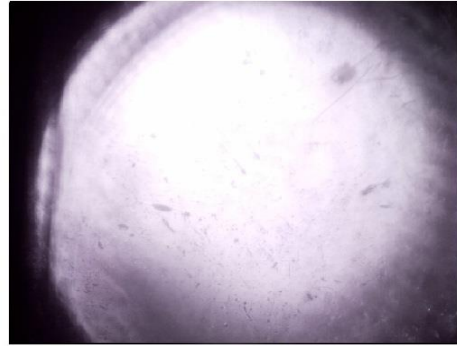
C\_CT\_CA



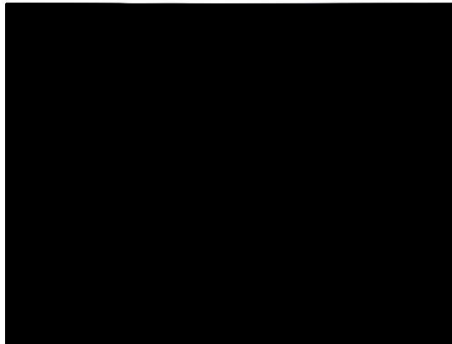
C\_CT\_NA



F\_ST\_CA



F\_ST\_NA



C\_ST\_CA

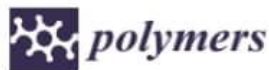


C\_ST\_NA



## PUBLICATIONS

Yunus, S., Sefa-Ntiri, B., Anderson, B., Kumi, F., Mensah-Amoah, P., & Sackey, S. S. (2019). Quantitative Pore Characterization of Polyurethane Foam with Cost-Effective Imaging Tools and Image Analysis : A Proof-Of-Principle Study. *Polymers*, 11(1879), 1–16.



Article

## Quantitative Pore Characterization of Polyurethane Foam with Cost-Effective Imaging Tools and Image Analysis: A Proof-Of-Principle Study

Shemmira Yunus <sup>1</sup>, Baah Sefa-Ntiri <sup>1,\*</sup>, Benjamin Anderson <sup>1</sup>, Francis Kumi <sup>2</sup>, Patrick Mensah-Amoah <sup>1</sup> and Samuel Sonko Sackey <sup>1</sup>

<sup>1</sup> Department of Physics, University of Cape Coast, PMB, Ghana

<sup>2</sup> Department of Agricultural Engineering, University of Cape Coast, PMB, Ghana

\* Correspondence: bsefa-ntiri@ucc.edu.gh; Tel.: +233-201863483

Received: 18 September 2019; Accepted: 30 October 2019; Published: 14 November 2019



**Abstract:** This study investigated the pore characterization of polyurethane (PU) foam as a necessary step in water filtration membrane fabrication. Porous material characterization is essential for predicting membrane performance, strength, durability, surface feel, and to understand the transport mechanisms using modeling and simulations. Most existing pore characterization techniques are relatively costly, time-consuming, subjective, and have cumbersome sample preparations. This study focused on using three relatively inexpensive imaging systems: a black box, Canon camera (EOS760D), and LaserJet scanner (M1132 MFP). Two standard, state-of-the-art imaging systems were used for comparison: a stereomicroscope and a scanning electron microscope. Digital images produced by the imaging systems were used with a MATLAB algorithm to determine the surface porosity, pore area, and shape factor of the polyurethane foam in an efficient manner. The results obtained established the compatibility of the image analysis algorithm with the imaging systems. The black box results were found to be more comparable to both the stereomicroscope and SEM systems than those of the Canon camera and scanner imaging systems. Indeed, the current research effort demonstrates the possibility of substrate characterization with inexpensive imaging systems.

**Keywords:** porous substrate; polyurethane foam; image analysis; pore morphology; inexpensive imaging systems

### 1. Introduction

Globally, the production of polyurethane (PU) foams dominates all other polymeric foams [1] as they are commercially inexpensive. Mostly, polymeric foams are the first choice for a wide range of technological applications, and PU foam consumption is 50% of the global polyurethane consumption [2]. The processing technology required to produce them is well-established when compared with foams derived from other polymers [2]. PU foams are lightweight, excellent porous materials with tunable thermal stability plus mechanical and sound-absorption properties for a range of applications, suitable for new and advanced technologies [1]. PU foams are generally made up of polyols and isocyanates. They can be recycled or recovered after use to reduce production costs and increase material utilization efficiency [3]. Thermosetting polymers like PU foams are widely preferred due to their light weight, excellent biocompatibility, flexible mechanical properties, and the presence of a urethane linkage (–NH–CO–O–) that bonds easily with nanoparticles such as silver nanoparticles (AgNPs) [4–10]. Also, PU foams have the capability of delivering a wide range of cell structures, rigidity, strength, and durability. The cell structure, whether it is open or closed, is another variable that must be considered. However, most flexible foams are designed to be of an



Sefa-Ntiri, B., Awuah, B. K., Anderson, R. Edziah. B., Mensah, F. A. Armah. P., Sackey, A. S. S., Sam, F., Akyea, A. G., **Yunus, S.**, Tatchie, E., Nkansah, B. K., & Kumi, F. (2020). Dissolved organic matter in hand-dug well water as groundwater quality indicator : assessment using laser-induced fluorescence spectroscopy and multivariate statistical techniques. *SN Applied Sciences*, 2(834), 1–15. <https://doi.org/10.1007/s42452-020-2446-4>

Research Article



## Dissolved organic matter in hand-dug well water as groundwater quality indicator: assessment using laser-induced fluorescence spectroscopy and multivariate statistical techniques

B. Sefa-Ntiri<sup>1</sup> · B. Kwakye-Awuah<sup>3</sup> · R. Edziah<sup>1</sup> · B. Anderson<sup>1</sup> · F. A. Armah<sup>2</sup> · P. Mensah-Amoah<sup>1</sup> · S. S. Sackey<sup>1</sup> · F. Sam<sup>1</sup> · A. G. Akyea<sup>1</sup> · S. Yunus<sup>1</sup> · E. Tatchie<sup>1</sup> · B. K. Nkansah<sup>4</sup> · F. Kumi<sup>5</sup>

Received: 14 November 2019 / Accepted: 6 March 2020  
© Springer Nature Switzerland AG 2020

### Abstract

In groundwater, dissolved organic matter (DOM), a complex material, is a contaminant of concern owing to its ability to influence water quality and stimulate microbial metabolism. Using a 445-nm diode laser-induced fluorescence (LIF) spectroscopy, DOM contamination levels have been investigated of well water samples fetched from ten privately owned hand-dug wells during dry and wet seasons of 2016, 2017 and 2018, in Ghana. The results showed spatio-temporal heterogeneities in the LIF spectra, and the fluorescence intensity peaks were generally higher and broader during the wet season than the dry season. In this study, DOM fluorescence spectra at an emission wavelength band of 460–650 nm showed two distinct broad peak shoulders within 480–500 nm and 550–570 nm, engulfing the water Raman peak at 527 ± 2 nm for all the water samples studied. Furthermore, principal component analysis and cluster analysis were used to differentiate the 2016 water samples based on their DOM contamination levels. In each case, three groups or clusters were identified based on their similarities and dissimilarities. The study revealed humic DOM substances as the most typical well water fluorophores. Applying the K-nearest neighbour algorithm as a classifier method for the classification of 30 water samples studied in 2016, 16.7% (5/30) were classified as very good drinking water, 46.7% (14/30) as good, 26.7% (8/30) as fairly good, and 10% (3/30) as bad drinking water samples. In general, levels of dissolved organic matter contamination increased over the study period during the rainy seasons for wells situated in close proximity to septic tanks, refuse dumps, public toilets and in wetlands. Thus, in the study the fluorescence intensity depends on the sampling site and the season, and indicates the DOM contamination level.

**Keywords** Dissolved organic matter · Hand-dug well water · Laser-induced fluorescence · Dry and wet seasons · Multivariate statistical techniques · Water quality monitoring and assessment

### 1 Introduction

Most of the available freshwater on Earth is locked up in the ground [47]. For this reason, groundwater constitutes the main resource in terms of obtainable quantities

for water supply. Globally, in excess of two billion people depend on groundwater for their day-to-day water use [41, 47]. In both the global north and south, groundwater bodies are the most vital and safest source of drinking water [3, 32, 47]. Groundwater sources are very important

✉ B. Sefa-Ntiri, [bsefa-ntiri@ucc.edu.gh](mailto:bsefa-ntiri@ucc.edu.gh) | <sup>1</sup>Department of Physics, School of Physical Sciences, College of Agriculture and Natural Sciences, University of Cape Coast, Cape Coast, Ghana. <sup>2</sup>Department of Environmental Science, School of Biological Sciences, College of Agriculture and Natural Sciences, University of Cape Coast, Cape Coast, Ghana. <sup>3</sup>Department of Physics, Kwame Nkrumah University of Science and Technology, Kumasi, Ghana. <sup>4</sup>Department of Statistics, School of Physical Sciences, College of Agriculture and Natural Sciences, University of Cape Coast, Cape Coast, Ghana. <sup>5</sup>Department of Agricultural Engineering, School of Agriculture, College of Agriculture and Natural Sciences, University of Cape Coast, Cape Coast, Ghana.



SN Applied Sciences (2020) 2:834 | <https://doi.org/10.1007/s42452-020-2446-4>

Published online: 07 April 2020

SN Applied Sciences  
A SPRINGER NATURE journal